STRUCTURAL CHARACTERISATION OF BIOACTIVE GLASSES

A THESIS SUBMITTED TO
THE UNIVERSITY OF KENT
IN THE SUBJECT OF PHYSICS
FOR THE DEGREE OF
DOCTOR OF PHILOSOPHY

Victoria FitzGerald
July 2007

All you deem important

is nothing compared

to the equation

$E=mc^2$

Poem by Mr. James Edward FitzGerald, 2002.

Acknowledgements

I would firstly, and most importantly, like to thank my supervisor Professor Bob Newport. He is the reason I started my journey in research, the reason I carried on, and the reason I managed to finish. Without his constant support, insight and enthusiasm I would have undoubtedly given up at the first hurdle. I would also like to thank all other members of the research group, past and present particularly Dr Dave Pickup, Dr Daniella Carta, Dr Laura Skipper, Dr Frank Sowrey, Dr Gavin Mountjoy, Dr Dong Qiu and also Rob Moss and Kate Wetherall, for constant support and entertainment at Daresbury, and for providing me with answers to my endless questions. Thanks must also go to the members of the sol-gel group, namely Professor Mark Smith, Dr Julian Jones, Professor Jonathan Knowles and Dr Kieran Drake, again for support, and much needed help and advice on Daresbury/ESRF experiments. It has been pure joy to work with such wonderfully talented people.

I would also like to thank Dr Dave Greenspan, formerly of NovaMin Technology Ltd, for giving me the opportunity to work at the University of Florida, and for all the help and advice provided when writing papers.

Many thanks go to all the station scientists at Daresbury Laboratory and ISIS, particularly Dr Alex Hannon, Dr Mark Roberts, and Dr Chris Martin for making every experiment go as smoothly as it possibly could.

Thanks must also go to all the gorgeous sexy people in the Science@kent crew, they made the last three years a joy even when I thought things were going horribly wrong. Thanks to Becky Parker, a true inspiration, Steve Walls, Mark Johnson, George Dobre, Nick Foster, Sam Lister and Sharon Humm, for allowing me to spread my love of physics in schools across the country, and thanks to Steve and Mark

especially for providing me with bottles of Malibu when I needed them. Thank you also for introducing me to the many ways to play with liquid nitrogen and dry ice and thanks Mark for letting me shoot you (several times).

Lastly I'd like to thank the people closest to me, without whom, I would never have accomplished anything. My mum Carole and dad Jim have supported me endlessly whatever I chose to do, and have always believed in me, giving me the ability to carry on until the end. My two sisters, Elizabeth and Alexandra make my world a lovely place to be, I am so proud of them, and I would like to specifically thank them for just being there, which means more than they will ever know.

I would like to finish with a story: Whilst watching TV, a presenter was talking about words they associated with the word silver. 'Moon' they said first. Matt then said to me 'What would you associate with the word silver?' And I replied 'Erm, antibacterial properties'.

Matt, thanks for not running away x

Abstract

Melt-quenched glasses containing SiO_2, CaO, Na_2O and P_2O_5, and sol-gel derived glasses containing SiO_2 and CaO are known to have bioactive properties. Foaming of binary sol-gel derived bioactive glasses containing SiO_2 and CaO can be used to produce 3D porous scaffolds which mimic the structure of trabecular bone, increasing the potential for these glasses to be used as bioactive bone-regenerative materials.

A range of experimental techniques have been used to investigate the atomic scale structure of these materials, and also to observe the reaction mechanisms which occur when these materials are immersed in a simulated physiological solution (simulated body fluid, SBF) and a standard cell culture medium (tris buffer solution, TBS).

A robust structural model of the most bioactive of the melt-quenched glasses, namely Bioglass®, has been produced by combining high energy X-ray and neutron diffraction data, magic angle spinning nuclear magnetic resonance (MAS NMR) and reverse Monte Carlo (RMC) modelling. It has been shown that Ca clustering occurs in the glass, which is of direct relevance to the understanding of the facile nature of calcium within such glasses giving rise to its relatively rapid diffusion from the solid into solution.

Hydroxyapatite has been confirmed as the calcium phosphate phase which grows on the surface of Bioglass® when immersed in the standard cell culture medium, TBS.

A new method which can be used for *in-situ* time resolved high-energy X-ray diffraction studies of reaction mechanisms, such as those involved when a bioactive glass is immersed in a simulated physiological solution, is decribed in this thesis.

Small-angle X-ray scattering has enabled the growth of mesopores to be observed during the foamed sol-gel stabilisation process. *In-situ* simultaneous small and wide angle X-ray scattering measurements of a foam in SBF have shown that the mesoporous network facilitates the rapid growth of relatively high-density HCA, which will therefore eventually replace the initial silicate glass as the material bounding the macropores.

The data presented herein reveal the structure of highly important materials in the field of biomaterials and enable a link to be made between the atomic scale structure of the materials and their bioactive properties.

Presentations and Publications

Conference Poster Presentations

‘X-ray diffraction study of sol-gel derived $(Ta_2O_5)_x(SiO_2)_{1-x}$ glasses’, V FitzGerald, DM Pickup, KO Drake, ME Smith, RJ Newport. Presented at the UK-Ireland sol-gel meeting, London, 2004.

‘The structure of a foamed bioactive calcia-silica sol-gel glass’, V FitzGerald, KM Wetherall, RM Moss, DM Pickup, JR Jones, RJ Newport. Presented at Professor Larry L Hench Retirement Symposium, Imperial College London, 2005.

‘X-ray and neutron diffraction study of Bioglass® supported by reverse Monte Carlo modelling’, V FitzGerald, DC Carta, DM Pickup, RJ Newport. Presented at ‘The first 18 years of reverse Monte Carlo modelling’ conference, Budapest, 2006.

Conference Oral Presentations

‘X-ray and neutron diffraction study of BioGlass® supported by reverse Monte Carlo modelling’, V FitzGerald, DC Carta, DM Pickup and RJ Newport. Presented at The Eighth ESG conference hosted by the Society of Glass Technology, Sunderland, 2006.

‘Time resolved high energy X-ray total diffraction of foamed bioactive calcia silica sol-gel glass immersed *in-situ* in simulated body fluid’, V FitzGerald, KO Drake, JR Jones, ME Smith and RJ Newport. Presented at NCM10, Prague, 2006.

Publications

LJ Skipper, FE Sowrey, V FitzGerald, R Rashid, KO Drake, Z Lin, P Saravanapavan, LL Hench, ME Smith, RJ Newport, ‘Structural studies of bioactivity in sol-gel derived glasses by X-ray spectroscopy’, *J. Biomed. Mater. Res.,* **70**(A), 354-360, 2004.

DM Pickup, I Ahmed, V FitzGerald, RM Moss, KM Wetherall, JC Knowles, ME Smith, RJ Newport, ‘X-ray absorption spectroscopy and high-energy XRD study of the local environment of copper in antibacterial copper-releasing degradable phosphate glasses’, *J. Non. Cryst. Solids.,* **352**, 3080-3087, 2006.

RJ Newport, LJ Skipper, V FitzGerald, DM Pickup, ME Smith, JR Jones, ‘*In vitro* changes in the structure of a bioactive calcia-silica sol-gel glass explored using isotopic substitution in neutron diffraction’, *J. Non. Cryst. Solids.,* **353**, 1854-1859, 2007.

V FitzGerald, DM Pickup, DC Carta, DC Greenspan, RJ Newport, ‘An X-ray diffraction study of the structure of Bioglass and its sol-gel analogue as a function of composition’, *Phys. Chem. Chem. Phys.,* in press.

V FitzGerald, DM Pickup, KO Drake, ME Smith, RJ Newport, ‘A high energy X-ray diffraction study of sol-gel derived $(Ta_2O_5)_x(SiO_2)_{1-x}$ glasses (x = 0.05, 0.11 and 0.25) – elucidating the role of tantalum in silica’, *J. Sol-gel Science and Tech.,* in press.

V FitzGerald, DM Pickup, DC Greenspan , G Sarkar, JJ Fitzgerald, KM Wetherall, RM Moss, JR Jones, RJ Newport, ‘A neutron and X-ray diffraction study of Bioglass® with reverse Monte Carlo modelling’, *Adv. Func. Mater.,* in press.

V FitzGerald, KO Drake, JR Jones, ME Smith, V Honkimäki, T Buslaps, M Kretzschmer, RJ Newport, ‘*In-situ* High Energy X-ray Diffraction Study of a Bioactive Calcium Silicate Foam Immersed in Simulated Body Fluid’, *J. Synchrotron. Rad.,* in press.

V FitzGerald, JR Jones, D Qiu, KM Wetherall, RM Moss, RJ Newport, ‘Bioactive glass sol-gel foam scaffolds: evolution of nanoporosity during processing and in situ monitoring of apatite layer formation using small and wide angle X-ray scattering’, *J. Biomed. Mater. Res. (A)*, submitted.

Contents

List of Tables

List of Figures

Chapter 1

Introduction

Life expectancy in the western world has increased significantly in recent years. This has emphasised the need for new types of prostheses with a life-span of over 30 years. In response to this problem, a new group of materials have been introduced and studied, named biomaterials. First introduced by Hench in 1969, glass/ceramic biomaterials have now been investigated for use as prostheses due to their ability to bond to bone. An exploration of biomaterials is given in Chapter 2, concentrating on bioactive glasses, which are at the heart of this thesis.

Two types of bioactive glass have been chosen as the basis of study: conventional melt-quenched glasses and glasses made via the sol-gel route. A review of the properties of these materials, and previously published work, can be found in Chapter 3.

The techniques employed to study the atomic-scale structure of these materials were high energy X-ray and neutron diffraction, reverse Monte Carlo modelling, grazing incidence X-ray diffraction and small angle X-ray scattering. The theory of these techniques, along with methods of data collection and data analysis can be found in Chapter 4.

The preparation of both the melt-quenched and sol-gel derived glasses is presented in Chapter 5 along with further characterisation techniques used to aid the interpretation of the aforementioned diffraction methods, namely X-ray fluorescence, inductively coupled plasma analysis, Raman and infrared spectroscopy and helium pycnometry.

The first bioactive glasses introduced were melt-quenched glasses containing CaO-SiO_2-Na_2O-P_2O_5. Chapter 6 reports the experimental results for the melt-quenched glasses studied. Results and discussion on the atomic scale structure of the melt-quenched glasses are presented along with an in-depth structural study of the most bioactive of the melt-quenched glasses. Chapter 7 reports the experimental results and presents a discussion of the growth of apatite on the most bioactive of the melt-quenched glasses, the latter including a comparison between two popular solutions used to investigate the *in-vitro* bioactive behaviour of bioactive glasses, one a standard cell culture medium and one a simulated physiological solution.

Interest has been growing in glasses with simpler compositions, as research has proven that Na_2O and P_2O_5 are not needed for the glass to bond to bone. Therefore, binary glasses containing only SiO_2 and CaO were produced which were also highly bioactive, and made via the sol-gel route. The sample investigated in this thesis is of high interest due to the foaming of the sol during the sol-gel process. This produces a scaffold for bone regeneration, which has both macro- and mesopores, meaning the scaffold has similar structure to that of trabecular bone. Chapters 8 and 9 report the structural analysis of foamed binary calcia-silica sol-gel bioactive glasses, with Chapter 9 focusing in particular on the role of mesopores in the glass (known to be connected to the high bioactivity of the materials, as they contribute most heavily to the surface area of the glass).

Chapter 10 summarises the conclusions drawn from Chapters 6-9, on both the melt-quenched and the sol-gel derived bioactive glasses.

Chapter 2

Bioactive materials

2.1 Introduction

Life expectancy for both men and women has continued to rise. In 2002, life expectancy at birth for females born in the UK was 81 years, compared with 76 years for males. This contrasts with 49 and 45 years respectively at the turn of the last century in 1901. In recent years, the increase in life expectancy among older adults has been dramatic, particularly for men. Between 1981 and 2002, life expectancy at age 50 increased by four and a half years for men and three years for women. For those aged 65 and over the extra years of life were three years and two years respectively. By 2002, women who were aged 65 could expect to live to the age of 84, while men could expect to live to the age of 81. Projections suggest that life expectancies at these older ages will increase by a further three years or so by 2020. The expectation of life for people at 70 and 80 has also gone up. At present there are a greater number of older people aged 70 and 80 than ever before.[2.1] This improvement may be related to better nutrition and improvements in medical care, improved vaccinations, drugs and water treatments. Due to this, millions of people now make use of implants or transplants to maintain their quality of life, as they grow older, due to illnesses or accidents.

Orthopaedic prostheses made of bioinert (biologically inactive) materials are currently used with excellent 15 year survivability of 75-85%. However, due to the aforementioned longer life expectancy, an increasing percentage of the population need greater than 30 year survivability of devices. [2.2] The two solutions to this growing need are 1) to increase the lifetime of current prostheses, or 2) to develop alternative means of orthopaedic treatment which do not require implants.

Solution 2 brings us to the bioactive alternative. During the last decade, a new group of materials that can form a bond to bone have been investigated. These biomaterials can augment, repair or replace parts of the human body by stimulating genes which initiate the repair process.

2.2 Bioactive Materials

The last four decades have seen the innovative use of specially designed ceramics for the repair and reconstruction of damaged or diseased parts of the body. Ceramics used for this purpose are called bioceramics. Many ceramics have been tested [2.3-2.5] however only few have been suitable for human clinical applications.

A bioactive material is one that elicits a specific biological response at the interface of the material which results in the formation of a bond between the tissues and the material [2.6]. Clinical success depends on two properties of the material; 1) its ability to form a stable interface with connective tissues; 2) its ability to mimic the mechanical behaviour of the tissue to be replaced. The mechanism of tissue attachment has been shown to be directly related to the type of tissue response at the implant interface [2.3]. There are four types of tissue response as shown in Table 2.1. These four types of response determine the different means of attachment of prosthesis to the musculo-skeletal system. Table 2.2 gives details of these attachment mechanisms along with some examples of materials that achieve the types of attachment.

If the material is toxic, the surrounding tissue dies.
If the material is non-toxic and biologically inactive (nearly inert), a fibrous tissue of variable thickness forms
If the material is non-toxic and biologically active (bioactive), an interfacial bond forms.
If the material is non-toxic and dissolves, the surrounding tissue replaces it.

Table 2.1: Types of implant-tissue response, [2.6]

The materials concentrated on in this study are materials of type 3 in Table 2.2. In 1969 it was shown by L Hench *et al.* [2.7] that a bioactive glass containing SiO_2, Na_2O, CaO and P_2O_5 in specific proportions, bonded to bone. Since then many bioactive glasses and ceramics of different composition and preparation methods have been produced and investigated for the use as prosthetic implants.

Type of bioceramic	Type of attachment	Example
1	Dense, nonporous, nearly inert ceramics attach by bone growth into surface irregularities by cementing the device into the tissues, or by press fitting into a defect (termed morphological fixation).	Al_2O_3 (single crystal and polycrystalline)
2	For porous inert implants bone ingrowth occurs, which mechanically attaches the bone to the material (termed biological fixation).	Al_2O_3 (porous polycrystalline) Hydroxyapatite-coated porous metals
3	Dense, surface-reactive ceramics, glasses and glass-ceramics attach directly by chemical bonding with the bone (termed biological fixation)	Bioactive glasses Bioactive glass-ceramics Hydroxyapatite
4	Dense, nonporous (or porous), resorbable ceramics are designed to be slowly replaced by bone.	Calcium sulphate Tricalcium phosphate Calcium phosphate salts

Table 2.2: Types of bioceramics – Tissue attachment and bioceramic classification, [2.6].

2.3 Surface reaction kinetics of bioactive glasses and ceramics

In 1988 studies showed that bioactive glasses and ceramics, upon implantation, begin a time-dependant kinetic modification of the surface. This reaction creates a biologically active hydroxycarbonate apatite (HCA) layer at the surface, which provides the bonding interface with tissues. [2.8, 2.9] There are five reaction stages outlined below for a single phase amorphous or glassy material [2.6].

[**1**] Rapid exchange of Na^+ or K^+ with H^+ or H_3O^+ from solution:

$\mathrm{Si\text{-}O\text{-}Na^{+}+H^{+}+OH^{-}} \rightarrow \mathrm{Si\text{-}OH^{+}+Na^{+}}$ (solution)$\mathrm{+OH^{-}}$

This stage is usually controlled by diffusion and exhibits a $t^{-1/2}$ dependence.

[**2**] Loss of soluble silica in the form of $Si(OH)_4$ to the solution, resulting from breaking of Si-O-Si bonds and the formation of Si-OH (silanols) at the glass solution interface:

$\mathrm{Si\text{-}O\text{-}Si + H_2O} \rightarrow \mathrm{Si\text{-}OH+OH\text{-}Si}$

This stage is usually controlled by interfacial reaction and exhibits a $t^{1.0}$ dependence.

[**3**] Condensation and repolymerisation of a SiO_2 rich layer on the surface depleted in alkalis and alkali-earth cations:

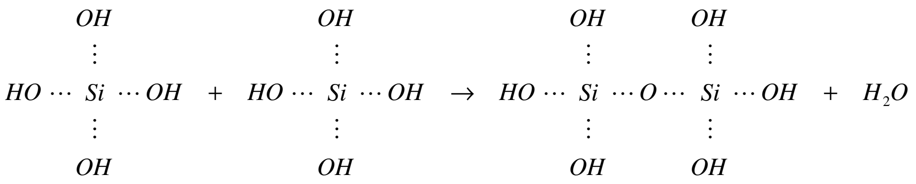

$$HO\cdots \underset{\underset{OH}{\vdots}}{\overset{\overset{OH}{\vdots}}{Si}}\cdots OH \;+\; HO\cdots \underset{\underset{OH}{\vdots}}{\overset{\overset{OH}{\vdots}}{Si}}\cdots OH \;\rightarrow\; HO\cdots \underset{\underset{OH}{\vdots}}{\overset{\overset{OH}{\vdots}}{Si}}\cdots O\cdots \underset{\underset{OH}{\vdots}}{\overset{\overset{OH}{\vdots}}{Si}}\cdots OH \;+\; H_2O$$

[**4**] Migration of Ca^{2+} and PO_4^{3-} groups to the surface through the SiO_2 rich layer forming a $CaO-P_2O_5$-rich film on top of the SiO_2 rich layer, followed by growth of the amorphous $CaO-P_2O_5$-rich film by incorporation of soluble calcium and phosphates from solution.

[**5**] Crystallisation of the amorphous $CaO-P_2O_5$ film by incorporation of OH^-, CO_3^{2-}, or F^- anions from solution to form a mixed hydroxyl carbonate fluorapatite layer.

Stages 1 and 2 have been studied extensively, whereas measurements of stages 3 to 5 are less extensive, although fairly conclusive.

The five stages outlined above do not depend on the presence of tissue, as they occur on the material side of the interface. In 1997, Hench [2.10] summarised the reaction mechanisms associated with the formation of interfacial bonding to bone, stages 6-11 below.

[6] Adsorption of biological moieties (proteins from the blood and tissue fluids from the wound site) in the SiO_2–HCA layer.

[7] Action of macrophages. Macrophages are cells derived from circulating white cells (monocytes) and have the ability to remove foreign material (i.e. dead tissue, bacteria and other particulates) at the wound site. During this stage the wound is cleaned by the macrophages and new blood vessels begin to enter the nearby tissue.

[8] Attachment of mesenchymal cells. These are the wound–healing cells and are the first cell type to interact with the implant.

[9] Differentiation of mesenchymal cells. During this stage, the mesenchymal cells proliferate (increase in numbers) and differentiate (assume specialised forms distinguished by morphology and function) into osteoblasts (bone growing cells).

[10] Generation of matrix. The osteoblasts produce and lay down collagen fibres in a random fashion.

[11] Mineralisation of matrix. The collagen fibres become more organised and matured leading to new bone.

The reaction stages 1-11 outlined above occur on a different timescale depending on the index of bioactivity I_B of the bioactive material. Hench [2.6] introduced the bioactive index as being the time it takes for more than 50% of the interface to be bonded ($t_{0.5bb}$) where

$$I_B = \frac{100}{t_{0.5bb}}. \qquad (2.1)$$

Bioactive materials can be split into two groups, Class A and Class B materials. Class B bioactive materials only elicit an extracellular response at the surface, they do not bond to soft connective tissues and the bond to bone occurs slowly. Most calcium phosphate biomaterials are examples of Class B materials. Class A bioactive materials are both osteoconductive (the implant provides a biocompatible interface along which bone can migrate) and osteoproductive (the colonisation of a bioactive surface by osteogenic cells in a defect environment), the rate of formation of the inorganic silica gel and the HCA layers is more rapid for Class A than Class B, and Class A materials bond to both hard and soft tissues. Class A materials are resorbed as new bone is formed and the newly regenerated bone is mechanically equivalent to normal bone. In this thesis materials of both class A and class B are investigated.

Investigations into the bioactivity of these materials involve the use of a simulated physiological body fluid which is a solution emulating human blood plasma. Several solutions have been used in previous literature, the two main examples of which are tris buffer solution (TBS) and simulated body fluid (SBF). The first solution to be used was TBS [2.11], which contains Tris(hydroxymethyl)aminoethane which is buffered to pH 7.25 with hydrochloric acid (a more detailed description of TBS and SBF preparation is given later in the thesis). The most commonly used solution now is SBF, which is a solution containing ions with similar concentrations to that found in human blood plasma. This solution was first used by Kokubo *et al.* to form an HCA layer on apatite-wollastonite (A/W) glass ceramics [2.12]. The reaction mechanisms (1-5) of the glass in SBF were found to be analogous to those proposed by Hench.

2.4 Rate of apatite formation

Many investigations have been carried out to identify factors which affect the rate of apatite formation, as well as the structure and properties of the apatite layer that is formed. The initial pH, ionic strength [2.13] and temperature of the solution used for testing the bioactivity of a material has been shown to have an effect on the rate and even the type of calcium phosphate layer formed on the surface. Using TBS it has been shown that the structure of the apatite layer formed *in-vitro* differed from that formed *in-vivo*. Kokubo *et al.* [2.12] showed that the *in-vitro* behaviour of the implant material closely matched that of the implant material *in-vivo* when SBF was used as the testing solution. Zhong and Greenspan found that when investigating Bioglass® immersed in SBF the nucleation of an apatite layer was rapid compared to that in TBS, however the crystal size was smaller than that formed in TBS.

The results described above led to the standard characterisation requirement for glasses and glass ceramics, namely that the glass/glass ceramic develops a fully crystallised HCA reaction layer within a specified period of time (20 hours) when exposed to SBF at 37 ºC.

Another factor found to affect the rate of apatite formation is a change in geometry of the implant. A change in the geometry will change the surface area to solution volume ratio (SA/V). Hench *et al.* [2.14] studied the surface reactions of bioactive glasses compared with an inactive glass, and the *in-vitro* studies demonstrated that stages 1-5 of the reaction kinetics depend on glass composition and reaction conditions including the SA/V ratio and the form of the material, i.e.; particulate or bulk glass. The effect of SA/V ratio on the rate of dissolution of 45S5 Bioglass® in TBS was investigated by Greenspan *et al.* [2.15]. At high SA/V ratio, the Ca–P layer formed rapidly but remained thin over time (i.e. rapid nucleation but slow growth). At lower SA/V ratios the nucleation of the Ca–P layers was slower. However, the final thickness of the HCA layer after 20 hours in TBS was greater than that of high SA/V ratio specimens.

Throughout this project when powders were tested for bioactivity, the ratio of 0.075 g per 50 ml of solution was used. This ratio was optimised by US Biomaterials (the original spin-out company from L.L. Hench's seminal work, and from which has come Novamin – the company supplying certain of the samples studied herein) for quality assurance purposes and is routinely used for 45S5 Bioglass® and the gel-derived bioactive glass compositions. It is based upon the analytical studies of Warren *et al.* [2.16]. This ratio was also confirmed to be in the optimum range for bioactive glass dissolution by Jones *et al.* [2.17].

Until the late 1980s bioactive glasses were generally melt-derived with most research based on the 45S5 Bioglass® composition, A/W glass-ceramics or synthetic hydroxyapatite (HA). The rapid rate of HCA formation exhibited by the Bioglass® was attributed to the presence of Na_2O and other alkali and alkali earth ions in the glass composition. Addition of other multivalent ions such as aluminium or boron, stabilised the glass structure (by eliminating the non-bridging oxygens) and served to retard the rate of HCA formation [2.18].

It is widely accepted that increasing silica content of melt derived glass decreases the rate of dissolution. This is due to the reduction in the concentration of network modifier ions present in the glass structure, which serve to disrupt the network resulting in faster network breakdown. Studies by Greenspan *et al.* [2.19, 2.20] revealed that melt derived bioactive glasses with more than 60 mol% silica were biologically inactive.

Li *et al.* showed that CaO-P_2O_5-SiO_2 glass powders produced by a sol-gel technique are more bioactive than the melt derived glasses of the same composition [2.21] (The sol-gel method is a low-temperature method for generating glass, and a detailed explanation of the sol-gel method can be found in Brinker & Scherer [2.22]; pertinent details are provided later in this thesis). The higher bioactivity and the higher rate of dissolution of the sol-gel derived glasses is related in part to the textural features of the gels i.e. pore size and pore volume associated with the large surface area [2.23, 2.24]. It has also been reported that this synthesis method expanded the

SiO_2 content range in which bioactive behaviour could be observed, from an upper limit of 60 mol% in melt derived quaternary bioactive glasses to 85 mol% in ternary sol-gel derived bioactive glasses [2.21]. This also dispels the theory that Na_2O is a critical component of the bioactive glass compositions, as all ternary bioactive glasses contained no Na_2O.

The role of phosphate in bioactive glasses is also interesting. Early on it was assumed that P_2O_5 was required for a glass to be bioactive. In the early nineties Kokubo *et al*. [2.25, 2.26] proved that as well as the quaternary and ternary glasses, P_2O_5 free ceramics in the binary system CaO-SiO_2 also showed *in-vitro* and *in-vivo* bioactivity with a maximum SiO_2 content of 65 mol%. The role of phosphate in the glass appears only to aid in the nucleation of the Ca–P phase on the surface but is not a critical constituent because the surface will adsorb phosphate ions from the body fluid and incorporate them into the growing HCA layer. Although Ca ions are also present in the SBF, the ionic concentration is lower than that is needed for both heterogeneous and homogeneous precipitations of HCA [2.27].

There are several methods that can be used to characterise the formation of apatite on the surface of a bioactive material [2.18]. Two of the common methods are inductively coupled plasma atomic emission spectrometry (ICP-AES) and Fourier transform infrared (FTIR) spectroscopy. An HCA layer can also be characterised using X-ray diffraction (XRD), scanning electron microscopy coupled with energy dispersive X-ray spectroscopy (SEM-EDS) and transmission electron microscopy (TEM).

Using the ICP technique it is possible to follow the dissolution mechanism of the surface. Ionic concentrations of silicon and calcium ions can be quantified at different times and thus a rate of dissolution (i.e. rate of ion exchange –Stage 1– and rate of surface network disruption –Stage 2) can be determined. At the same time using the phosphate concentration in the surrounding SBF, the rate of apatite formation can also be quantified. However, this technique does not confirm that the resultant products of the surface reactions are actually a polycrystalline, apatite (HCA).

To confirm the formation of an apatite layer, it is common practice to analyse the surface of the implant material using FTIR. It is possible to observe the nucleation and growth of apatite using this technique even though it is not usually quantifiable.

These two characterisation techniques are sufficient for analysing apatite formation, particularly for quality assurance purposes if the characterisation programs are standardised. However, when new materials are being tested for bioactivity it is necessary to perform other surface analysis tests to confirm the structure and the composition of the newly deposited apatite layer.

XRD analysis is usually performed on the crystalline surface of the material after immersion in SBF, or other simulated physiological solution to confirm the surface layer is similar to that of the apatite structure in bone mineral. SEM–EDS is another technique used to observe the surface microstructural features and their dimensions and area fractions can also be measured. The composition can be chemically analysed with EDS to confirm that the ratio of Ca/P is similar to that found in natural bone.

Many other techniques can be utilised to study these materials. In the next chapter, an outline of previous experiments carried out on each type of material studied within this thesis will be given, along with a description of the work produced in this thesis for each type of material.

References

[2.1] National statistics online www.statistics.gov.uk

[2.2] Hench, L.L., Jones, J.R., Sepulveda, P., **Bioactive materials for tissue engineering scaffolds**, In: Polak,J.M., Hench,L.L., Kemp,P., editor, Future Strategies for Tissue and Organ Replacement, London, Imperial College Press, 2002, Pages: 3 - 24, ISBN: 1-8609-4311-X.

[2.3] Hench, L.L., Ethridge, E.C., Biomaterials: An interfacial approach. Academic Press, New York, 1982.

[2.4] Preston, J.D., *Properties in Dental Ceramics*. In Proceedings of the IVth international Symposium on Dental Materials. Quintessa Publishing, Chicago, IL, 1988.

[2.5] Hulbert, S.F., Bokros, J.C., Hench, L.L., Wilson, J., Heimke, G., *Ceramics in clinical applications: Past, Present and Future*. pp. 189-213 in High Tech Ceramics. Edited by P Vincenzini. Elsevier, Amsterdam, Netherlands, 1987.

[2.6] Hench, L.L., *J. Am. Ceram. Soc.,* **74**(7), 1487-1510, 1991.

[2.7] Hench, L.L., Splinter, R.J., Allen, W.C., Greenlee, T.K., *J. Biomed. Mater. Res.,* **2**(1), 117-141, 1972.

[2.8] Hench, L.L., 'Bioactive ceramics' p. 54 in Bioceramics: Materials characteristics versus in vivo behaviour, Vol 523, Ed P Ducheyne and J Lemons. Annals of New York Academy of Sciences, New York, 1988.

[2.9] Grosse, U., Kinne, R., Schmitz, H.J., Strunz, V., Crit, C.R.C., *Rev, Biocompat*, **4**, 2 1988.

[2.10] Hench, L.L., *Solid State & Materials Science*, **2**, 604-610, 1997.

[2.11] Kim, C.Y., Clark, A.E., Hench, L.L., *J. Non. Cryst. Solids.,* **113**, 195-202, 1989.

[2.12] Kokubo, T., Kushitani, H., Sakka, S., *Journal of Biomedical Materials Research*, **24**, 721-734, 1990.

[2.13] Cerruti, M., Greenspan, D., Powers, K., *Biomaterials,* **26**, 1665-1674, 2005.

[2.14] Hench, L.L., Andersson, Ö.H., La Torre, G.P., The kinetics of bioactive ceramics part III: surface reactions for bioactive glasses compared with an inactive glass. Bonfield W, Hastings GW, and Tanner KE. Bioceramics 4, 155-162. 1991. London, UK, Butterworth Heinemann Ltd.

[2.15] Greenspan, D.C., Zhong, J.P., La Torre, G.P. Effect of surface area to volume ratio on in-vitro surface reactions of bioactive glass particulates. Andersson ÖH and Yli-Urpo A. Bioceramics 7, 55-60. 1994. Turku, Finland, Butterworth-Heinemann Ltd.

[2.16] Warren, L.D., Clark, A.E., Hench, L.L. *J. Biomed. Mater. Res.(A),* **23,** 207-209, 1989.

[2.17] Jones, J.R., Sepulveda, P., Hench, L.L., *J. Biomed. Mater. Res.(A),* **58**, 720-726, 2001.

[2.18] Hench, L.L., Wilson, J. Introduction to Bioceramics. In: Hench LL, Wilson J, Eds. *Introduction to Bioceramics.* World Scientific, Singapore 1993: pp.17.

[2.19] Greenspan, D.C., Zhong, J.P., Wheeler, D.L. Bioactivity and Biodegradability: melt vs. sol-gel derived glasses *in vitro* and *in vivo*. Eds: LeGeros RZ, LeGeros JP. *Bioceramics 11.* 1998; 354-348.

[2.20] Greenspan, D.C., Zhong, J.P., Chen, X.F., LaTorre, G.P. The Evaluation of Degradability of Melt and Sol-Gel Derived Bioglass® *in-vitro*. Sedel L and Rey C. Bioceramics 10. 1997.

[2.21] Li, R., Clark, A.E., Hench, L.L. Effects of Structure and surface area on bioactive powders by sol-gel process. In: Hench LL, West JK, Eds. *Chemical Processing of Advanced Materials*. 1992: 627-633.

[2.22] Brinker, C.J., Scherer, G.W., Sol-gel science: The physics and Chemistry of Sol-Gel processing. Academic Press Inc., USA 1990.

[2.23] Pereira, M.M., Hench, L.L. *Journal of Sol-Gel Science and Technology*, **7,** 59-68, 1996.

[2.24] Pereira, M.M., Clark, A.E., Hench, L.L. *Journal of Materials Synthesis and Processing*, **2,** 189-196, 1994.

[2.25] Ebisawa, Y., Kokubo, T., Ohura, K., Yamamuro, T. *Journal of Materials Science: materials in Medicine*, **1,** 239-244, 1990.

[2.26] Ohura, K., Nakamura, T., Yamamuro, T. *et al., J. Biomed. Mater. Res.,* **25,** 357-365, 1991.

[2.27] Pereira, M.M., Clark, A.E., Hench, L.L. *J. Biomed. Mater. Res.,* **28,** 693-698, 1994.

Chapter 3

Bioactive glasses

3.1 Quaternary melt-quenched bioactive glasses

Two types of bioactive glasses have been studied, and are discussed within this thesis. The first are a group of melt-quenched glasses containing SiO_2, Na_2O, CaO and P_2O_5 in specific proportions. The most bioactive of the group, 45S5 (Bioglass®) contains 45 wt% SiO_2, and has a 5 to 1 molar ratio of Ca to P. This set of bioactive glasses was the first investigated for use in the human body. As mentioned previously, Bioglass® was first introduced as a bioactive material by Hench *et al.* in 1969 [3.1]. Bonding to bone was demonstrated for a family of glasses of certain compositional range which contained SiO_2, Na_2O, CaO and P_2O_5. There were three compositional features to these glasses which made the surface highly reactive when exposed to an aqueous medium: (1) less than 60% SiO_2, (2) high Na_2O and CaO content, (3) high CaO/ P_2O_5 ratio. Studies of these glasses showed that the formation of a SiO_2 rich layer and a calcium phosphate film on the bioglass surface in an aqueous environment was associated with the film bonding bioglass to bone. [3.2, 3.3] An investigation into the compositional sensitivity of the glasses was also carried out [3.4], which showed that bonding was favourable within the range of 3-6 wt % of P_2O_5. A further study showed an essential factor for the bonding is the silica content of the bioglass with a compositional boundary between bonding and nonbonding glasses occurring between 55 and 60 mol% SiO_2. [3.5] In 1980, Ogino *et al.* [3.6] showed that depending on the bioglass composition, three types of reaction occur when in a standard cell culture medium (TBS): (1) A calcium phosphate film and

SiO_2 rich layer form simultaneously and the reaction rate is faster for bioglasses with lower SiO_2 content (~45 wt % SiO_2). (2) A SiO_2 rich layer forms first, and a calcium phosphate film develops later between the aqueous environment and the SiO_2 rich layer for bioglasses whose SiO_2 content was between 45-52 wt %. (3) A calcium phosphate film does not form for glasses with SiO_2 content higher than 58 wt %. The formation of a calcium phosphate film on the glass surface in a solution such as TBS is therefore indicative of the ability to bond to bone.

In 1992 Li *et al.* produced ternary glass powders based upon the melt-quenched bioglass family using the sol-gel method of producing glasses [3.7]. This represents the first example of the second major type of bioactive glass discussed within this thesis. The sol-gel method is a low-temperature, chemical method for generating glass, and a detailed explanation of the sol-gel method can be found in Brinker & Scherer [3.8]. The glasses produced contained CaO, P_2O_5 and SiO_2, and these sol-gel glasses were more bioactive than their melt-quenched counterparts. In 1994 Pereira *et al.* investigated the calcium phosphate formation on these sol-gel derived bioactive glasses, and showed that for all compositions a HCA layer was formed within 8 hours immersion time in SBF and TBS, with the HCA layer growing more rapidly in the SBF solution. [3.9] The sol-gel glasses produced were shown not only to be more bioactive, but also showed a higher rate of dissolution, due to their higher surface area as a result of pore size and pore volume (and most probably also due to the high concentration of surface hydroxyl groups). [3.10] These materials had the ability to resorb at a similar rate to the bone formation, whereas the melt-quenched glasses did not. The sol-gel glasses are processed at lower temperatures and the process allows control of their pore structure, which permits better control of their bioactivity and biodegradability. The absence of Na_2O in the glasses avoids the rapid change in interfacial pH observed with melt-quenched glasses, and the high specific surface area rich in silanol groups obtained *in-situ* allows a more rapid nucleation of a biologically active HCA layer.

In 1998 Rehman *et al.* investigated the *in-vitro* reaction layers formed on Bioglass® using thin film XRD and FTIR-attenuated total reflectance microspectroscopy (ATR-FTIR) [3.11]. The simulated physiological solution used in the experiments was that used by Kokubo *et al.* [3.12], designated SBF K-9 by Filgueiras *et al.* [3.13]. The results agreed with previous data showing that a calcium phosphate rich phase formed on the top of the silica rich gel layer, FTIR data showed that the carbonate modes were associated with the formation of the crystalline carbonate apatite phase. The FTIR data also showed that the crystallisation of the carbonate apatite layer took place in steps, and they also showed that the layer is deposited initially with preferred orientation, that with time reduces as crystal growth becomes more random.

In 2000, Zhong and Greenspan outlined the processing and properties of sol-gel bioactive glasses. They investigated the properties of 58S, 77S and 100S sol-gel glasses (containing 58, 77 and 100 wt% SiO_2 respectively) and used 45S5 Bioglass® as a comparison [3.14]. The paper outlines a method to produce homogeneous and stable micro-porous high surface area sol-gel bioactive glasses. The study showed that the 58S sol-gel glass had a greater rate of HCA formation than the most bioactive of the melt-quenched glasses 45S5. The 77S sol-gel glass showed HCA formation after only 1 day in SBF and the 100S sol-gel glass did not exhibit any HCA growth after 1 day which indicated the presence of Ca and P are critical for the early induction of HCA growth. The 58S and 77S sol-gel glasses were investigated further by Hamadouche *et al.* exploring the long term *in-vivo* bioactivity and degradability of bulk sol-gel derived glasses in a rabbit model [3.15]. The study showed that degradability was observed for the sol-gel glasses but not for the 45S5 melt-derived sample. The paper proved that in the long-term sol-gel glasses maintained their bioactive properties, however biodegradability increased with time. The bulk sol-gel glass proved to be resorbable, being replaced by newly formed bone, whilst maintaining its bioactive behaviour over time.

In 2001, Jones *et al.* [3.16] investigated the dose-dependant behaviour of bioactive glass dissolution (the concentration of glass to simulated body fluid), for melt-derived 45S5 and sol-gel derived 58S bioactive glasses. The concentrations of elements leached into the surrounding dissolution medium were measured using inductively coupled plasma (ICP) analysis, and the growth of HCA on the surface was measured using FTIR. The results showed that the rate of HCA formation on both types of glass powders *in vitro* depends on the concentration of the powders in solution. The data showed that for the melt-quenched 45S5 glass HCA formation was inhibited at glass concentrations above 0.002 gml^{-1} in SBF. For the 58S sol-gel glass the critical concentration was 0.0015 gml^{-1} in SBF. Throughout this thesis, when dealing with powdered glass being reacted in SBF or TBS, 0.075 g of powder was immersed in 50 ml of SBF or TBS. This corresponds to a concentration of 0.0015 gml^{-1}, which is in the range where HCA formation is not inhibited for either types of glass.

Sepulveda *et al.* [3.17] continued this work, investigating the *in-vitro* dissolution of 45S5 and 58S bioactive glasses. The effects of powder type, particle size and type of dissolution medium were investigated using ICP and FTIR. Two dissolution mediums were used, SBF and α-MEM (a cell culture medium). It was found that lower dissolution rates occurred in the culture medium compared to the SBF, and the subsequent delay of surface layer formation was attributed to the presence of proteins from serum in the culture media. The melt-derived and gel-derived glasses both showed dissolution behaviour that was directly correlated to their particle size range, with dissolution rate increasing as particle size decreased. The change in exposed area could lead to the control of dissolution rate of the silica network. The deposition of the calcium phosphate however appeared to be more closely related to the powder type than to the particle size. In summary, it had been demonstrated that varying particle size, glass type and volume fraction of powder in fluid allowed one to control dissolution rates and bioactivity levels.

In 2002 Zhong *et al.* [3.18] observed that when Bioglass® was tested *in-vitro* in SBF, apatite crystals not only formed on its surface but also in the reaction solutions. The crystals formed in the reaction solution appeared identical in morphology and structure with those formed on the Bioglass® surface.

Arcos *et al.* [3.19] used the activation energy for silicon release to determine the bioactivity of a glass. Two melt-derived glasses (45S5 and 60S5) and four sol-gel derived glasses (58S, 68S, 77S and 91S) were investigated. The relationship between activation energy for silicon release and bioactivity was explained in terms of the influence of chemical composition, textural properties and structural density on silanol group formation and silicon dissolution. The measurements provided a quantitative method to evaluate the *in-vitro* bioactivity of the silica based glasses.

In 2002 Kontonasaki *et al.* [3.20] investigated the growth of the HCA layer on PerioGlas®. PerioGlas® is a commercially available Bioglass® Synthetic Bone Graft Particulate which has been used successfully as an alloplast for treatment of osseous defects and bone loss in periodontal disease. [3.21] PerioGlas® powder of particle size 20-63 µm was soaked in SBF (Kokubo *et al.* [3.22]) and then studied using FTIR and SEM. The results showed the formation of an amorphous calcium phosphate rich layer on the surface after 12 hours, and a well crystalline HCA layer after 24 hours in SBF.

In 2004 Cerruti *et al.* [3.23] studied the effects of pH and ionic strength on the reactivity of 2 µm sized particles of Bioglass®. The results showed that when the pH was higher than 8, calcium phosphate precipitation occurred immediately after the immersion and prevented any further large ion release. Calcium carbonate was formed more than HCA under these conditions. At lower pH, no phosphorus reprecipitation occurred within the first two days of immersion, and total breakdown of the glassy network occurred. Only at a pH of 8 or lower would a significant amount of phosphate reprecipitate. These results were comparable to results obtained when immersing particles of Bioglass® in SBF.

Further to this study, Cerruti *et al.* [3.24] analysed the early stages of reactivity of three different particle sizes of Bioglass® as well as bulk Bioglass®. Ion release and pH variations were observed and the results demonstrated that differences in initial surface area influenced the increase in pH, the rate of elemental release and the rate of calcium phosphate reprecipitation. The larger particles obtained a thicker calcium phosphate layer after immersion in TBS. Their paper presents an analytical model for cation release based on a two-step mechanism.

Cerruti *et al.* [3.25] used BET surface area theory and pore size distribution analysis to study the modifications in specific surface area (s.s.a.) and porosity of Bioglass® particles during reaction in TBS. Particles of 2 and 90 μm were investigated and it was found that a significant increase in s.s.a. occurs in the course of dissolution of the Bioglass® particles, however the ratio between starting s.s.a. of the two samples was not maintained throughout the dissolution, indicating that the starting s.s.a. cannot be used as a suitable parameter to normalise dissolution rates. A microporous system was observed, which appeared earlier on the 2 μm Bioglass® particles, and which depended on ion release from the glassy network into solution. After some time, the micropores were occluded by the precipitation of a calcium phosphate layer. High resolution transmission electron microscopy (HR-TEM) and energy dispersive spectrometry (EDS) analysis showed that the high surface area measured on reacted samples was related to the formation of a complex articulated Ca/P rich structure as well as to the microporous silica layer. The microcrystalline Ca/P rich structure was observed in the proximity of denser amorphous SiO_2 particles, confirming that SiO_2 can act as a nucleation point for the Ca/P-rich layer. They concluded that not only hydroxyapatite, but other types of calcium phosphates were formed after only a few hours reaction.

Recently Cormack *et al.* performed some molecular dynamics studies on bioactive glasses [3.26, 3.27]. The first study focused on the dissolution energy of the glasses. The dissolution energy was shown to vary considerably depending on the nature and environment of the Si-O-Si bond being broken, however no correlation between this and bioactivity was found, suggesting network disruption is a necessary process but not rate determining. The second study, using a new potential model incorporating polarization effects, investigated the structure of three melt-quenched bioactive glasses, namely 45S5, 55S5 and 65S5. The study found that the phosphate groups were predominantly isolated as orthophosphate units, and that the silica network was made up of Q^2 and Q^3 species.

In this thesis further study of this group of bioactive glasses is presented. Although much research has been done on this group of materials, their structure is still not fully understood. X-ray diffraction has now been used as a structural characterisation tool in order to compare the atomic scale structures of four melt-quenched bioactive glasses, namely 45S5, 52S5, 55S5 and 60S5 along with 77S a sol-gel derived bioactive glass for comparison. Along with this, an in-depth structural analysis has been carried out on 45S5, the most bioactive composition of the melt-quenched glasses. Several characterisation techniques were used in unison, high energy X-ray and neutron diffraction, nuclear magnetic resonance (NMR), and reverse Monte Calro (RMC) modelling to create one structural model of Bioglass®. A grazing incidence X-ray diffraction study has been carried out to compare the surface reactions of three melt-quenched glasses when reacted in TBS. Also, an X-ray diffraction study of Bioglass® reacted in SBF for various periods of time is presented along with the same experiment carried out in TBS to allow a direct comparison of SBF and TBS.

3.2 Binary calcia silica sol-gel bioactive glasses

As mentioned in Chapter 2, binary calcia silica sol-gel glasses have been shown to be bioactive [3.28, 3.29]. In 2000 Martinez *et al.* [3.30] studied glasses in the CaO-SiO_2 binary system, i.e. containing no sodium or phosphorus, with varying silica content (50-90 mol%). The glasses were characterised using thermogravimetric analysis (TGA) and differential thermal analysis (DTA), Fourier transform infrared spectroscopy (FTIR), X-ray diffraction (XRD), scanning electron microscopy (SEM) and energy dispersive spectroscopy (EDS). Clear differences were observed in composition, specific surface area and porosity between the low SiO_2 content glasses (50-70 mol%) and the high SiO_2 content glasses (80-90 mol%). *In-vitro* bioactivity for all glasses was investigated by soaking samples in SBF at 37 °C. It was proven that, for these Na_2O- and P_2O_5 free glasses, a hydroxycarbonate apatite (HCA) layer formed when they were immersed in SBF. The formation of this layer proved to be a function of composition, with lower SiO_2 content glasses forming the HCA layer more quickly. In the 50 and 60 mol% SiO_2 glasses a calcite layer was shown to grow, along with the amorphous calcium phosphate layer, after 1.5 hours in SBF. The 70 mol% glass showed evidence that the apatite phase was the predominant feature.

In 2001 Saravanapavan and Hench produced a study outlining the low temperature synthesis, structure and bioactivity of gel derived glasses in the binary CaO-SiO_2 system [3.31]. The glasses were made via a slightly different method to that of Martinez *et al.* [3.30], however with the same components. Glasses containing between 0 and 50 mol % CaO were produced and investigated. As observed before [3.30], all glasses were found to be bioactive, and formed a hydrated carbonate apatite layer on their surface when exposed to SBF. The results showed that all five reaction stages outlined in Chapter 2 occurred within the first 24 hours immersion time, and thus the materials exhibit a similar level of bioactivity to that observed in ternary $CaO-SiO_2-P_2O_5$ glasses, further confirming that P_2O_5 is not essential to produce a bioactive glass. The growth of the HCA layer was shown to depend on textural properties as well as the composition of the glass. Glasses with larger surface area and smaller pore sizes were those with higher CaO content. The results showed that the glass containing the most (50 mol%) CaO resorbs rapidly, hindering the growth of the HCA, and the glass containing the least (90 mol%) CaO had a slow rate of glass dissolution and hence a slow rate of HCA formation. Of the other three compositions examined, the glass containing 70 mol% CaO appeared to be the most bioactive.

Further studies on these binary sol-gel glasses by Saravanapavan and Hench [3.32, 3.33] led to a description of a method to prepare crack free monoliths, of various sizes, with yields of up to 90%, by controlling thermal treatment during the ageing and drying stages of the sol-gel process. The laboratory-based characterisation techniques described above confirmed that only calcium oxide and silica were present in the glasses, with no traces of organic matter or nitrates. The gels were confirmed to be amorphous glasses even after stabilisation at 600 °C, with crystallisation temperatures of above 850 °C. When sintered at 1000 °C the gel-glasses were shown to form calcium phosphate phases in accordance to the $CaO-SiO_2$ phase diagram. The sol-gel monoliths produced via the method described in the paper by Saravanapavan and Hench [3.32] were shown to be homogeneous and of high purity. The textural features of these glasses were then investigated. Their results showed that the pores in these gel-glass monoliths were of non-perfect cylindrical shape of varying sizes in the mesopore range, with sizes dependent on the composition of the gel. Their data indicate that the pore system of these glasses consists of a 3-dimensional network of cavities (pores) interconnected by constrictions (throats). The surface area increases, whereas the pore size decreases as the CaO content is reduced. The skeletal and bulk densities were both shown to increase when CaO content decreases, and all gel-glasses were shown to be of ~ 30% porosity [3.33].

In 2003 Saravanapavan *et al.* [3.34] investigated the bioactivity of the aforementioned binary gel-glasses in direct comparison with ternary (CaO-SiO_2-P_2O_5) and quaternary (CaO-SiO_2-P_2O_5-Na_2O) glasses. The main conclusion of their work was that the binary gel-glass of composition 30 mol% CaO and 70 mol% of SiO_2 can be designated a Class A bioactive glass and has comparable bioactivity to 45S5 Biolass® (a quaternary melt-quenched glass) and 58S (a ternary sol-gel glass). The first four reaction stages of a bioactive glass when immersed in a physiological fluid, outlined in Chapter 2, were shown to occur in the first 30 minutes of immersion time in SBF, and corroborated by the observed reduction in particle size in the same time period. The fifth stage was shown to occur between 3 and 6 hours in SBF.

In 2005 Pickup *et al.* [3.35] used an advanced materials characterisation methodology to study a range of sol-gel glass materials. Neutron diffraction with isotopic substitution (NDIS) and isotope-enriched magic angle spinning nuclear magnetic resonance (MAS NMR) was used to study the calcium environment in bioactive binary calcia-silica sol-gel glasses. The results showed evidence of three Ca-O bond distances, and quantified their respective contributions to the bonding of Ca within the silica network. The data pointed to a complex calcium environment in which the calcium is loosely bound at the surface of the network. The data provided a direct atomic scale explanation for the empirical observation that calcium loss from these materials is facile and can be achieved by simple ion exchange with simulated body fluid.

Further to this work, Skipper *et al.* [3.36] then performed a high energy X-ray diffraction experiment to observe the nature of the reaction processes initiated when bioactive calcia-silica sol-gel glass is immersed *in-vitro* in simulated body fluid. The study shows complex multi-stage dissolution and mineral growth phases as a function of reaction time between 1 minute and 30 days, leading eventually to the formation of a disordered hydroxyapatite (HA) layer on the glass surface. It was shown that, following immersion in SBF, a rapid initial dissolution of Ca occurs, and the growth of an amorphous calcium phosphate layer is visible within 1 hour of immersion time, which becomes more evident / ordered by 5 hours immersion time. By 10 hours this layer was shown to be replaced by an amorphous hydroxyapatite which developed steadily into a more ordered, although still only poorly crystalline, hydroxyapatite.

In 2002 Sepulveda *et al.* [3.37] developed a foaming process to produce macroporous gel-glasses. This involved foaming small quantities of the sol, to which has been added a surfactant and a gelling agent, using vigorous mechanical agitation. Surfactants act to lower the surface tension of gas-liquid interface, thus making foams thermodynamically stable. The gelling agent catalysed the polycondensation reaction such that gelling of the foamed sol could be controlled to occur directly after casting. The glass foams produced exhibited a hierarchical structure with interconnected macropores (10-500 μm) and a mesoporous framework (pores of 2-50 nm), which is similar to the structure of trabecular bone. The processing route described allows for casting of irregular shapes, large and small, controlled by mould selection.

Saravanapavan *et al.* [3.38] showed that the binary sol-gel glass of composition 30 mol% CaO and 70 mol% SiO_2 was more susceptible to foaming than the ternary 58S bioactive sol-gel glass or a sol-gel glass containing 100 mol% SiO_2, which means that a larger volume was produced for the same foaming parameters. Their study also showed that the binary glass foam provided a large interconnected pore network suitable for tissue engineering applications, and the binary glass foam exhibited greater handling strength compared to the other compositions. The binary gel-glass foam was shown to have similar dissolution behaviour to that of monoliths and powders.

In this thesis further work is presented which was undertaken in order to investigate the atomic scale structure of these important $(CaO)_{0.3}(SiO_2)_{0.7}$ sol-gel bioactive foams. High energy X-ray diffraction studies have been carried out to replicate the X-ray diffraction experiment carried out by Skipper *et al.* [3.36] on unfoamed samples of the same composition. The aim of the experiment is to study any atomic scale differences in structure between foamed and unfoamed samples and to investigate any differences in reaction mechanisms between the two glasses. In addition to this study, a new method for investigating the reaction mechanisms of bioactive glasses using time-resolved *in-situ* high energy X-ray diffraction is described, and this method is used to investigate two $(CaO)_{0.3}(SiO_2)_{0.7}$ sol-gel bioactive foams sintered to different temperatures. To add to this information, small angle X-ray scattering experiments have been undertaken, the first investigating the foam during the sol-gel synthesis process, specifically the drying stage, to observe the incorporation of calcium into the glass network, and the second to investigate the *in-situ* reaction mechanisms of the glass when reacted in SBF.

References

[3.1] Hench, L.L., Splinter, R.J., Allen, W.C., Greenlee, T.K., *J. Biomed. Mater. Res.,* **2**(1), 117-141, 1972.

[3.2] Clark, A.E., Paschall, H.A., Hench, L.L., Harrell, M.S., *J Biomed Mater Res Symp on Materials for Reconstructive Surgery,* Clemson University, Clemson, SC, 1975.

[3.3] Pantano, C.G., Clark, A.E., Hench, L.L., *J Am Ceram Soc.,* **57**(9), 412-413, 1974.

[3.4] Clark, A.E., Solubility and biocompatibility of glass, Ph.D. DISSERTATION, University of Florida, 1974.

[3.5] Walker, M.M., An investigation into the bonding mechanism of Bioglass, M.S. thesis, University of Florida, 1977.

[3.6] Ogino, M., Ohuchi, F., Hench, L.L., *J. Biomed. Mater. Res.,* **14**, 55-64, 1980.

[3.7] Li, R., Clark, A.E., Hench, L.L., *J. Biomed. Mater. Res.,* **28**, 693, 1994.

[3.8] Brinker, C.J., Scherer, G.W., Sol-gel science: The physics and Chemistry of Sol-Gel processing. Academic Press Inc., USA 1990.

[3.9] Pereira, M.M., Clark, A.E., Hench, L.L. *J. Biomed. Mater. Res.,* **28,** 693-698, 1994.

[3.10] Greenspan, D.C., Zhong, J.P., Wheeler, D.L. Bioactivity and Biodegradability: melt vs. sol-gel derived glasses *in vitro* and *in vivo*. Eds: LeGeros RZ, LeGeros JP. *Bioceramics 11,* 354-348, 1998.

[3.11] Rehman, I., Knowles, J.C., Bonfield, W., *J. Biomed. Mater. Res.,* **41**, 162-166, 1998.

[3.12] Kokubo, T., Kushitani, H., Sakka, S., Kitsugi, T., Yamamuro, Y., *J. Biomed. Mater. Res.,* **26**, 1147-1161, 1992.

[3.13] Filgueiras, M.R., LaTorre, G.P., Hench, L.L., *J. Biomed. Mater. Res.,* **27**, 445-453, 1993.

[3.14] Zhong, J., Greenspan, D.C., *J. Biomed. Mater. Res. (A),* **53**, 694-701, 2000.

[3.15] Hamadouche, M., Meunier, A., Greenspan, D.C., Blanchat, C., Zhong, J.P., La Torre, G.P., Sedel, L., *J. Biomed. Mater. Res.,* **54**, 560-566, 2001.

[3.16] Jones, J.R., Sepulveda, P., Hench, L.L., *J. Biomed. Mater. Res.(A)*, **58**, 720-726, 2001.

[3.17] Sepulveda, P., Jones, J.R., Hench, L.L., *J. Biomed. Mater. Res.,* **61**, 301-311, 2002.

[3.18] Zhong, J.P., Greenspan, D.C., Feng, J.W., *Journal of materials Science:Materials in Medicine*, **13**, 321-326, 2002.

[3.19] Arcos, D., Greenspan, D.C., Vallet-Regi, M., *J. Biomed. Mater. Res.,* **65**(A), 344-351, 2003.

[3.20] Kontonasaki, E., Zorba, T., Papadopoulou, L., Pavlidou, E., Chatzistavrou, X., Paraskevopoulos, K., Koidis, P., *Cryst. Res. Technol.,* **37**, 1165-1171, 2002.

[3.21] Low, S.B., King, C.J., Krieger, J., *Int. J. Periodont. Rest. Dent.,* **17**, 359, 1997.

[3.22] Kokubo, T., Kushitani, H., Sakka, S., Kitsugi, T., Yamamuro, T., *J. Biomed. Mater. Res.,* **24**, 721, 1990.

[3.23] Cerruti, M., Greenspan, G., Powers, K., *Biomaterials*, **26**, 1665-1674, 2005.

[3.24] Cerruti, M., Greenspan, G., Powers, K., *Biomaterials*, **26**, 4903-4911, 2005.

[3.25] Cerritu, M., Perardi, A., Cerrato, G., Morterra, C., *Langmuir*, **21**, 9327-9333, 2005.

[3.26] Zeitler, T.R., Cormack, A.N., *J. Crystal Growth*, **294**, 96-102, 2006.

[3.27] Tilocca, A., Cormack, A.N., de Leeuw, N.H., *Chem. Mater.*, **19**, 95-103, 2007.

[3.28] Ebisawa, Y., Kokubo, T., Ohura, K., Yamamuro, T. *Journal of Materials Science: materials in Medicine*, **1,** 239-244, 1990.

[3.29] Ohura, K., Nakamura, T., Yamamuro, T., *et al.*, *J. Biomed. Mater. Res.,* **25,** 357-365, 1991.

[3.30] Martinez, A., Izquierdo-Barba, I., Vallet-Regi, M., *Chem. Mater.*, **12**, 3080-3088, 2000.

[3.31] Saravanapavan, P., Hench, L.L., *J. Biomed. Mat. Res.,* **54**, 608-618, 2001.

[3.32] Saravanapavan, P., Hench, L.L., *J. Non. Cryst. Solids.,* **318**, 1-13, 2003.

[3.33] Saravanapavan, P., Hench, L.L., *J. Non. Cryst. Solids,* **318**, 14-26, 2003.

[3.34] Saravanapavan, P., Jones, J.R., Pryce, R.S., Hench, L.L., *J. Biomed. Mat. Res.,* **66**(A), 110-119, 2003.

[3.35] Pickup, D.M., Sowrey, F.E., Skipper, L.J., Newport, R.J., Gunawidjaja, P., Drake, K.O., Smith, M.E., Saravanapavan, P., Hench, L.L., *Phys. Chem. Glasses.*, **46**, 433-438, 2005.

[3.36] Skipper, L.J., Sowrey, F.E., Pickup, D.M., Drake, K.O., Smith, M.E., Saravanapavan, P., Hench, L.L., Newport, R.J., *J. Mater. Chem.,***15**, 2369-2374, 2005.

[3.37] Sepulveda, P., Jones, J.R., Hench, L.L., *J. Biomed. Mater. Res.,***59**, 340-348, 2002.

[3.38] Saravanapavan, P., Verrier, S., Jones, J.R., Beilby, R., Shirtliff, V.J., Hench, L.L., Polak, J.M., *BioMed. Mater. Eng.,* **14**(4), 467-486, 2004.

Chapter 4

Theory

4.1 Real-space distribution functions

Amorphous structures are devoid of long-range translational periodicity, and hence many of the simplifications included in the structural description of crystals are not applicable. Thus, the unit cell of an amorphous solid can be regarded as being infinite in extent to its boundaries. Due to the degree of randomness characterising non-crystalline structures, a statistical approach is more appropriate. One simplifying feature which can be invoked in the case of amorphous materials is orientational isotropy: averaged over the whole solid, the structural environment at a given distance from a particular type of atom is the same in all directions. Thus if the structure is described in the general case in terms of the radial density function $\rho(\mathbf{r})$, giving the number of atoms between r and $(r+dr)$ from a given atom, in the case of amorphous materials, $\rho(\mathbf{r})$ becomes a one-dimensional function, $\rho(r)$, dependent only on a scalar distance r, as a consequence of orientational isotropy (see Figure 4.1). At large values of r, the radial density function $\rho(r)\rightarrow\rho_0$, which is the average atomic density of the amorphous material and is a constant value. Fluctuations from the average density, ρ_0, are due to the presence of atoms at the corresponding values of r from the arbitrarily chosen centre. A number of real-space distribution functions related to $\rho(r)$ are used to describe the structure of non-crystalline solids. Amorphous materials are conventionally described using an averaged 1-dimensional function called the radial distribution function (RDF). The RDF describes the fluctuation of the number density of atoms with distance from an arbitrary atom in an amorphous material. Below are a number of ways of representing this function:

Radial Distribution Function $J(r) = 4\pi r^2 g(r)$ (4.1)

Total Correlation Function $T(r) = 4\pi r \rho(r)$ (4.2)

Differential Correlation Function $D(r) = 4\pi r[\rho(r) - \rho_0]$ (4.3)

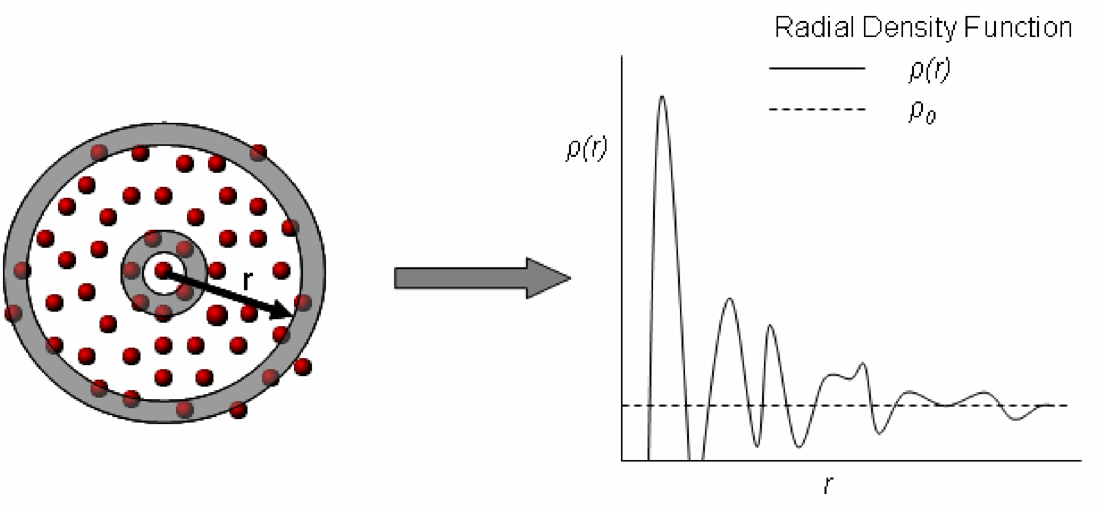

Figure 4.1: Schematic illustration of the structural origin of the density function.

We shall now look at some of these distribution functions in more detail. [4.1] Consider first N fixed identical particles in a volume V, with position vectors $\boldsymbol{R}_i$. The average number density is denoted by

$$n_0 = N / V . \quad (4.4)$$

Only one particle centre can occupy one point, i.e. all points in space are either singly occupied sites or empty, which leads us to the use of the Dirac δ-function. The single particle density function can be written as

$$v_1(\boldsymbol{r}) = \sum_{i=1}^{N} \delta(\boldsymbol{r} - \boldsymbol{R}_i) \qquad (4.5)$$

and hence

$$\int v_1(\boldsymbol{r})\, d\boldsymbol{r} = N . \qquad (4.6)$$

The two particle density function is

$$v_2(\boldsymbol{r}_1, \boldsymbol{r}_2) = \sum_{i}^{N} \sum_{j \neq i}^{N-1} \delta(\boldsymbol{r}_1 - \boldsymbol{R}_i)\,\delta(\boldsymbol{r}_2 - \boldsymbol{R}_j) . \qquad (4.7)$$

This must be zero unless we have particles at $\boldsymbol{R}_i$ and $\boldsymbol{R}_j$. Integrating over $\boldsymbol{r}_2$ will produce a non-zero term whenever $\boldsymbol{r}_2 = \boldsymbol{R}_i \neq \boldsymbol{R}_j$,

$$\int v_2\, d\boldsymbol{r}_2 = (N-1) \sum_{i}^{N} \delta(\boldsymbol{r}_1 - \boldsymbol{R}_1) = (N-1)\, v_1(\boldsymbol{r}_1) . \qquad (4.8)$$

Now a time or ensemble average is taken as these particles may not be fixed. $<v_1(\boldsymbol{r})>$ shall now be denoted as $n_1(\boldsymbol{r})$, so that $n_1(\boldsymbol{r})$ d$\boldsymbol{r}$ then means the average number of particle centres in d$\boldsymbol{r}$, and on the assumption that this cannot be more than unity as particles cannot coincide, $n_1(\boldsymbol{r})$ d$\boldsymbol{r}$ is the probability of finding a particle in d$\boldsymbol{r}$, hence

$$\int_v n_1(\boldsymbol{r})\, d\boldsymbol{r} = N \qquad (4.9)$$

where $n_1(\boldsymbol{r})$ is called the one-particle distribution function.

Likewise, if we average equation 4.8, we find

$$d\boldsymbol{r}_1 \int_v n_2(\boldsymbol{r}_1, \boldsymbol{r}_2)\, d\boldsymbol{r}_2 = (N-1)\, n_1(\boldsymbol{r}_1)\, d\boldsymbol{r}_1 \qquad (4.10)$$

Here $n_2(\boldsymbol{r}_1, \boldsymbol{r}_2)d\boldsymbol{r}_1d\boldsymbol{r}_2$ is the probability of finding particles simultaneously in d$\boldsymbol{r}_1$ and d$\boldsymbol{r}_2$: $n_2(\boldsymbol{r}_1, \boldsymbol{r}_2)$ is the two-particle distribution function.

$n_2(\mathbf{r}_1,\mathbf{r}_2) \neq n_1(\mathbf{r}_1)\, n_1(\mathbf{r}_2)$ because the probability of occupation of $\mathbf{r}_2$ may be affected by that of $\mathbf{r}_1$. The physical basis for this statement is that interatomic forces may be significant over length scales ($\mathbf{r}_1$ - $\mathbf{r}_2$).

A pair distribution function to account for this dependency can now be defined by

$$n_2(\ _1,\ _2) \equiv n_1(\ _1)n_1(\ _2)g_2(\ _1,\ _2) \qquad (4.11)$$

Clearly $g_2 \to 1$ at large ($\mathbf{r}_1$ - $\mathbf{r}_2$) because inter-partial forces decay. We now assume our system is homogeneous, $n_1(\mathbf{r}_1) = n_1(\mathbf{r}_2) = n_0$, then

$$n\mathbf{r}_2(\mathbf{r}_1,\ _2) = n_0^2 g\mathbf{r}_2(\mathbf{r}_1,\ _2)\,. \qquad (4.12)$$

As mentioned before, when dealing with amorphous materials we can assume they are isotropic, then ($\mathbf{r}_1$ - $\mathbf{r}_2$) = $\mathbf{r}$ → r. We can also choose the origin to be at particle 1. Then equations 4.10 and 4.12 give

$$n_0 \int g(r)dr = N - 1\,. \qquad (4.13)$$

So $n_0 g(r)$dr gives the probability of finding a particle at $r \rightarrow r+\mathrm{d}r$ from a particle at the origin.

The average number of particles in a spherical shell centred on a particle at the origin, and dr thick is then

$$\int_{Shell} n_0 g(r)dr = 4\pi r^2 n_0 g(r)dr = n_0 J(r)dr \quad (4.14)$$

where $J(r)=4\pi r^2 g(r)$ is the radial distribution function as described earlier. From equation 4.14 we find the average number of particles surrounding the origin particle out to a distance r_1 is

$$n_1 = n_0 \int_0^{r1} J(r)dr\,. \qquad (4.15)$$

If r_1 includes only the first peak of $J(r)$ then n_1 may be called the number of nearest neighbours which again was described earlier.

Extending this to a binary system of volume V containing N_A type A atoms and N_B type B atoms, the concentrations can be expressed as atomic fractions as follows, $c_A=N_A/N$, $c_A=N_A/N$ and $N=N_A+N_B$.

Take $n_{ij}(r)$ to be the average number density of type j atoms at a distance r from a type i atom. Then

$$g_{ij}(r) = \frac{n_{ij}(r)}{n_0 c_j} = \frac{n_{ij}(r)}{n_j} \qquad (4.16)$$

where $n_0 = N/V$ as in equation 4.4, and $n_j = N_j/V$. Since the numbers of A→B and B→A interparticle distances must be the same, $g_{AB} = g_{BA}$.

$g_{ij}(r)$ is a partial pair distribution function and is the generalisation of $g(r)$ in equation 4.13. For large r, the i-j interaction is negligible so $n_{ij} \rightarrow n_j$ and $g_{ij} \rightarrow 1$. For very small r, $g_{ij} = 0$ because atoms do not interpenetrate. The partial radial distribution function, ρ_{ij} is defined as in equation 4.14 by

$$4\pi r^2 g_{ij}(r) = J_{ij}(r)\,. \qquad (4.17)$$

In analogy with the definition of n_1, the coordination number, we now have four partial coordination numbers, n_{ij}:

$$n_{ij} = n_j \int_0^{r1} J_{ij}(r)dr\,. \qquad (4.18)$$

4.2 X-ray Diffraction theory

4.2.1 Introduction

In order to discover the distribution functions mentioned in the previous section, the structure of real matter must be studied experimentally. This is often realised by undertaking X-ray or neutron scattering experiments, interpreted via diffraction theory. X-rays are electromagnetic radiation with typical photon energies in the range of 100 eV - 100 keV. For diffraction applications, only short wavelength X-rays (hard X-rays) in the range of a few Ångstroms to 0.1 Ångstrom (10 keV - 120 keV) are used. Because the wavelength of X-rays is comparable to the atomic spacing of atoms, they are ideally suited for probing the structural arrangement of atoms and molecules in a wide range of materials. Energetic X-rays can penetrate deep into the materials and provide information about the bulk structure. When X-rays interact with electrons surrounding an atom, X-ray scattering occurs, which may be elastic or inelastic. Inelastic scattering involves the transfer of energy from the incident photons to the electrons in the sample, such that the scattered waves have lower energy and there is no phase relationship between the incident and scattered X-rays, hence an incoherent scattered intensity. Elastic interactions involve direct interactions between the incident and scattering X-rays, where there is no energy transfer and the phases of the incident and scattering X-ray beams remain coherent. This means that the interference between the scattered waves contains only structural information about the sample. Elastic coherent scattering will be considered in the following sections only, for simplicity. A full explanation of X-ray diffraction theory can be found in *Warren* [4.2].

4.2.2 Scattering from a single atom

To calculate the elastic scattering from an atom, we consider that each electron is spread out into a diffuse cloud of negative charge, characterised by a charge density ρ. Hence the quantity ρdV is the ratio of charge in volume dV to the charge of one electron, so for each electron $\int \rho dV = 1$. To get the total amplitude of elastic scattering from one electron, we must integrate over the volume occupied by the electron, and in doing this make proper allowance for the phase of the contribution for each element ρdV. By assuming spherical symmetry for the charge distribution $\rho=\rho(r)$, and taking the origin at the centre of the atom, we can obtain a simple expression for f_e, the amplitude of elastic scattering per electron for a given atom.

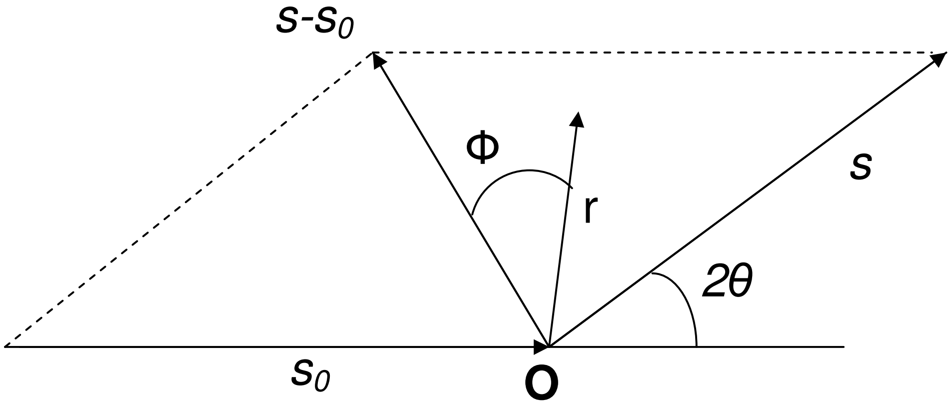

Figure 4.2: Definition of quantities involved with X-ray scattering.

In terms of the quantities shown in Figure 4.2, $(\boldsymbol{s} - \boldsymbol{s_0})\cdot\boldsymbol{r} = 2\sin\theta\, r \cos\Phi$, and using the abbreviation

$$Q = \frac{4\pi \sin\theta}{\lambda}, \quad (4.19)$$

we can write the following expression for f_e [4.1]

$$f_e = \int_{r=0}^{\infty} \int_{\phi=0}^{\pi} e^{iQr\cos\phi} \rho(r) 2\pi r^2 \sin\phi d\phi dr. \qquad (4.20)$$

The integration with respect to ϕ can be performed, giving

$$f_e = \int_0^{\infty} 4\pi r^2 \rho(r) \frac{\sin Qr}{Qr} dr. \qquad (4.21)$$

For an atom with several electrons, f_e becomes the sum of the amplitudes per electron, f:

$$f = \sum_n f_{en} = \sum_n \int_0^{\infty} 4\pi r^2 \rho_n(r) \frac{\sin Qr}{Qr} dr. \qquad (4.22)$$

The quantity f, more commonly known as the atomic scattering factor, plays an important role in X-ray diffraction theory (see below).

4.2.3 Scattering from a condensed material – identical atoms

We will now look at X-ray scattering from a material containing only one type of atom. The intensity from the sample is given by summing the amplitude of the scattering from the different atoms, and then multiplying that sum by its complex conjugate:

$$I_{eu} = \sum_i f_{ai} e^{(i\mathbf{Q}\cdot r_i)} \sum_j f_{aj} e^{(-i\mathbf{Q}\cdot \mathbf{r}_j)} \qquad (4.23)$$

which can be re-written in terms of the difference vector $\mathbf{r}_{ij}=\mathbf{r}_i-\mathbf{r}_j$ as follows

$$I_{eu} = \sum_i \sum_j f_{ai} f_{aj} e^{\boldsymbol{Q}\boldsymbol{r}\cdot{}_{ij})} \qquad (4.24)$$

Now using the average for each exponential term, in terms of *Q =(4πsinθ/λ)*, we can arrive at the Debye scattering equation, since each vector $\boldsymbol{r}_{ij}$ has an equal probability for all possible directions [4.2]

$$I_{eu} = \sum_i \sum_j f_{ai} f_{aj} \frac{\sin Q_{ij}}{rQ_{ij}} \qquad (4.25)$$

For one type of atom, equation 4.24 gives

$$I_{eu} = |\sum_i e^{\boldsymbol{Q}\boldsymbol{r}\cdot{}_{i})}|^2 |f_a|^2 \qquad (4.26)$$

and for *N* identical atoms the structure factor, *S(Q)*, is defined as

$$NS(Q) \equiv |\sum_i e^{\boldsymbol{Q}\boldsymbol{r}\cdot{}_{i})}|^2 . \qquad (4.27)$$

Again we recall that amorphous materials can be treated as isotropic, hence $S(\boldsymbol{Q}) \to S(|\boldsymbol{Q}|) \equiv S(Q)$, and we can combine equations 4.26 and 4.27 to define the intensity of scattering in terms of *S(Q)*:

$$I_{eu} = N |f_a|^2 \; S(Q) \qquad (4.28)$$

Now we can define the structure factor in terms of the pair distribution function *g(r)*, including the fact that the system is isotropic

$$S(Q) = 1 + \rho_0 \int 4\pi r^2 (g(r) - 1)(\frac{\sin Qr}{Qr})dr \qquad (4.29)$$

and we can relate this to an intensity (which will later be associated with the experimentally measured scattering intensity):

$$I_{eu} = Nf_a{}^2 + Nf_a{}^2\rho_0 \int 4\pi r^2 (g(r)-1)(\frac{\sin Qr}{Qr})dr \qquad (4.30)$$

It is now possible to extract structural information in real space from the scattering intensity, via a Fourier transformation, as $g(r)=\rho(r)/\rho_0$.

4.2.4 Scattering from a material – different atom types

We begin with a sample of M types of atom, where i and j represent two of the different types of atom. The atomic scattering factors are f_i and f_j and c_i and c_j are the fractional concentrations of each atom type. If there are N total atoms in the sample, with N_i atoms of type i and N_j atoms of type j, then $c_i = (N_i/N)$ and $c_j = (N_j/N)$. The number density, $\rho_{ij}(r)$, and $g(r)$ can then give us the partial structure factor $S_{ij}(Q)$

$$\int 4\pi r^2 (\rho_{ij}(r) - \rho_0)(\frac{\sin Qr}{Qr})dr \equiv \int 4\pi r^2 \rho_0 (g_{ij}(r)-1)(\frac{\sin Qr}{Qr})dr \equiv S_{ij}(Q)-1 \qquad (4.31)$$

The total pair distribution function $g_T(r)$ can now be defined in terms of $g_{ij}(r)$ to obtain structural information from the scattered intensity.

$$g_T(r)-1 = \sum_{i=1}^{T}\sum_{j=1}^{T} c_i f_i c_j f_j (g_{ij}(r)-1) \quad (4.32)$$

We can now write the intensity for a sample with more than one type of atom.

$$I_{eu} = N\sum_{i=1}^{T} c_i f_i^2 + N\sum_{i=1}^{T}\sum_{j=1}^{T} c_i f_i c_j f_j (S_{ij}(Q)-1) \qquad (4.33)$$

The two components in this function represent the self scattering term, I_{self} ($N\sum_{i=1}^{T} c_i f_i^2$) and the distinct scattering term, $I_{distinct}$ ($N\sum_{i=1}^{T}\sum_{j=1}^{T} c_i f_i c_j f_j (S_{ij}(Q)-1)$). The latter is the more interesting term as it represents the interference between the scattered photons which holds the structural information of the sample. In order to obtain only the distinct scattering term, during X-ray diffraction data analysis, the self scattering is calculated and removed, this process is outlined in Appendix 1 in the section describing the program ANALYSE.

To obtain real space functions of *S(Q)* data, provide information about the structure of the material, a Fourier Transform of the *S(Q)* is performed. The equation below shows the *S(Q)* Foruier transformation into real-space,

$$g(r) = 1 + \frac{1}{2\pi^2 \rho_0} \int Q^2 [S(Q) - 1] \left(\frac{\sin Qr}{Qr}\right) dQ \qquad (4.34)$$

4.3 X-ray diffraction experimental methods

X-ray diffraction experiments were carried out on Station 9.1 at the Synchrotron Radiation Source (SRS), Daresbury and on Station ID15 at the ESRF, Grenoble. The experimental setup of each type of diffraction experiment will be described below.

Station 9.1 at the SRS has two modes of operation, conventional powder diffraction using the 2-circle diffractometer; or, image-plate configurations for either high pressure diamond anvil cell experiments or a curved system (CIP) for diffraction from crystalline powders, liquids and amorphous materials [4.3]. The X-ray experiments carried out in this study used the two circle diffractometer.

In the SRS X-rays are produced by the acceleration of a 2 GeV electron beam in the storage ring. The beam current is about 250 mA at the beginning of the fill and it decays down to about 120 mA at the end of the fill. Station 9.1 is situated about 15 m tangentially from a 5 T multipole superconducting magnet (Wiggler) where X-ray wavelengths of 0.4-1.7 Å are available. Wavelengths of 1.0 Å and below are more commonly used, due to lower harmonic content and optimal flux. The monochromatic X-ray beam is finally incident on to the diffraction instrument as shown schematically in Fig. 4.3.

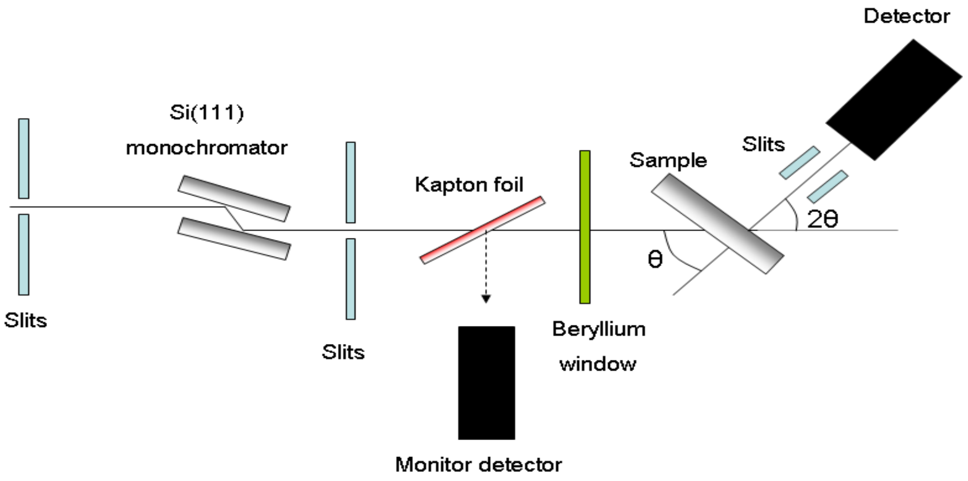

Figure 4.3: Schematic illustration of the layout of an X-ray diffraction experiment

Before the X-ray beam reaches the sample, it first passes through slits as shown in Figure 4.3. This reduces the beam size to the required value. The temperature-controlled Si(111) channel-cut crystal monochromator is used to select the desired wavelength. Next the radiation passes through more apertures and slits to control the size of the beam.

The wavelength used for each experiment is stated in the results sections; for simplicity, here we will use 0.4858 Å, as an example, which is calibrated by using the K-edge of a silver foil. This value is low enough to provide data to a high value of momentum transfer ($\hbar Q$, where $Q_{\max} = 4\pi \sin\theta/\lambda \sim 23$ Å^{-1}; 2θ is the scattering angle, and λ is the wavelength of the diffracted radiation). The effective resolution in real-space can be expressed as, [4.4]

$$\Delta r \sim \frac{2\pi}{Q_{\max}}. \quad (4.35)$$

The diffractometer is a two circle machine with a sample θ axis and a detector 2θ axis. The sample is rotated by an angle of θ and the detector positioned at 2θ to record the scattered X-rays (as shown in Figure 4.3). In all experiments carried out on station 9.1 at the SRS, the 2θ range used was from 1.6-125°, with a step of 0.2°.

More slits are employed between the sample and the detector to define the origin of the scattering reaching the detector. The detectors are NaI scintillation detectors which measure radiation using the photoelectric effect.

Beamline ID15 at the ESRF is an X-ray diffraction station with an energy range of 30 keV to 1000 keV [4.2]. There are two insertion devices on this station. These are devices which are inserted into a straight section of the storage ring, they produce forward directed quasi-monochramatic synchrotron radiation, by deflecting the electrons with a magnetic field. An asymmetrical multipole wiggler (AMPW) serves ID15B with one central "white" beam, and a superconducting wavelength shifter (SCWS) serves ID15A with three separate beams. The diffraction studies presented in the results section were performed using ID15B. A schematic of the actual experimental setup is shown in Figure 4.4.

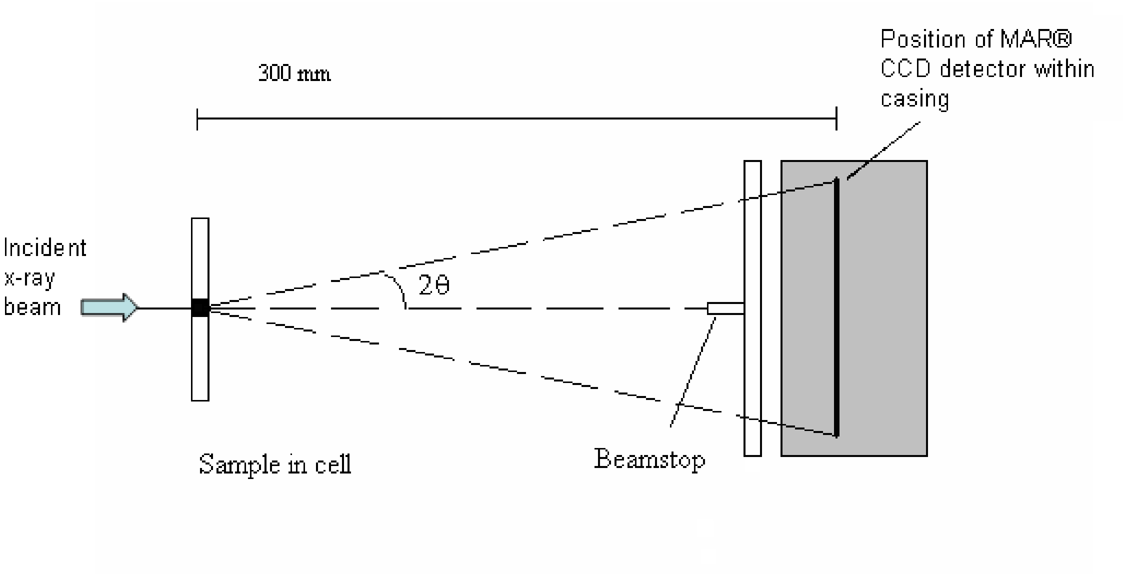

Figure 4.4: Schematic of the experimental setup on station ID15B.

The sample preparation and a full description of the experimental setup will be provided in each results section.

4.4 X-ray diffraction data analysis

The X-ray diffraction data analysis method employed here is based on the methodology of Warren [4.2]. The following is a description of the data analysis necessary for data acquired at station 9.1 at the SRS.

Data reduction was performed using programs written in fortran and then Matlab by past members of the Kent Group, namely D Huxley, DT Bowron and DM Pickup.

A flow chart outlining the programs used during data reduction can be found in Figure 4.5. A full description of each program can be found in Appendix 1. The programs outlined in Appendix 1 are used to manipulate the data to obtain structural information.

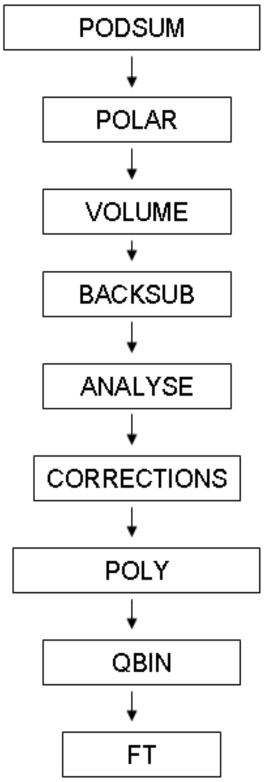

Figure 4.5: Flow chart showing programs used to analyse X-ray diffraction data.

In order to utilise these programs, the composition and density of the samples need to be known. X-ray fluorescence is used to analyse the compositions of the samples and helium pycnometry is used to determine an accurate value of density. These two processes are outlined in more detail in the following chapter.

The program PODSUM normalises the raw data against the monitor count to correct for the beam decay effect. This is necessary because the X-ray flux is not constant during an X-ray experiment as the electron beam current decays with time. The programs POLAR, VOLUME, BACKSUB, ANALYSE and CORRECTIONS perform the removal of background scattering, correction for absorption and inelastic scattering, and subtraction of the self-scattering term. No correction was made to account for multiple scattering since it is a negligible effect in high energy X-ray diffraction from thin samples having low sample attenuation. The programs POLY and QBIN convert the 2θ data into the resultant structure factor, *S(Q)*, which can reveal structural information by Fourier transformation to obtain the differential correlation function *D(r)* (done using the program FT).

To obtain structural information from this differential correlation function, the Q-space data is simulated by the program DORFIT10 using compositions and initial guesses of peak distances and coordination numbers for the partial correlations. The Q-space simulation is generated using the following equation,

$$p(Q)_{ij} = \frac{N_{ij} w_{ij}}{c_j} \frac{\sin QR_{ij}}{QR_{ij}} e^{(\frac{-Q^2 \sigma_{ij}^2}{2})}. \qquad (4.36)$$

where $p(Q)_{ij}$ is the pair function in reciprocal space. N_{ij}, R_{ij} and σ_{ij} are the coordination number, atomic separation and Debye-Waller factor (determines the reduction in intensity of Bragg peaks due to thermal vibrations [4.1]), respectively, for atom i with respect to atom j. c_j is the concentration of atom j and w_{ij} is defined as the weighting factor given by,

$$w_{ij} = \frac{2c_i c_j f_i(Q) f_j(Q)}{[\overline{f(Q)^2}]} \qquad \text{where } i \neq j \qquad (4.37)$$

$$w_{ij} = \frac{c_i c_j f_i(Q) f_j(Q)}{[\overline{f(Q)^2}]} \quad \text{where } i{=}j \qquad (4.38)$$

where $f_i(Q)$ and $f_j(Q)$ are the atomic scattering factors for each atom type defined in section 4.1.2.

The parameters N_{ij}, R_{ij} and σ_{ij} are varied to obtain a simulation in r-space,

$$D(r) = \int_{Q\min}^{Q\max} M(Q) Q p(Q) \sin(Qr) dr + 2\pi^2 r \rho_0 \qquad (4.39)$$

where ρ_0 is the density of the sample, and $M(Q)$ is the optional Hanning window function, applied to reduce FT termination ripples, necessitated by the finite maximum experimentally attainable value of Q. The definition of the Hanning window function can be found in Appendix 1.

Equation 4.39 is the differential correlation function. An example of the fitting can be seen in Figure 4.6 below.

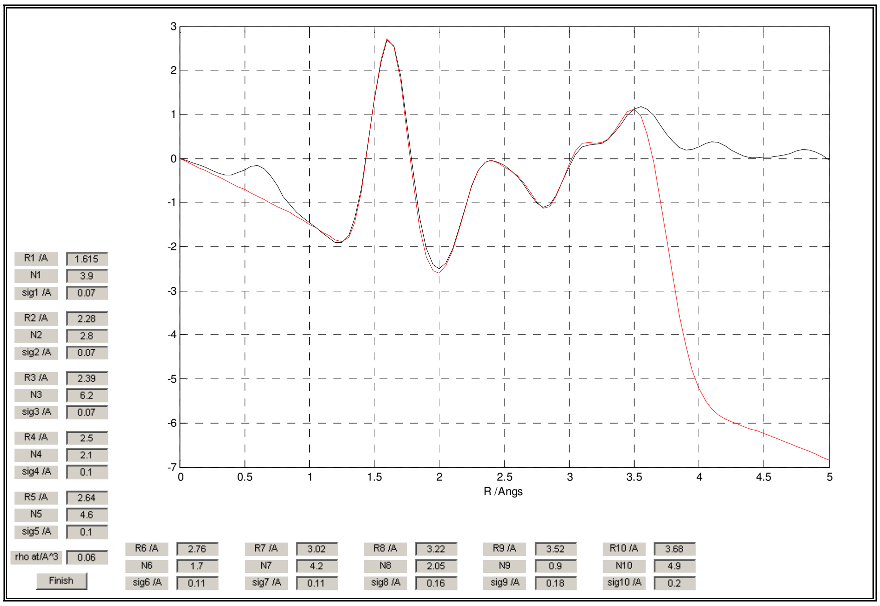

R1 /A 1.615
N1 3.9
sig1 /A 0.07

R2 /A 2.28
N2 2.8
sig2 /A 0.07

R3 /A 2.39
N3 6.2
sig3 /A 0.07

R4 /A 2.5
N4 2.1
sig4 /A 0.1

R5 /A 2.64
N5 4.6
sig5 /A 0.1

rho at/A^3 0.06

R6 /A 2.76
N6 1.7
sig6 /A 0.11

R7 /A 3.02
N7 4.2
sig7 /A 0.11

R8 /A 3.22
N8 2.05
sig8 /A 0.16

R9 /A 3.52
N9 0.9
sig9 /A 0.18

R10 /A 3.68
N10 4.9
sig10 /A 0.2

Figure 4.6: A snapshot of the simulation process from the program DORFIT10.

In Figure 4.6 the black line is the Fourier transform of the *Q*-space data output from the program FT, described in section 8 of Appendix 1. The red line is the simulation of the data produced by the program DORFIT10. The grey boxes contain the values for parameters N_{ij}, R_{ij} and σ_{ij} which are varied to produce an acceptable simulation.

Throughout this thesis the total correlation function *T(r)* is used to visualise the data. The program DOR2TOR will convert the differential correlation function to the total correlation function using:

$$T(r) = D(r) + 2\pi^2 \rho_0 r \quad (4.40).$$

Analysis for samples examined on station ID15B at the ESRF is slightly different to the method described above. The X-ray scattering patterns were recorded using a CCD-based MAR® 345 image plate detector. The two dimensional images, an example of which is shown in Figure 4.7, were radially integrated about the centre of the image. The centre of the image and the tilt of the detector were found and corrected for using software written in Matlab by Dr Veijo Honkimaki, station scientist of ID15, ESRF.

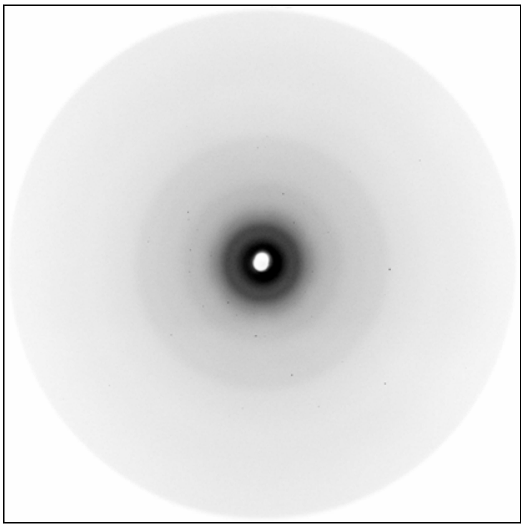

Figure 4.7: Graphical output file from the Mar345 detector on station ID15B at the ESRF.

The data is corrected for the beam decay (as in the program PODSUM mentioned above) then trimmed to 1000 of the 1150 points which removes the ill-determined effects associated with pixels at large angles (at the edge of the detector) and any problems with the straight through beam and the beam stop. Corrections are made for absorption due to the sample, as well as for the absorption in air. The background associated with the scattering caused by the X-rays travelling through the air is also calculated and subtracted. The recorded scattering pattern for an "empty cell" (i.e. the empty sample holder) is also subtracted at this stage.

A program is now used to sum any repeat data sets together, and convert the data to Q-space. The programs found in sections 4, 5, 6 and 8 of Appendix 1 are then used to obtain the differential correlation function $D(r)$, and then converted to $T(r)$ using equation 4.40 above.

4.5 Neutron Diffraction Theory

4.5.1 Introduction

Neutron scattering is another experimental method to realise the distribution functions mentioned in section 4.1. Neutrons are uncharged constituents of atoms and therefore penetrate materials well. Unlike X-rays, which interact with electrons surrounding atoms, neutrons interact with the nucleus of atoms. The statistical accumulation of diffracted neutrons beyond the sample can be used to obtain structural information.

Neutron diffraction can be divided into two types, elastic and inelastic scattering as described in section 4.2.1.

The de Broglie wavelength, λ, describes a neutron travelling at velocity v_n with energy E_n, where k is the magnitude of the wavevector and m_n the mass of the neutron.

$$m_n v_n = h / \lambda \quad (4.41)$$

$$E_n = \frac{h^2}{2m_n\lambda^2} = \frac{\hbar^2 k^2}{2m_n} \quad (4.42)$$

The interference that occurs when λ is similar to the inter-atomic spacing in a sample can be analysed to give structural information on the material being studied. In the next section, neutron diffraction theory is outlined.

4.5.2 Neutron diffraction theory

An outline of neutron diffraction theory can be found in the books by Squires or Newport, Rainford and Cywinski [4.6, 4.7]. There are many similarities between neutron and X-ray scattering, and hence a full description of neutron diffraction will not be given. The formulae in the sections 4.2.2, 4.2.3 and 4.2.4 can be used; however, the atomic scattering factor $f_a(Q)$ is replaced by the appropriate quantity representing neutron scattering by the nucleus, which is the scattering length b. This is related to the bound-atom cross section, σ_s, by

$$\sigma_s = 4\pi b^2 \qquad (4.43)$$

So for scattering from a material with different types of atoms, we can write the partial structure factor $S_{ij}(Q)$ as

$$S_{ij}(Q) = 1 + \rho_0 \int (g_{ij}(r) - 1) e^{(iQ \cdot r_{ij})} dr \qquad (4.44)$$

The total pair distribution function, $g_T(r)$, can also be interpreted for neutron scattering as

$$g_T(r) - 1 = \sum_{i=1}^{T} \sum_{j=1}^{T} c_i c_j b_i b_j (g_{ij}(r) - 1) \qquad (4.45).$$

4.6 Neutron Diffraction Experimental Setup

The neutron diffraction experiments were carried out on the general materials diffractometer (GEM) at ISIS pulsed neutron and muon source. GEM is used to study the structure of disordered materials because it is on a high intensity neutron source and achieves high count rate due to the high solid angle of its high efficiency scintillator detectors and the accessible Q-range is such that high real-space resolution is achievable. A detailed description of GEM can be found in [4.8]. A beam of neutrons is produced when the 160 kW, 800 MeV proton beam from the accelerator hits a metal target and releases neutrons via a spallation process. Moderators are used to slow down fast neutrons to enable a more useful range of wavelengths to be obtained. The detectors cover a wide range of scattering angle and a large solid angle, as can be seen in Figure 4.8.

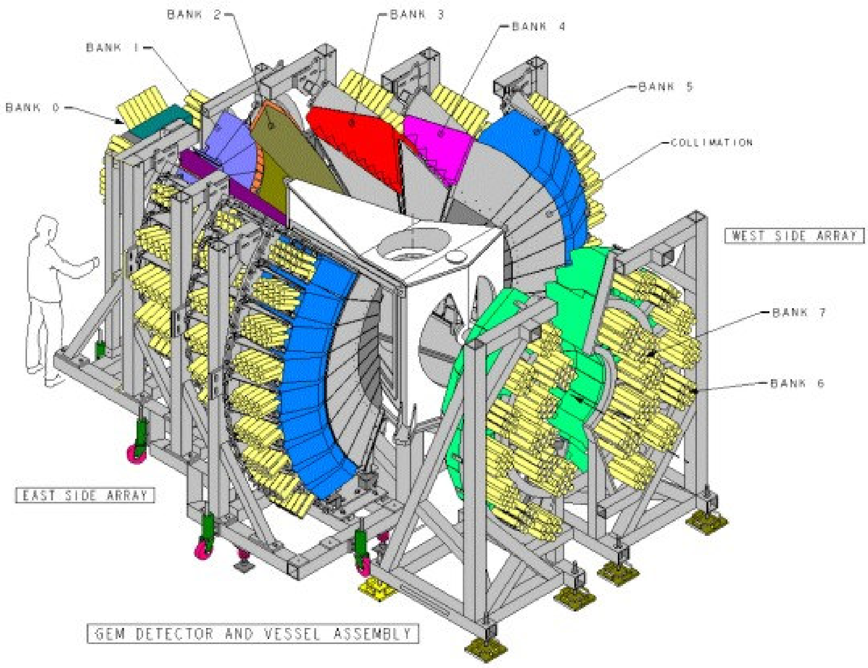

Figure 4.8: Schematic diagram of GEM from the ISIS website. (www.isis.rl.ac.uk)

The GEM detectors are zinc sulphide scintillators. GEM has choppers for setting the wavelength range and a chopper to reduce the contribution to the background by high energy neutrons. The beam that arrives on GEM has a maximum size of 40mm by 20mm which can be adjusted using apertures (GEM employs five motorised beam-defining apertures, and one beam-scraper nearest the sample, to ensure the required beam size).

4.7 Neutron Diffraction Data analysis

The description of programs used in neutron diffraction data analysis is outlined in Appendix 2. A further more detailed description of the theoretical basis to the software can be found in a report by Soper *et al.* [4.9].

The initial stages of analysis of neutron diffraction data from an amorphous material entails the removal of background scattering, correction for absorption and multiple scattering, and subtraction of the self scattering terms. The programs used for this analysis are outlined in Appendix 2, sections 2, 3 and 4. A flow chart of the programs used in neutron diffraction analysis is shown in Figure 4.9.

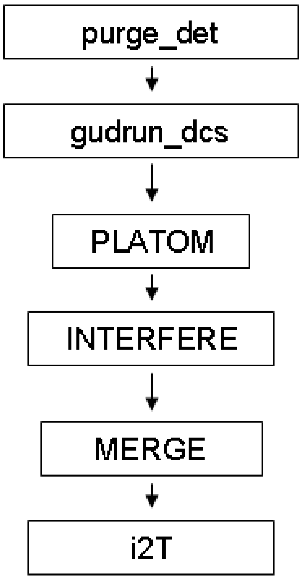

Figure 4.9: Flow chart of programs used to analyse neutron diffraction data.

The program *purge_det* identifies problems with any of the detectors, and removes them from the analysis. The program *gudrun_dcs* sums the runs of each type and converts to a Q-scale after correcting for absorption and multiple scattering. The spectra are normalised to an absolute scale using the scattering profile from a cylindrical sample of vanadium.

The resultant scattered intensity, *S(Q)* can reveal structural information when Fourier transformed, as in Appendix 2, section 6.

A *Q*-space simulation of the structure factor is generated using equation 4.36 as shown in section 4.4. Again $p(Q)_{i\,j}$ is the pair function in reciprocal space (i.e. derived from the real-space model by Fourier transformation); $N_{i,j}$, $R_{i,j}$ and $\sigma_{i,j}$ are the coordination number, atomic separation and disorder parameter (described in section 4.4) respectively of atom *i* with respect to atom *j* ; c_j is the concentration of atom *j* , and $\omega_{i,j}$ is a weighting factor calculated from the relevant concentration and neutron scattering length data.

The program employed for the simulation is called *Tor_fit*. Here we simulate the total correlation function *T(r)*, and the weighting factors corresponding to neutron data are as follows:

$w_{ij} = 2c_i c_j b_i b_j$ where $i \neq j$ (4.46)

$w_{ij} = c_i c_j b_i b_j$ where $i=j$. (4.47)

4.8 Reverse Monte Carlo Modelling

4.8.1 Introduction

Reverse Monte Carlo (RMC) modelling is a useful tool when investigating the structure of disordered materials. RMC modelling is a method for producing three-dimensional models of the structure of disordered materials that quantitatively agree with available diffraction (and other) data. No interatomic potential is required for RMC modelling, unlike Molecular Dynamics and Monte Carlo modelling, and RMC modelling can utilise data from different sources (e.g. neutrons, X-rays, extended X-ray absorption fine structure (EXAFS) and solid state NMR). The structural model is actually fitted to the data, which ensures good agreement. A detailed description of reverse Monte Carlo modelling can be found in the RMC manual, [4.10], or in a paper by *McGreevy.* [4.11] RMC modelling has shown to be useful when modelling the structure of disordered materials, and especially useful when combined with both X-ray and neutron diffraction data. [4.12, 4.13]

4.8.2 RMC Theory

RMC is a variation of the standard Metropolis Monte Carlo procedure. In RMC we start by assuming that the experimentally measured structure factor, $S^E(Q_i)$, contains only statistical errors that have a normal distribution. The difference between the calculated structure factor, $S^C(Q_i)$, which is calculated from a model of the real structure, and that measured experimentally can be defined as

$$e_i = S^C(Q_i) - S^E(Q_i) \qquad (4.48)$$

and has a probability

$$p(e_i) = \frac{1}{\sqrt{2\pi}\sigma(Q_i)} e^{-\frac{e_i^2}{2\sigma(Q_i)^2}} \qquad (4.49)$$

where $\sigma(Q_i)$ is the standard deviation of the normal distribution of statistical errors.

The total probability of the calculated structure factor is

$$P = \prod_{i=1}^{m} p(e_i) = \left(\frac{1}{\sqrt{2\pi}\bar{\sigma}}\right)^m \exp\left(-\sum_{i=1}^{m} \frac{e_i^2}{2\sigma(Q_i)^2}\right) \qquad (4.50)$$

where m is the number of Q_i points in S^E and

$$\bar{\sigma} = \left(\prod_{i=1}^{m} \sigma(Q_i)\right)^{1/m} \qquad (4.51)$$

We need to create a statistical ensemble of atoms whose structure factor satisfies the above probability distribution, in order to model the structure of a system using S^E. Writing the exponent as follows,

$$\chi^2 = \frac{\sum_{i=1}^{m} (S^C(Q_i) - S^E(Q_i))^2}{\sigma(Q_i)^2} \qquad (4.52)$$

then we can see $P \; \alpha \; exp(-\chi^2/2)$.

We can now define the RMC algorithm.

The first thing is to start with an initial configuration of atoms with periodic boundary conditions. The initial configuration is made up of N atoms, whose positions are decided using any prior chemical knowledge. An explanation of building the initial configuration is outlined in the next section.

We now calculate the radial distribution function for this 'old' configuration,

$$J_0^C(r) = 4\pi r^2 g(r) \qquad (4.53)$$

as defined in section 4.1. The configuration size, L, should be sufficiently large so that there are no correlations across the shell, i.e. $J(r > L/2) = 1$.

The radial distribution function $J(r)$ is only calculated for $r < L/2$ and the nearest image convention is used to determine the atomic separations. We now transform to the total structure factor

$$S_0^2(Q) - 1 = \frac{4\pi\rho}{Q}\int_0^\infty r(J_0^C(r) - 1)\sin Qr dr \qquad (4.54)$$

where $\hbar Q$ is the momentum transfer.

The difference is then calculated between the measured total structure factor and that determined from the configuration

$$\chi_0^2 = \sum_i (S_0^C(Q_i) - S^E(Q_i))^2 / \sigma(Q_i)^2 \qquad (4.55)$$

Here the sum is over the m experimental points and $\sigma(Q_i)$ is the experimental error. One atom is moved at random and the new radial distribution function, $g_n^C(r)$, and total structure factor, $S_n^C(Q)$ are calculated which gives us the new difference

$$\chi_n^2 = \sum_i (S_n^C(Q_i) - S^E(Q_i))^2 / \sigma(Q_i)^2 \qquad (4.56)$$

If $\chi_n^2 < \chi_o^2$ then the move will be accepted and the new configuration becomes the old configuration. If $\chi_n^2 > \chi_o^2$ then the move is accepted with a probability of $\exp((\chi_n^2 - \chi_o^2)/2)$. Otherwise the move is rejected. This process is repeated and χ^2 will initially decrease, and then reach an equilibrium value about which it will oscillate. The resulting configuration will be a three dimensional structure that is consistent with the experimental total structure factor, within the experimental error.

The algorithm described above is modelling a single set of data. However RMC provides the option to model several sets of diffraction data, using either the structure factor or the radial distribution function as the fit-function.

For a multicomponent system where the fit is to several different total structure factors (indicated by index k),

$$\chi^2 = \sum_k \chi_k^2 = \sum_k \sum_{i=1}^{m} (S_k^C(Q_i) - S_k^E(Q_i))^2 / \sigma_k(Q_i)^2 \qquad (4.57)$$

For neutron diffraction

$$S_k^E(Q_i) = \sum_a \sum_b c_a c_b b_{ak} b_{bk} (S_{ab}(Q_i) - 1) \qquad (4.58)$$

where c_a and c_b are the concentrations in sample k and b_{ak} and b_{bk} are the coherent scattering lengths.

For X-ray diffraction

$$S_k^E(Q_i) = \sum_{ab} c_a c_b f_{ak}^*(Q_i) f_{bk}^*(Q_i)(S_{ab}(Q_i) - 1) \qquad (4.59)$$

where $f_{ak}^*(Q_i)$ are the Q dependent form factors for the X-rays of wavelength λ_k.

For the fitting of data sets obtained by different experimental techniques, the separate χ^2 values are simply summed to give one value.

4.8.3 Making the initial configuration

The initial configuration could be a random configuration of N atoms, but usually some prior chemical knowledge of the sample is available. Hence the initial configuration need not be totally random. This information can be used in the form of constraints. The most commonly used constraint is on the closest approach of two atoms. Because of systematic errors in the experimental data, and often because of limited data range, the data would not forbid some atoms from becoming very close together in the model. We know that this is physically implausible, and a constraint can define an appropriate excluded volume. Realistic values for the closest approach of two atoms can be found from the direct Fourier transform of the experimentally derived total structure factors. If a satisfactory value is not chosen, it is obvious in the partial $g(r)$ output from the RMC algorithm in the form of sharp spikes. This constraint is very powerful when combined with a fixed density. Packing is the dominant effect in defining the structure of many materials, and to include information on atomic sizes (minimum effective distances taking into account empirical peaks widths, not tabulated ionic radii) severely limits the number of structures consistent with the data. A constraint on the coordination of atoms can also be employed (e.g. in light of prior chemical knowledge, solid state NMR data, etc.). A coordination number of n_{ab} is defined as being the number of atoms of type b between two fixed distances of one atom of type a. The minimum distance is usually the distance of closest approach mentioned above. Coordination constraints are weighted using the parameter σ_c, which weights the constraint relative to the data. If $\sigma_c \approx 0$ then it is effectively impossible for atoms with the constrained coordination to change it.

To summarise, when producing the starting model, an initial configuration of N atoms is produced, with the correct concentration of each atom type, and the correct number density. This configuration is then constrained, using closest approach distances and coordination constraints. This model can now be used as the starting configuration when fitting to the data. In Appendix 3, a brief description of RMC programs used to make initial configurations of atoms can be found.

4.8.4. Fitting to the data

When a satisfactory initial model has been produced, it may then be fitted to the data. As mentioned earlier, several data sets of different diffraction experiments can be fitted: e.g. neutron diffraction data, extended X-ray absorption fine structure data, and X-ray diffraction data. In the RMC data file, we can input how many data sets of each type there are. The first type is *G(r)* data sets. The *G(r)* is the total pair distribution function, and is the direct Fourier Transform of the total structure factor. The second type is the total structure factor *S(Q)*. The next type is *F(Q)*, which is also the total structure factor. For the purposes of the RMC program, the difference between *S(Q)* and *F(Q)* here is that the former has constant coefficients of partial structure factors, whereas the latter has *Q*-dependent coefficients, as is the case with X-ray data. The fourth type is the EXAFS data sets. In this thesis, only neutron and X-ray data have been examined, so no further explanation will be given on the use of EXAFS data sets.

The *S(Q)* and the *F(Q)* can be directly input from the data. The *G(r)* is normally obtained using a program called MCGR, the output of which can be used directly as input into RMC. MCGR is a program which determines total or partial radial distribution functions from one or more total structure factors. MCGR uses an inverse method [4.14], which has considerable advantages over conventional direct methods (i.e. Fourier transformation), as it avoids the effects of truncation errors, caused by the finite maximum experimentally attainable value of *Q*, and allows the estimation of errors in the radial distribution functions. A full description of RMC methods, and all the programs associated with RMC can be found on the RMC website. [4.15]

4.9 Grazing Incidence X-ray diffraction method

4.9.1 Introduction

X-rays have a number of advantages: multiple scattering can often be neglected in the cases of samples with small optical path (unlike, say, electrons), and high energy X-rays penetrate significant distances allowing them to obtain microscopic structural information averaged over a large ensemble of atoms or molecules. This distinguishes X-ray techniques from imaging techniques such as the various scanning microscopes, which give real-space images but are limited to surfaces and interfaces, and where one cannot have both a very high resolution and view a large, statistically significant, area at the same time.

X-rays are not intrinsically a surface-selective probe. However, very intense sources of X-rays are now available, and it is sometimes possible to obtain surface information simply by looking for deviations from the ideal bulk scattering, and attributing these deviations to the surface.

4.9.2 Theory

Waves can propagate into regions where their propagation is classically forbidden, as has been demonstrated by phenomena ranging from frustrated total internal reflection to particle tunnelling. In the conventional plane wave representation these effects are described by evanescent waves, i.e. waves whose wave vector consists of real and imaginary components. When the index of refraction of materials is generally less than unity, such as at X-ray energies, the phenomenon is manifested as total external reflection, with wave solutions decaying exponentially into the surface of the medium. The short decay length of evanescent X-rays makes them attractive as a surface probe. It has been natural to combine the surface enhancement of grazing incidence X-rays with diffraction to obtain the ordering of surface layers, giving grazing incidence X-ray diffraction. Materials with a refractive index less than one, can therefore have total external reflection from a surface if the incident angle is small enough (typically 0.05–1.5º, depending on the substrate electron density and the X-ray energy). At this point the substrate is not entirely invisible to X-rays, but only an evanescent wave penetrates into and scatters from it. The X-ray intensity is therefore highest at the surface, as desired. It is possible to increase the surface selectivity further by reducing the incident angle and thus causing the evanescent wave to damp out faster.

If the incident beam is coming in at less than the critical angle for total reflection, the specular beam does not carry useful information. However, if there is any lateral order at the surface (or in a monolayer at the surface) there will be diffraction peaks.

4.9.3 Experimental setup

A schematic of the GIXRD geometry is shown in Figure 4.10.

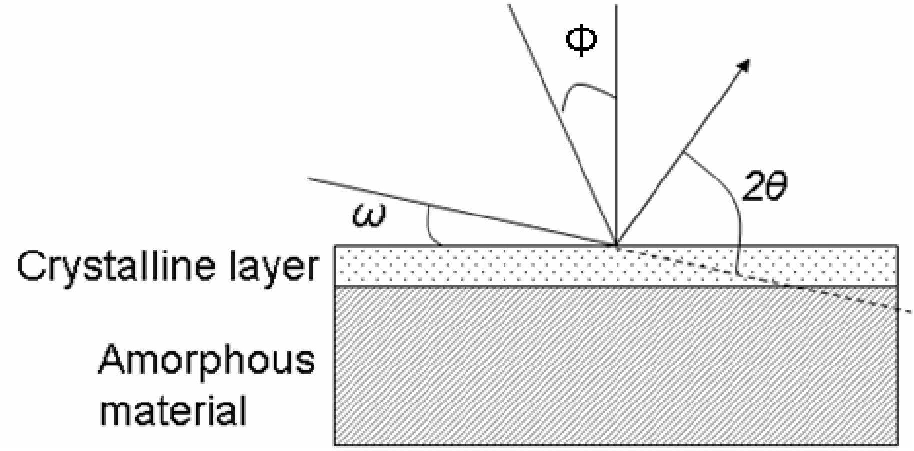

Figure 4.10: Diagram of GIXRD geometry.

The angle *ω* is the angle of incidence of the X-ray beam. *2θ* is the angle of the diffracted beam, and *Φ* is the angle between the surface normal of the sample and the incident and diffracted beam bisector. The sample is set at a fixed small angle, *ω*, to the incident X-rays. An iterative procedure of height and angle adjustment is used to define the zero-angle for the sample. This is important, as the angles used in data collection are so small, the samples must also be as smooth and flat as possible as any irregularity will produce an uncertainty in *ω* and hence in the collected data [4.16]. The samples studied in this thesis were dry-polished using polishing plates of 68, 36 and 12 microns, and then polished using diamond grit down to 0.5 microns. After each stage, the sample was examined under the microscope before proceeding to the next step. This process ensured an optically flat surface suitable for X-ray diffraction at shallow angles of incidence.

The GIXRD data were taken using a Philips *X'Pert* diffractometer with a wavelength derived from the Cu Kα line (1.5405 Å). The goniometer is a four-axis system with 2θ, ω, Φ and Ψ as the variables. ω is the angle between the incident beam and the sample surface. It can be varied independently of 2θ, which is the angle between the incident beam and the diffracted beam. Φ is the rotation angle about the sample normal and Ψ is the tilt angle about a horizontal and centred line in the sample surface. The X-ray beam passes through a 1/8° divergence slit, before reaching the sample. With the sample aligned correctly, the diffraction patterns obtained are biased towards the surface of the samples, although with some bulk scattering contributing an underlying diffraction pattern.

4.9.4 GIXRD Data analysis

As the depth of penetration of the X-rays is not known, and neither are the details of density and composition in the near-surface regions, quantitative analysis of these results cannot be performed. However, a reliable interpretation of a growing crystalline phase on the surface of an amorphous substrate can nevertheless be achieved.

4.10 Small Angle X-ray Scattering

4.10.1 Introduction

Small angle X-ray scattering is a non-destructive method for examining structure in the size range ~10 to a few hundred Ångstroms. X-rays monochromated by an arrangement of optics (described in section 4.11) are incident on the sample and scattered to a range of angles. Variations in the incident beam intensity, and the transmittance of the sample, are monitored using ionisation chambers. The scattered radiation travels down an evacuated camera and is incident on a position sensitive detector at a distance l from the sample; a beam stop is used to absorb the straight-through beam which would otherwise damage the detector. The length of the camera (typically between 1 and 4 metres) determines the range of scattering angles subtended by the detector; this can be chosen to span a range appropriate for the scattering distribution examined. Standard data reduction, involving transmission correction and removal of the background scattering is carried out before detailed data analysis. In the case of shorter camera lengths, a correction to take account of slit smearing must be considered (however, this is not applicable in the experiments reported in this thesis).

4.10.2 Scattering from individual particles

The focusing of a beam of coherent X-rays on a sample causes the electrons in the sample to resonate with the frequency of the incident radiation, and emit coherent secondary (scattered) waves whose intensities are given by the well known Thompson formula:

$$I_e(\theta) = I_p \cdot (7.90 \cdot 10^{-26}) \cdot \frac{1}{a^2} \cdot \frac{1+\cos^2 2\theta}{2} \qquad (4.60)$$

where I_p the primary intensity, $7.90*10^{-26}$ is the classical electron radius, a is the distance of object to point of registration, and 2θ is the scattering angle.

The radiation detectors employed in SAXS experiments do not measure the amplitude of the radiation, as they are not sensitive to the phase of the incident waves. Instead it is the power flux which is measured which is defined as the squared amplitude of the scattered wave.

The Thompson equation illustrates the dependence of the emitted intensity on a, the distance from the scattering entity to the point of detection, and the fact that scattered intensity is only slightly dependent on the angle at which the wave is scattered, through the polarisation factor. However, across the angular range probed by SAXS, this factor can be assumed to be unity.

As the scattered waves are coherent, their amplitudes can be added, and the intensity is given by the square of the resultant amplitude. The scattered amplitudes are of equal magnitude and therefore it is only the difference in phase, ψ (which is defined as $2\pi/\lambda$ times the path difference between the optical path and an arbitrary reference point), which determines the intensity detected at a particular angle. There is a relationship between the sizes of the scattering entities and the angles at which the phase difference causes constructive interference, and thus a peak in intensity.

Taking r as the distance between entities, as the magnitude of r increases, the angle resulting in a path difference of 1λ reduces, thus any constructive interference shifts to smaller and smaller angles. If each scattered wave is represented using Euler's complex form,

$$\psi = Ae^{i\psi} \qquad (4.61)$$

an expression for ψ can then be derived as follows:

If the direction of an incident beam of X-rays is denoted by the unit vector ***k***, and that of the scattered beam by the unit vector ***s***, the path difference of a point *P* specified by the vector ***r*** against the origin *O* is then

$$- \ (\ - \ ) \qquad (4.62)$$

Therefore the phase difference is

$$\psi = -(\frac{2\pi}{\lambda}\boldsymbol{r})\boldsymbol{s}(\ \boldsymbol{k} - \ ) \qquad (4.63)$$

Noting that (***s*** - ***k***) lies symmetrically with respect to the incident and scattered beam, and that its magnitude is *2sinθ*, where *θ* is half the glancing angle as used in crystallography. Thus the vector ***Q*** normal to ***s***, has the same direction, and its magnitude is given by

$$|Q| = \frac{4\pi}{\lambda}\sin\theta \qquad (4.64)$$

Therefore the phase takes the form of the vector product,

$$\psi = \quad \cdot \qquad (4.65)$$

meaning it is the only component of ***r*** in ***Q*** which contributes to the phase. Thus each scattered wave can be represented by a term

$$\psi = A_0 e^{\boldsymbol{Qr}} \qquad (4.66)$$

and the total scattered amplitude is given by the form factor *F(**Q**)* which is simply the sum of the individual waves.

The measured intensity is the square of this amplitude per unit volume,

$$I(\mathbf{Q}) = \frac{1}{V}[|F^{*}(\mathbf{Q})F(\mathbf{Q})|] \qquad (4.67)$$

When defining the form factor it is more convenient to use the electron density of the sample *ρ(**r**)* – defined as the number of electrons per unit volume – rather than the sum of the contribution from each electron. If the irradiated volume is divided into infinitesimal elements, d*V*, then the number of electrons in each volume element is *ρ(**r**)*d*V*. Thus the total scattered amplitude can now be expressed as an integral over volume of the amplitude from each infinitesimal region of electron density,

$$F(\mathbf{Q}) = \int \rho(\mathbf{r}) e^{i\mathbf{Q}\cdot\mathbf{r}}\, dV \quad (A_0=1) \qquad (4.68)$$

This integral has the form of a Fourier transform, and if the particle in question has a homogeneous electron density distribution, the total scattered amplitude is the spatial Fourier transform of the electron density.

4.10.3 The Guinier Approximation

For particles embedded in a medium (solvent) which has intrinsic electron density *ρ(r)* > 0, it is the fluctuation in electron density between the sample and the solvent, called the scattering contrast, which is responsible for the observable scattering pattern. If the sample and the solvent are of identical electron density, then correlations will exist on all length scales for every orientation, and no information about the structure of the particles would be available. Representing this contrast by $\Delta\rho$, for the central part of symmetric particles we can write the form factor as,

$$F(Q) = (\Delta\rho)\int \cos QrdV , \qquad (4.69)$$

Expanding the term cos Qr into its power series, representing Qr in cartesian coordinates and neglecting the higher order terms, this can be simplified to, [4.17, 4.18]

$$I(Q) = (\Delta\rho)^2 V e^{\frac{-Q^2R^2}{3}} \qquad (4.70)$$

The parameter R is the radius of gyration, defined as the mean square distance from the centre of gravity, where the role of “mass” is played by the electrons. It is in essence the moment of inertia for the particle using the electron density rather than the mass as a weighting factor. This result was first given by Guinier in 1939 [4.19] and provides a simple method for the calculation of the average particle size. From the $I(Q)$ vs Q data, this last equation manifests as Guinier regions of exponential decay in the intensity as a function of Q. Despite the approximations used, the equation is applicable to all but the most anisotropic of scattering systems, and as such is relied upon heavily. The radius of gyration equation must only be used with materials which satisfy the conditions for which the approximation is valid: 1) the material must be an isotropic system, 2) $(Q^2R^2)/3<1$, 3) the scatterers in the material must scatter independently; that is the scattered intensity from n scatterers must be n times the scattering from a single scatterer. [4.20]

4.10.4 The Correlation Function

Whilst the approximation for *F(Q)* given in polar coordinates is valid for ideal scatterers, in practice the assumptions of homogeneous electron density and spherical symmetry are usually invalid. Therefore to describe the scattering of a system as a function of angle, we need a description of the spatial arrangement of the electrons within the sample. The scattered intensity is given in an equation as the square of the form factor, which in practise is performed using its complex conjugate *F**, giving the fourier integral,

$$I(Q) = FF^* = \int\int \rho(r_1)\rho(r_2)e^{[-iQ(r_1-r_2)]}dV_1 dV_2 \qquad (4.71)$$

This integral is best determined in two steps, the first being the density auto-correlation integral, which gives the Patterson function of crystallography, [4.17]

$$\rho^2 \equiv \int \rho(r_1)\rho(r_2)dV_1 \qquad (4.72)$$

The second step is the volume integral of the scattered waves produced by this squared density,

$$I(Q) = \int \rho^2(r)e^{-iQr}dV \qquad (4.73)$$

The scattered intensity *I(Q)* can also be derived by substituting $\rho^2(r)$ for $\rho(r)$ in *F(Q)* giving,

$$I(Q) = \int 4\pi r^2 \rho^2 (\frac{\sin Qr}{Qr})dV \qquad (4.74)$$

Extending the idea of fluctuating electron density in the sample being responsible for the scattering curve,

$$\rho^2 - V\rho^2 = V\gamma(r) \qquad (4.75)$$

$$I(Q) = V\int 4\pi r^2 \gamma(r)(\frac{\sin Qr}{Qr})dr \qquad (4.76)$$

The term $\gamma(r)$ is the correlation function of Debye and Bueche [4.21], which describes the probability of finding two regions of identical electron density separated by a distance r. If the electron density difference $(\Delta\rho)$ is assumed to be constant $\gamma(r)$ can be written as,

$$\gamma(r) = (\Delta\rho)^2 \gamma_0(r) \qquad (4.77)$$

where $\gamma_0(r)$ depends solely on the geometry of the object, and is equal to unity at the origin, and zero at distances greater than the maximum particle diameter. Substituting this into $I(Q)$ gives,

$$I(Q) = (\Delta\rho)^2 V\int 4\pi r^2 \gamma_0(r)(\frac{\sin Qr}{Qr}) \qquad (4.78)$$

This equation provides a general form of the scattered intensity of an object as a function of the distance correlations present.

4.10.5 Porod’s Law

An interesting phenomenon appears at higher Q values for samples with a very sharp interface (for example very flat surfaces). A power law decay is observed in the intensity versus Q data, in the form of a Q^{-4} dependence. This region of higher Q data is known as the Porod region [4.18] and Porod’s law can be used to measure the surface area of domains in the nano-scale.

A derivation for $\gamma_0(r)$ can be approximated by considering the volumes of the particle, and its correlation ‘ghost’ [4.17] as differing only by a shift of the surface of one particle with respect to the other. The contribution of a surface element is then $dS.\boldsymbol{r}\cos\theta$ if we define the angle between $\boldsymbol{r}$ and the surface normal $\boldsymbol{n}$ as θ [4.17]. However only the scalar products for which $\boldsymbol{n}.\boldsymbol{r} < 0$ are considered; that is, $\cos\theta < 0$. This corresponds to performing the integration for the Fourier integral of $I(Q)$ – which for each magnitude of r is performed twice, for the directions $+r$ and $-r$ – for only one direction of r, that which corresponds to the vector directed from the surfaced of the particle towards the centre. Averaging over $\cos\theta$ introduces a factor of ½, while the consideration of the contributions from the inwardly directed vectors only gives another factor of ½. After expanding $\gamma_0(r)$ into its corresponding power series, this produces the approximate form of $\gamma_0(r)$,

$$\gamma_0(r) = 1 - \frac{S}{4V} \quad (4.79)$$

where S is the particle surface area. Substituting this into $I(Q)$ and integrating by parts gives a series of negative powers of Q, the most important of which (for these length scales) gives the scattered intensity as,

$$I(Q) = (\Delta\rho)^2 (\frac{2\pi}{Q^4}) S \qquad (4.80)$$

This power law derived independently by Porod and Debye *et al.* [4.22, 4.23] is valid not only for single particles, but also for densely packed systems and for non-particulate structures provided there exists a well defined internal surface [4.17].

4.11 Small angle X-ray scattering experimental method

The small angle X-ray scattering measurements were performed on station 6.2 at the SRS, Daresbury Laboratory, UK. Station 6.2 is a materials science station dedicated to the study of time-resolved variation of short and/or long-range order in a variety of inorganic and organic materials. The beamline can be used for two main purposes: time-resolved, medium resolution X-ray Powder Diffraction (often referred to as Wide-Angle X-ray Scattering, WAXS, in this context) and time-resolved Small-Angle X-ray Scattering, SAXS. All the experiments presented in this study were undertaken using both the small angle and wide angle detectors simultaneously. The X-ray source is a Mutli-Pole Wiggler (MPW) insertion device and the energy used can be selected within the range 5 keV to 18 keV. The standard energy delivered by the station is 8.865 keV (λ = 1.40 Å), which is what was used for all the work presented in this thesis. At this energy the output from the insertion device and the detectors' efficiencies are optimised. The intense X-ray source is complemented by a 2-dimensional SAXS detector and 1-dimensional WAXS detector.

The WAXS detector is mounted rigidly onto a nose cone sited adjacent to the sample position and in this position it has an acceptance angle of 7 degrees to 67 degrees in 2θ in the upwards vertical plane. Beyond the nose cone a variable-length evacuated small-angle X-ray scattering (SAXS) camera tube is fitted, with stepwise length variations between ~1.3 and ~4.00 metres possible, in 0.25 metre steps. At the end of the SAXS tube a 2-dimensional small-angle detector is placed which is aligned to be effective in the downward vertical plane (shown in Figure 4.11).

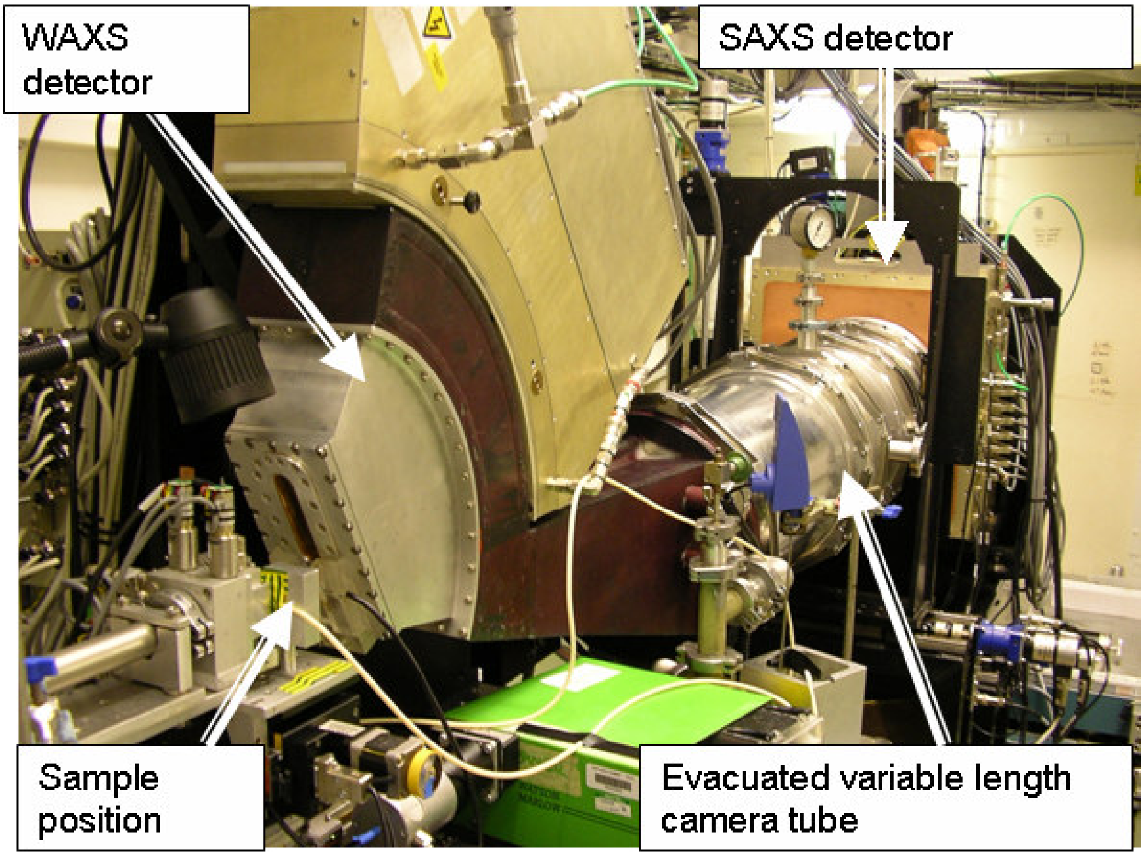

Figure 4.11: Photograph of the SAXS/WAXS camera setup

The SAXS detector utilises a standard aperture design of a 60 degree quadrant and is functionally complementary to the curved WAXS detector enabling truly synchronised SAXS and WAXS measurements to be made.

4.12. Small Angle X-ray Data Analysis

The initial stages of data analysis were performed using the program OTOKO. Details of this program can be found on the SRS, Daresbury Laboratory website [4.24]. The data is first normalised in order to correct for variations in incident beam flux. At this stage, any multiple scans are averaged together. Any relevant background (empty sample holder) is then removed to produce the raw data files. In order to convert the x-axis to Q space, the SAXS data was calibrated using a reference of wet rat tail collagen, a scan of which was taken at the beginning of each experiment [4.24], and the WAXS data was calibrated using a reference of silicon powder [4.25]. Further data analysis is explained in the relevant results chapters.

References

[4.1] Cusack, N.E. *The Physics of Structurally Disordered Matter,* IOP Publishing Ltd, Bristol, 1987.

[4.2] Warren, B.E. *X-ray diffraction,* Dover Publications, New York, 1990.

[4.3] www.srs.ac.uk/srs/stations/station9.1.html

[4.4] Windsor, C.G. *Pulsed Neutron Scattering*, Taylor &Francis Ltd, London, 1981.

[4.5]http://www.esrf.eu/UsersAndScience/Experiments/MaterialsScience/ID15/3axes/3axintro.html

[4.6] Squires, G.L. *Introduction to the theory of thermal neutron scattering*, Dover Publications Inc, New York, 1996.

[4.7] Newport, R.J., Rainford, B.D., Cywinski, R., Eds., *Neutron Scattering at a Pulsed Source*. Adam Hilger, Bristol. 1988.

[4.8] Hannon, A.C., *Nuclear Instruments and methods in Phys. Res A*, **551**, 2005, 88-107.

[4.9] Soper, A.K., Howells, W.S., Hannon, A.C. *ATLAS - Analysis of Time-of-Flight Diffraction Data from Liquid and Amorphous Samples*', Rutherford Appleton Laboratory Report RAL-89-046, 1989.

[4.10] www.isis.rl.ac.uk/rmc/downloads/rmca/rmca_3_14.pdf

[4.11] McGreevy, R.L. *J. Phys.: Condens. Matter.,* **13,** 887, 2001.
[4.12] Keen, D.A., McGreevy, R.L., *Nature*, **344**, 423-425, 1990.

[4.13] McGreevy, R.L., Howe, M.A., *Annu. Rev. Mater. Sci.,* **22**, 217-242, 1992.

[4.14] Pusztai, L., McGreevy, R.L., *J. Neutron Res.,* **8**(1), 17-35, 1999.

[4.15] www.isis.rl.ac.uk/rmc

[4.16] Rigden, J.S., Newport, R.J., Bushnell-Wye, G., *J. Mat. Res.,* **12**, 264, 1997.

[4.17] Glatter, O., Kratky, O., *Small Angle X-ray Scattering*, Academic Press Inc, London, 1982.

[4.18] Feigin, L.A., Svergun, D.I., *Structure Analysis by Small-Angle X-ray and Neutron Scattering*, (Ed G. W. Taylor), Plenum Press, New York, 1987.

[4.19] Guinier, A., *Ann. Phys.,* **12**, 161, 1939.

[4.20] Gardner, M.A., MSc Thesis, *Small Angle X-ray Scattering Studies of Porous Carbons*, November 1991, University of Kent.

[4.21] Debye, P., Bueche, A.M.T., *Appl. Phys.,* **20**, 518, 1949.

[4.22] Porod, G., *Kolloid-2*, **124**, 83, 1951.

[4.23] Debye, P., Anderson, H.R., Brumberger, H., *J. Appl. Phys.,* **28**, 679-683, 1957.

[4.24] www.srs.dl.ac.uk/ncd/computing/manual.otoko.html

[4.25] Toebbens, D.M., Stuesser, N., Knorr, K., Mayer, H.M., Lampert, G., *Materials Science Forum*, **378**, 288-293, 2001.

Chapter 5

Materials and Methods

5.1 Sample Preparation

5.1.1 Introduction

Two types of bioactive glass, namely melt-quenched and sol-gel, have been investigated in this study. The details of each type of material have been outlined in previous chapters. Below, the two methods of preparation are outlined.

5.1.2 Melt-quenched Glasses

The melt-quenched glasses are of general compositions CaO-Na_2O-P_2O_5-SiO_2. The melt-quenched bioactive glasses were prepared by Novamin Technology, Inc (Alachua, Florida, USA). They were made by conventional glass manufacturing methods (i.e. preparing raw materials, melting, forming, and annealing). The compositions of the glasses need to be carefully controlled, ensuring the components are well mixed in precise proportions before being fed into a melting furnace. Purity of raw materials must be ensured, contamination of the glass must be avoided in order to retain the chemical reactivity of the material. Analytical grade components are typically used for most components. Weighing, mixing, melting, homogenising and forming of the glass must be done without introducing impurities or losing volatile constituents such as Na_2O or P_2O_5. Melting is usually done in the range of 1300-1450 ºC in a platinum crucible, depending on composition, specifically for Bioglass® 1370 ºC. The molten glass is quenched with distilled water, then rinsed with acetone to stop any reaction with the water. Bulk specimens are formed by casting or injection moulding in graphite or steel moulds. Annealing at 450-550 ºC is crucial, because of the high coefficient of thermal expansion of the bioactive glass compositions. Several compositions of bioactive melt-quenched glasses were investigated in this study. Below is Table 5.1 showing the batch compositions of the glass samples in weight %.

Sample name	SiO_2 / wt % (mol %)	CaO / wt % (mol %)	Na_2O / wt % (mol %)	P_2O_5 / wt % (mol %)
45S5 (MQ)	45 (46.1)	24.5 (26.9)	24.5 (24.4)	6 (2.6)
52S5 (MQ)	52	21	21	6 (2.6)
55S5 (MQ)	55 (55.1)	19.5 (22.2)	19.5 (20.1)	6
77S5 (SOL)	77 (80.0)	14 (16.0)	N/A	9 (4.0)

Table 5.1: Theoretical wt% compositions of different bioactive glasses. (MQ denotes melt-quenched and SOL denotes sol-gel).

One sample investigated was a bioactive sol-gel glass, with composition shown in Table 5.1. This glass was produced via the sol-gel route, which is a lower temperature route to that of melt-quenching. This has many advantages which are outlined in chapter 3. This sample was also prepared by Novamin Technology, Inc (Alachua, Florida, USA), by hydrolysis and polycondensation of tetraethyl orthosilicate (TEOS) and triethyl phosphate (TEP). Calcium nitrate tetrahydrate ($Ca(NO_3)_2 4H_2O$)

was used to catalyse the TEOS and TEP hydrolysis, and each reactant was consecutively added under continuous stirring. The solution was then introduced into a furnace, and aged at 60 ºC for 52 hours. The gel was then dried at 150 ºC for 78 hours under high humidity conditions and then stabilised at 700 ºC. Melt-quenched samples were prepared as powders and also as solid discs, the sol-gel sample was produced as a powder only.

5.1.3 Sol-gel Glasses

The foamed bioactive $(CaO)_{0.3}(SiO_2)_{0.7}$ sol-gel glasses were prepared by the Centre for Tissue Engineering and Repair, Department of Materials, Imperial College of Science, Technology and Medicine. The procedures used to prepare the foams were based on previously established procedures [5.1, 5.2]. A schematic representation of the manufacture of these foams can be found in Figure 5.1 below.

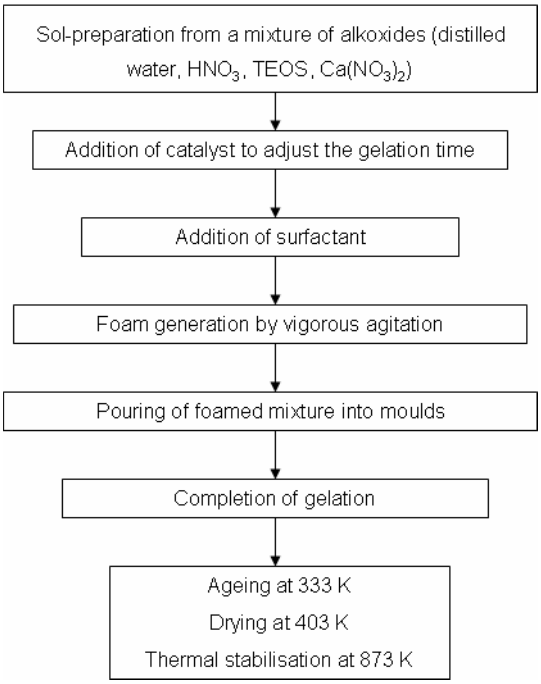

Figure 5.1: Schematic representation of the manufacture of foams.

The sol-gel precursors used in the foams are shown in Figure 5.1. The calcium nitrate ($Ca(NO_3)_2$) is hydrolysed in the presence of 2N nitric acid (HNO_3), giving calcium nitrate tetrahydrate ($Ca(NO_3)_24H_2O$).

Initially the procedure involves preparing the sol-gel by a mixture of distilled water, the appropriate alkoxide precursors and salts, and the catalyst for hydrolysis, nitric acid.

The foaming of the sol-gels takes place after hydrolysis. The sol is foamed with the addition of surfactant (Teepol, an ionic surfactant) and vigorous agitation. The condensation is catalysed with an acidic addition (0.1 wt% HF). As sol viscocity rises, the foamed sol is then placed into moulds, then sealed to age at 60 ºC for 72 hours. The temperature is then increased to 130 ºC after containers are opened slightly to allow slow solvent evaporation. Thermal stabilisation is carried out to 600 ºC, to allow partial densification of the matrix. Some foam samples were further heated to 800 ºC and 1000 ºC to investigate the affect of temperature on the structure and bioactivity of the foams.

5.2 Sample Characterisation

5.2.1 Introduction

The analysis of X-ray and neutron diffraction depends on accurate knowledge of the chemical composition of the sample and the sample density. Several characterisation techniques were employed in this study to investigate the compositions of each sample. Each of these techniques are explained below, along with the method for measuring the density of samples.

5.2.2 X-ray fluorescence

X-ray fluorescence (XRF) is a non destructive analytical technique which is fast and yields elemental composition of samples. XRF uses the photoelectric effect, in which the initial x-ray has sufficient energy to eject an electron from the inner shells to create a vacancy. These vacancies present an unstable condition for the atom, and the atom returns to a stable condition by filling the vacancy with an electron from the next shell out – thus creating a new vacancy which in turn will be filled from a higher shell, and so on. This process of filling the inner shell produces a characteristic x-ray whose energy is the difference between the binding energy of the corresponding shells. Thus, a typical spectrum from an irradiated sample will display multiple peaks of different intensities. The elements that are present in a sample can be identified by the energy location of their characteristic peaks. Since, in theory, the number of photons produced is proportional to the number of atoms present in the sample, quantitative elemental concentrations can be determined from the net intensities of the observed peaks.

The XRF measurements were carried out on a Bruker AXS S4 Explorer instrument. Approximately 10-15 mg of each sample was loaded into sample holders, held in place using 3 μm mylar film. Each sample scan lasted ~20 minutes. The data collected was analysed using the instrument's internal Bruker analysis program to provide the relevant oxide concentrations; charge-balancing stoichiometry was assumed in order to calculate the oxygen content of the samples. The results of all sample analyses are presented in the relevant results chapter.

5.2.3 Inductively Coupled Plasma

Elemental compositions for some samples were verified using inductively coupled plasma optical emission spectroscopy (ICP-OES). ICP spectroscopy techniques are so-called wet sampling techniques, whereby samples are introduced in liquid form for analysis. In ICP-OES, a sample solution is introduced into the core of inductively coupled argon plasma, which generates an effective temperature of approximately 8000 °C. At this temperature all elements become thermally excited and emit light at their characteristic wavelengths. This light is collected by the spectrometer and passes through a diffraction grating that serves to resolve the light into a spectrum of its constituent wavelengths. Within the spectrometer, this diffracted light is then collected by wavelength and then amplified to yield an intensity measurement that can be converted to an elemental concentration by comparison with calibrated standards. The ICP-OES analysis was performed by MEDAC Ltd, using a Varian Vista MPX ICP-OES system. The powdered glass samples were digested in hydrogen fluoride (HF) to produce the sample solutions needed for the analysis. Again the relevant analysis of samples is presented in the results chapters.

5.2.4 Raman Infra-Red Spectroscopy

Both infrared (IR) and Raman spectroscopies give rise to a set of absorption or scattering peaks as a function of energy. These constitute a vibrational spectrum. Individual peaks in the spectrum correspond to energies of vibrational transitions within the sample, or in more common terminology, to the frequencies of its vibrational modes. Since a vibrational spectrum is dependent on the interatomic forces in a particular sample, it is a sensitive probe of microscopic structure and bonding within the material. Vibrational spectroscopy can provide much useful structural information from the positions, symmetries and relative intensities of observed peaks, and any changes in these with variables such as temperature, composition and applied pressure [5.3].

As mentioned above vibrational transitions can be observed as infrared or Raman spectra, however the physical origins of these two spectra are markedly different. Raman spectra have their origin in the electronic polarisation caused by ultraviolet (UV), visible and near-IR light. If a molecule is irradiated by monochromatic light of frequency v, then, because of electronic polarisation induced in the molecule by this incident beam, the light of frequency v (Rayleigh Scattering), as well as that of frequency $v+v_i$ (Raman Scattering) is scattered where v_i represents a vibrational frequency of the molecule. Thus, Raman spectra are presented as shifts from the incident frequency in the UV, visible and near-IR region.

When performing Raman Infra-red spectroscopy, little sample preparation is needed, and the technique is non-destructive.

Raman infra-red spectroscopy was performed by Dr Simon FitzGerald, of HORIBA Jobin Yvon Ltd. The measurements were taken on a LabRAM 800 bench top Raman microscope, using an air cooled CCD detector, and two lasers of 50 and 18 mW. Samples were analysed without pre-treatment, using 633 nm (red) and 532 nm (green) lasers.

5.2.5 Pycnometry

Pycnometry is a method of measuring the volume of a sample based upon Archimedes' displacement principle. It can be used on powdered and porous materials as well as solid samples. Measurements are made using air, or in this study, helium displacement. Two chambers of equal volume, a reference piston and a measurement piston record the pressure change needed to balance the two chambers when the sample is placed inside the measurement chamber. This change in pressure can be used to calculate the volume of the sample. True volume is measured and hence, by measuring mass of sample used the true density can be calculated. Measurements were carried out on a Quantachrome Multipycnometer. The amount of sample used varied, as precision is enhanced with larger amounts of sample.

5.3 The Apatites

5.3.1 Introduction

As mentioned in Chapter 2, the characteristics looked for in these bioactive glasses are the formation of an apatite layer on their surface when immersed in an aqueous medium. Within this thesis, more than one type of apatite is discussed, namely Hydroxyapatite, hydroxycarbonate apatite and tricalcium phosphate. This section will briefly describe the general structure of the apatites.

5.3.2 Structure

The structure of the apatites can be thought of as unconnected PO_4^{3-} tetrahedral with Ca^{2+} ions in the spaces between, and in order to balance the charge, a column of X^- ions along the *c* axis. [5.4] It is this column of anions, its type and location, which distinguishes the various calcium apatites. Two different kinds of structures have been distinguished; hexagonal and monoclinic structures, with the latter being adopted if the compound is stoichiometric. [5.4] An examples of the hexagonal structure can be seen in Figure 5.2.

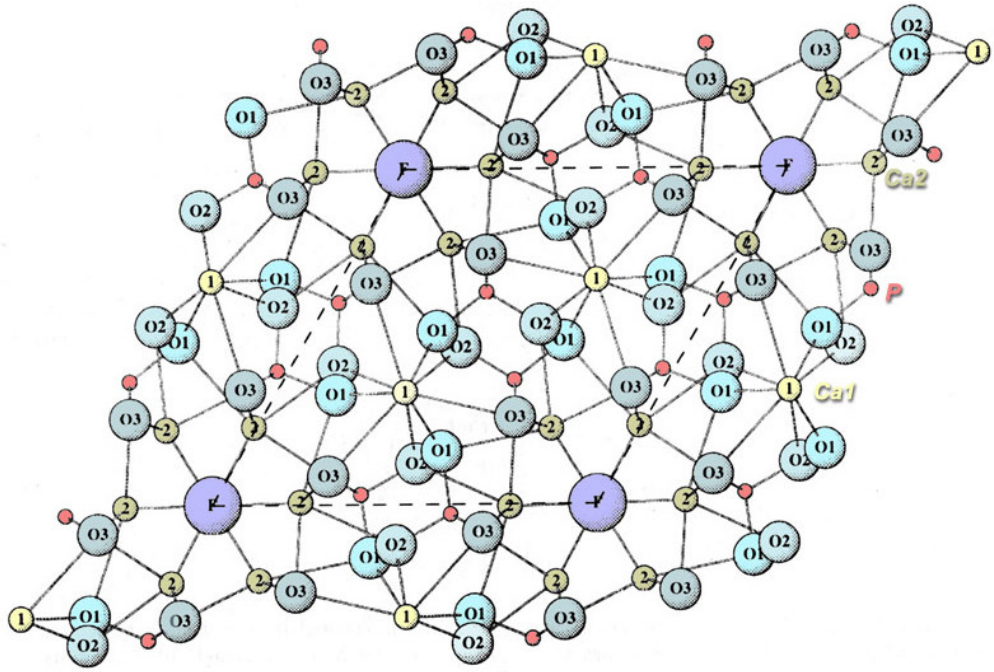

Figure 5.2: Illustration of the hexagonal crystal structure of a typical apatite, $Ca_5(PO_4)_3(F,OH,Cl)$ [5.5]

In FA, at room temperature X-ray diffraction measurements show a hexagonal unit cell containing two units per unit cell, with the F^- ions lying at the centre of the calcium triangles. [5.4] CA, at room temperature, is reported to have a monoclinic structure with four formula units per unit cell, but once at a temperature of 310 °C a hexagonal structure with two formula units per cell has been observed. In the monoclinic structure, the Cl^- ions are shifted up and down in alternating chains whereas in the hexagonal the four chlorine sites are half occupied by the two atoms per cell. [5.4] HA also shows a phase transition; from a monoclinic structure with four formula units per cell to a hexagonal structure around 370 °C. The structure of the hexagonal phase of HA presents a problem: there are four possible sites for the two OH groups per unit cell. Thus the assumption of 0.5 occupancy per site was made, resulting from disorder in every anion column or disorder from column to column. [5.6]

Phosphorus NMR at 68.4 MHz and MAS NMR of an amorphous calcium phosphate shows that they are very similar to HA. However, proton enhancement studies show that ACP is not a poorly crystalline HA, nor a mixture of HA with calcium phosphate phases containing HPO_4^{2-} ions, but a unique compound with some heterogeneity. The conclusion is that PO_4^{3-} ions are slightly distorted and/or weakly bound to protons. [5.7]

Carbonate apatites are prepared by precipitating apatites or hydrolysing amorphous calcium phosphates in the presence of CO_3^{2-} or HCO^{3-} ions. The effect is the reduction in the crystallinity of the apatite, or the prevention of its formation. Tamai et al. [5.8] reported on the microstructural changes in the initial stage of conversion of α-tricalcium phosphate (α-$Ca_3(PO_4)_2$) (α-TCP) to HA in aqueous solution. The process involved surface coverage of the α-TCP with amorphous calcium phosphate, as a result of the hydration and/or dissolution of the α-TCP, followed by the nucleation of the HA on the amorphous layer, the growth of dendritic structures which would finally develop into needlelike fine HA crystals.

<u>References</u>

[5.1] Sepulveda, P., Binner, J.G.P., *J. Eur. Ceram. Soc.,* **19**, 2059-2066, 1999.

[5.2] Li, R., Clark, A.E., Hench, L.L., *J. Appl. Biomater.,* **2**, 231-239, 1991.

[5.3] McMillan, P.F., Hofmeister, A.M., *Mineralogy and Geochemistry*, **18**, 99-159, 1988.

[5.4] Calderin, L., Stott, M.J., Rubio, A., *Physical Review B*, **67,** 134106, 2003.

[5.5] http://www.geol.lsu.edu/henry/Geology7900/Apatite/Apatite.htm

[5.6] Kay, M.I., Young, R.A., *Nature*, **204**, 1050, 1964.

[5.7] Elliott, J.C., Structure and Chemistry of the Apatites and other Caclium Orthophosphates, Elsevier Science, Amsterdam, The Netherlands, 1994.

[5.8] Tamai, M., Isshiki, T., Nishio, K., Nakamura, M., Nakahira, A., Endoh, H., *Journal Materials Research*, **18(11)**, 2633, 2003.

Chapter 6

Quaternary melt-quenched bioactive glasses

6.1 Introduction

This chapter describes the work undertaken investigating the atomic scale structure of a group of melt-quenched bioactive glasses containing SiO_2, CaO, Na_2O and P_2O_5. The different compositions were investigated using X-ray diffraction in order to gain an insight into the structure of these materials and to compare the structure of glasses with different levels of bioactivity. The most bioactive composition, namely Bioglass® (45S5), was looked at in more detail, utilising NMR data, combined with X-ray diffraction, neutron diffraction and reverse Monte Carlo modelling, to facilitate a more complete understanding of the material and to correlate the structure with its observed bioactivity.

6.2 X-ray diffraction of melt-quenched bioactive glasses

X-ray diffraction measurements were performed on a series of melt-quenched bioactive glasses, namely 45S5, 55S5, 60S5 (where S denotes the network former SiO_2 in 45% followed by a specific Ca/P molar ratio of 5) and also one composition of an analogous (i.e. it has similar biological properties but has different elemental composition) sol-gel bioactive glass, 77S5.

The samples of bioactive glass were supplied by Novamin Technology, Alachua, FL. The samples were in granular form, the composition and density of which are reported in Table 6.1. Composition analysis was performed using a Bruker

S4 X-ray fluorescence spectrometer. Density measurements were performed using a Quantachrome multipycnometer and were based on the use of He as the probe gas.

ICP analysis was used in conjunction with XRF data to corroborate the composition of Bioglass® (as were some bioactive calcia-silica sol-gel foams investigated in chapters 8 and 9). The ICP results have been set aside however, as for glasses with labile components such as Ca in these samples, the results constantly underestimate the calcium content. This is most likely due to the fact that a significant amount of calcium is leached out prior to the equipment beginning to record data. Hence, in this thesis, XRF was relied upon to provide the compositional values for all samples.

The high energy X-ray diffraction (HEXRD) data were collected on Station 9.1 at the synchrotron radiation source (SRS), Daresbury Laboratory, UK. The finely powdered samples were enclosed inside a 1 mm thick circular aluminium annulus by polyimide windows, and mounted to provide a flat-plate $\theta:2\theta$ sample geometry. The wavelength was set at $\lambda = 0.4875$ Å, and calibrated using the K-edge of a Ag foil; this value is low enough to provide data to a high value of momentum transfer ($\hbar Q$, where $Q_{\max} = 4\pi \sin\theta/\lambda \sim 23$ Å^{-1}; 2θ is the scattering angle, and λ is the wavelength of the diffracted radiation). The data were corrected using a suite of programs written in-house, as described in chapter 4, section 4.4.

	45S5	**55S5**	**60S5**	**77S5**
Density / gcm^{-3} (+/- 0.002)	2.708	2.624	2.612	2.309
Density / atoms Å^{-3}	0.07761	0.07589	0.07592	0.06676
mol%				
CaO	26.9	22.2	19.6	16.0
SiO_2	46.1	55.1	60.1	80.0
P_2O_5	2.6	2.6	2.6	4.0
Na_2O	24.4	20.1	17.7	-
atomic % (+/- 0.003)				
Ca	0.101	0.082	0.072	0.059
Si	0.161	0.191	0.207	0.275
P	0.004	0.004	0.004	0.006
Na	0.083	0.068	0.059	-
O	0.651	0.655	0.658	0.660

Table 6.1: Sample characterisation on the basis of XRF, (using charge balancing to determine oxygen concentrations), and helium pycnometry.

Figure 6.2 shows the *T(r)* functions for three compositions of melt-quenched bioactive glass and one sol-gel bioactive analogue after Fourier transformation of the experimentally derived *S(Q)* (shown in Figure 6.1) into *r*-space, together with the simulation to the pair distribution function obtained using the method described in chapter 4, section 4.4.

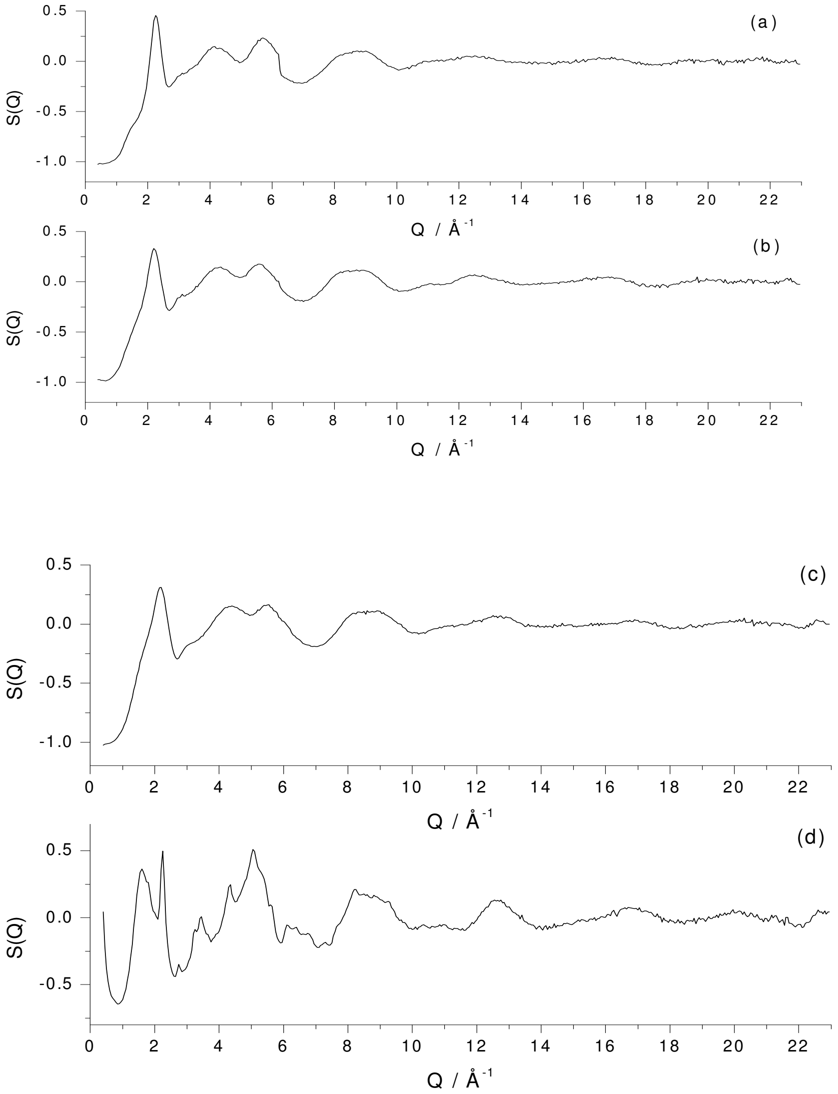

Figure 6.1: High energy X-ray diffraction data from: (a) the 45S5 Bioglass melt-quenched sample: *Q*-space interference function *S(Q)* (b) the 55S5 Bioglass melt-quenched sample: *Q*-space interference function *S(Q)*, (c) the 60S5 Bioglass melt-quenched sample: *Q*-space interference function *S(Q)*, and (d) the 77S5 Bioglass sol-gel sample: *Q*-space interference function *S(Q)*.

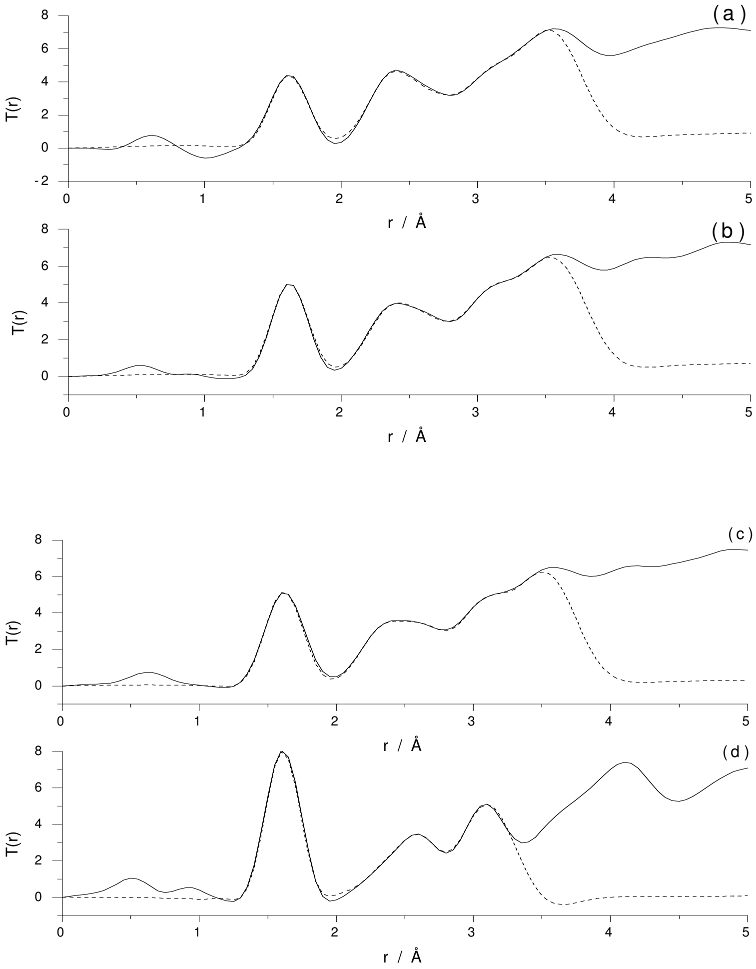

Figure 6.2: High energy X-ray diffraction data from: (a) the 45S5 Bioglass melt-quenched sample - pair distribution function, *T(r)*, (solid line) together with fit (dashed line), (b) the 55S5 Bioglass melt-quenched sample - pair distribution function, *T(r)*, (solid line) together with fit (dashed line), (c) the 60S5 Bioglass melt-quenched sample - pair distribution function, *T(r)*, (solid line) together with fit (dashed line), and (d) the 77S5 Bioglass sol-gel sample - pair distribution function, *T(r)*, (solid line) together with fit (dashed line).

Three distinct features can be observed in all four cases. The peak centred around 1.6Å is associated with the Si-O (1.61 Å) and P-O (1.43 and 1.58 Å) pairwise correlations, and the peak at ~2.5 Å is assigned to three Ca-O bond distances of 2.32, 2.5, 2.76 Å, along with the O-O nearest-neighbour distance at 2.64 Å and also the Na-O distance at 2.4 Å (with the obvious exception of the sol-gel sample). Finally, the double peak centred at 3.5 Å is associated with the Si···Si second-neighbour pairwise correlation (3.03 Å) and the corresponding Si···Ca, Ca···Ca correlations at 3.22, 3.5 Å respectively along with contributions from Ca···P, Na···Ca and Na···Na. The assignments of the Si-O and O···O correlations are made on the basis of previous HEXRD results from metal-doped sol-gel derived silicate glass [6.1], and the assignment of the distances involving Ca are based on an experiment undertaken on a bioactive calcia-silica sol-gel glass using neutron diffraction with isotopic substitution [6.2]. The assignment of the Na-O distance is based on work by Du and Cormack [6.3]. The assignment of P-O distances are based on a study of vitreous P_2O_5 [6.4]. It is evident that, on the basis of the structural parameters derived from the simulation process, shown in Figures 6.4 and 6.5, significant structural changes are occurring in these materials both as a function of composition and of preparation method. It is possible in all cases to simulate a Si-O peak at 1.61 Å with a coordination of ~4, although we note the fact that the coordination number is on average slightly higher than 4 as simulated. This is probably associated with residual uncertainties in sample density and composition, which will affect the peak areas directly, and in the absence of independent data we have chosen not to scale the *T(r)*. Naturally therefore, all other simulated coordination numbers are also likely therefore to be marginally higher than they ought to be. In all samples we obtain an O-Si-O peak at ~2.64 Å however the coordination varies with Si content from ~4-6. All samples have a Si···Si distance of ~3.03 Å as expected and a coordination of ~4, however this coordination decreases as the amount of Ca increases. All samples also have a Si···Ca distance of ~3.22 Å and a coordination of 2.80 which decreases to 1.50 as Ca content decreases. The total Ca-O coordination over all three correlation distances is ~6.1, which agrees well with the results of earlier experimental [6.5] and molecular dynamics [6.6] studies on melt-quenched calcium silicate glasses. All melt quenched samples showed a Na-O pair correlation peak at ~2.40 Å with a coordination of ~6, the 77S5 sol-gel glass however showed one obvious difference in the pair distribution function compared with the melt-quenched samples, namely the absence of this Na-O pair correlation peak (- the sol-gel sample contained no Na_2O). This can clearly be seen in Figure 6.3. The absence of Na is obvious and also the absence of some Ca is also apparent, along with the effect of the higher Si content.

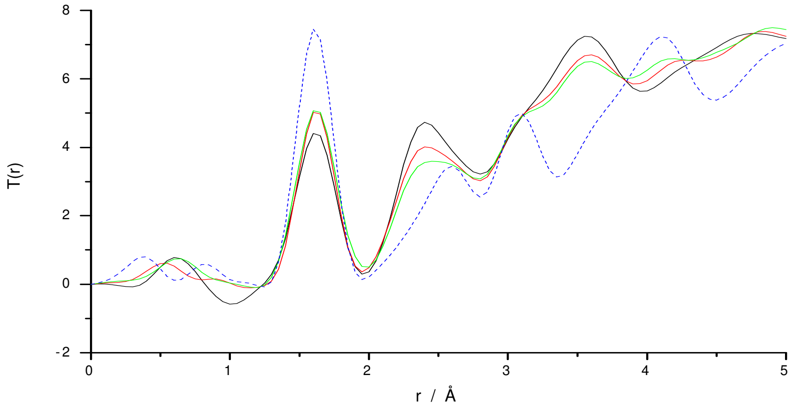

Figure 6.3: High energy X-ray diffraction data from: (a) the 45S5 Bioglass melt-quenched sample: pair distribution function, *T(r)*, (solid black line), (b) the 55S5 Bioglass melt-quenched sample: pair distribution function, *T(r)*, (solid red line) (c) the 60S5 Bioglass melt-quenched sample: pair distribution function, *T(r)*, (solid green line), and (d) the 77S5 Bioglass sol-gel sample: pair distribution function, *T(r)*, (dotted blue line).

The results in Figures 6.4 and 6.5 show that three pairwise correlations characteristic of the host silica network are present in the data presented here: the Si-O bond at 1.61 Å, the O-Si-O nearest-neighbour distance at 2.64 Å and the Si-O-Si nearest-neighbour distance at 3.03 Å.

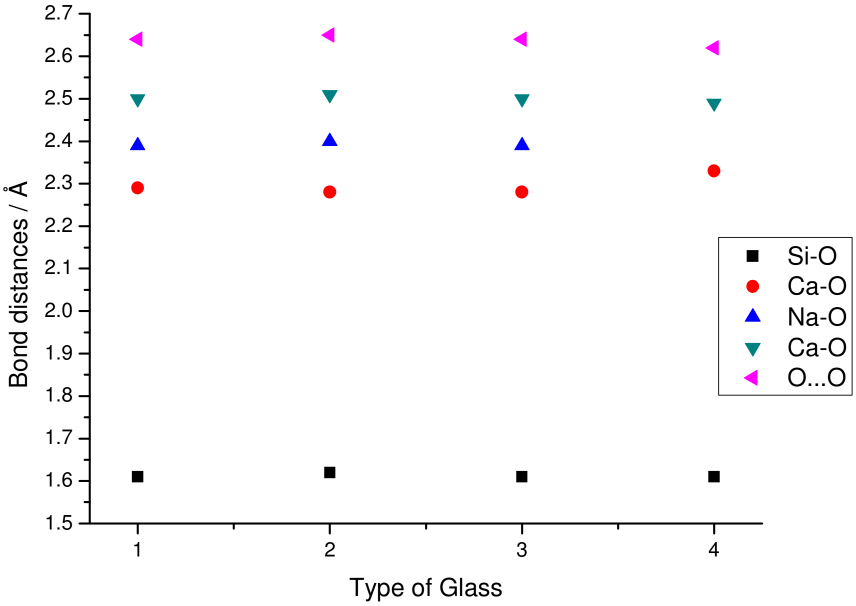

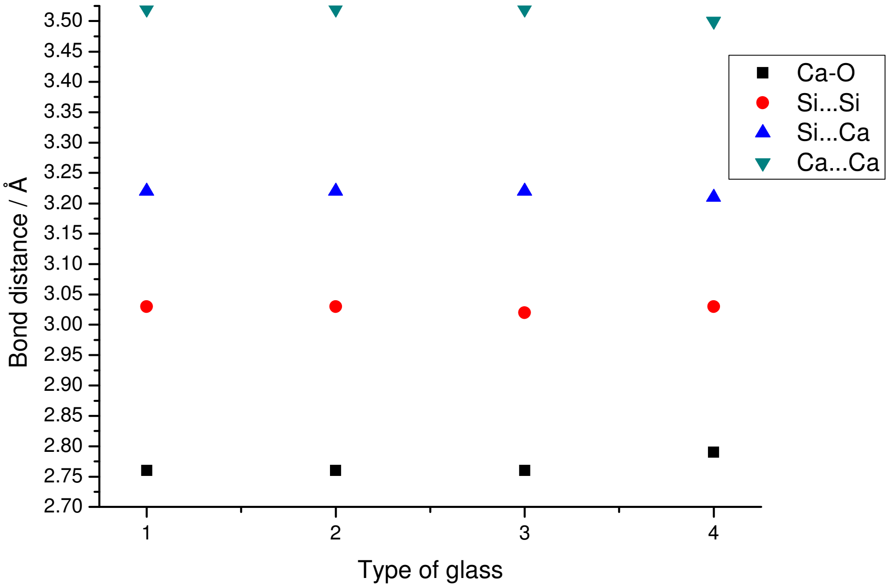

Figure 6.4: Graphs showing the bond distances for the Bioglass® samples obtained by fitting the high energy X-ray diffraction pair distribution functions. Note that errors are ± 0.02 Å, and glasses 1-4 correspond to increasing SiO_2 content.

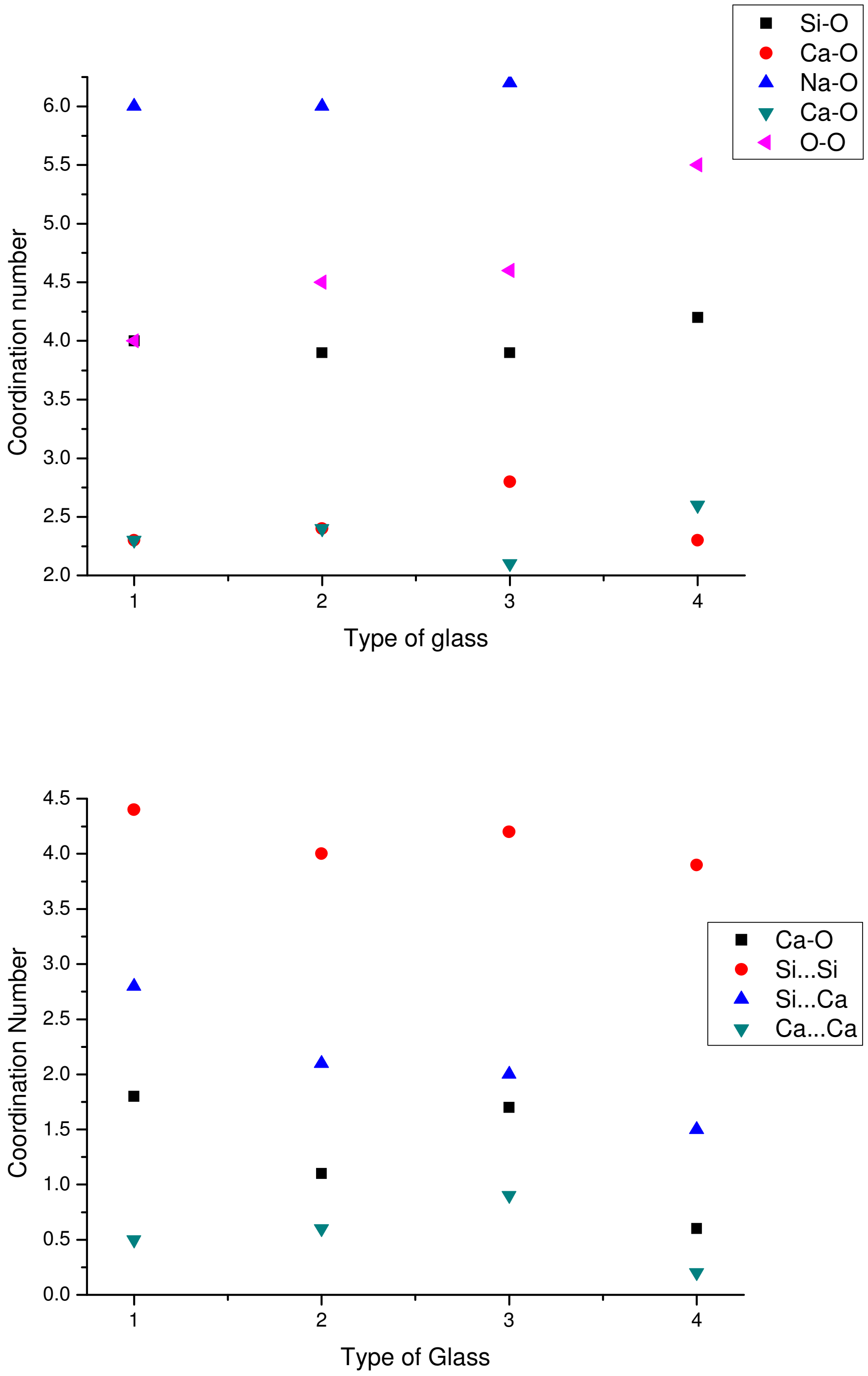

Figure 6.5: Graphs showing the coordination numbers for the Bioglass® samples obtained by fitting the high energy X-ray diffraction pair distribution functions. Note that errors are ± 15%, and glasses 1-4 correspond to increasing SiO_2 content.

The O-Si-O coordination number would tend towards six in a fully densified silica network, but in these samples the coordination is ~4 in the 45S5 sample which has the lowest concentration of Si, whereas in the sol-gel sample, which has the highest concentration of Si the coordination is ~5.5. The results show a general trend of decreasing O-Si-O coordination number with increasing Ca and Na content suggesting Ca or Na is acting as a network modifier. The Si-O-Si coordination number should exhibit a similar trend with composition, although the errors associated with this parameter are much larger because this Si···Si first neighbour correlation is not resolved in the pair distribution functions themselves. We note here that all Si···Si coordination numbers are 4 or greater which one would not expect unless in a fully densified silica network. This is attributed to the fact that the Si···Si peak is not well resolved from overlapping correlations; furthermore, due to residual uncertainties in composition (most notably in the case of the sol-gel sample) and the effect this may have on the corrections used in data analysis, there may be a systematic error in the areas of the *T(r)* peaks. All the samples can be simulated with three Ca-O distances with a total coordination number of between 5 and 6.5. This agrees with a previous experiment on a bioactive sol-gel glass [6.2]. The Na-O peaks all have a distance of ~2.40 Å and a coordination of ~6. The distance agrees with previous published data [6.3].The coordination of ~6, again recalling that all coordinations will be marginally higher than they should be, agrees well with that expected for α-$Na_2Si_2O_5$, as in this material sodium coordination numbers are five and six [6.8]. We note that in our simulations we have a large number of partial correlation functions, and it may therefore be beneficial in a heuristic sense to combine the Ca-O and Na-O correlations with one modifier–oxygen, M-O, pseudo-correlation. Assuming a material of the generic formula $MO_x(SiO_2)_{1-x}$, parameters for the M-O correlations have been found by a weighted averaging all of the M-O correlation peaks within our *T(r)* simulations. These results are shown for reference purposes in Table 6.2. Due to and the need to employ accurate form factors for all pairwise terms in producing the simulations, it is of course not practicable to produce a simulation of the data from ‘first principles’ assuming a material of $MO_x(SiO_2)_{1-x}$.

Sample	Correlation	*R* / Å	N	*σ* / Å
45S5	Si-O	1.61	4.0	0.06
	M-O	2.49	12.4	0.19
	O···O	2.64	4.0	0.14
	Si···Si	3.03	4.4	0.11

Sample	Correlation	*R* / Å	N	*σ* / Å
55S5	Si-O	1.62	3.9	0.06
	M-O	2.49	11.9	0.19
	O···O	2.65	4.5	0.14
	Si···Si	3.03	4.0	0.11

Sample	Correlation	*R* / Å	N	*σ* / Å
60S5	Si-O	1.61	3.9	0.07
	M-O	2.49	12.8	0.18
	O···O	2.64	4.6	0.10
	Si···Si	3.02	4.2	0.11

Sample	Correlation	*R* / Å	N	*σ* / Å
77S5	Si-O	1.61	4.1	0.05
	M-O	2.52	5.6	0.17
	O···O	2.62	5.8	0.11
	Si···Si	3.03	3.9	0.13

Table 6.2: Weighted average simulated parameters assuming a generic sample $MO_x(SiO2)_{1-x}$; uncertainties are the same as those quoted in Figures 6.4 and 6.5.

P-O contributions have been included only in the 77S5 sample since, in the melt-quenched samples, only 2.6 mol% P_2O_5 is present, whereas the 77S5 sol-gel sample contains 4 mol% P_2O_5. The results for the 77S5 sol-gel sample show two separate P-O distances corresponding to the separate P-bridging oxygen bonds (P-O_b), and the P-non bridging oxygen bonds (P-O_{nb}). The correlation at 1.43 Å is assigned to the P-O_{nb} bonds and has a coordination of ~3. The correlation at 1.58 Å is assigned to the P-O_b bond and has a coordination of ~1. This agrees well with NMR data carried out by Novamin Technology [6.9], which showed that 45S5 Bioglass® contains mostly orthophosphate (Q^0) units, and that as the Si and P content increases, an increase in pyrophosphate (Q^1) units occurs.

6.3 In-depth structural study of Bioglass®

For a relatively complex system such as this multicomponent glass, no one structural probe is able to provide a definitive structural model. Complementary methods need to be employed within a materials-centred methodology. In this study both X-ray and neutron diffraction are employed, alongside solid state NMR measurements using several key nuclei.

There is a significant difference between the experimentally determined X-ray and neutron structure factors due to the differences in weighting factors derived using the following equation

$$T(r) = \sum_{ij} n_i n_j Z_i Z_j T_{ij}(r) \qquad (6.1)$$

where $T_{ij}(r)$ are the partial correlation functions for pairs of atomic species i and j, n_i is the fraction of atom type i, and Z_i is the atomic number (X-rays) or coherent scattering length (b_i neutrons). The pair correlation weighting factors are shown graphically for each partial in Figure 6.6.

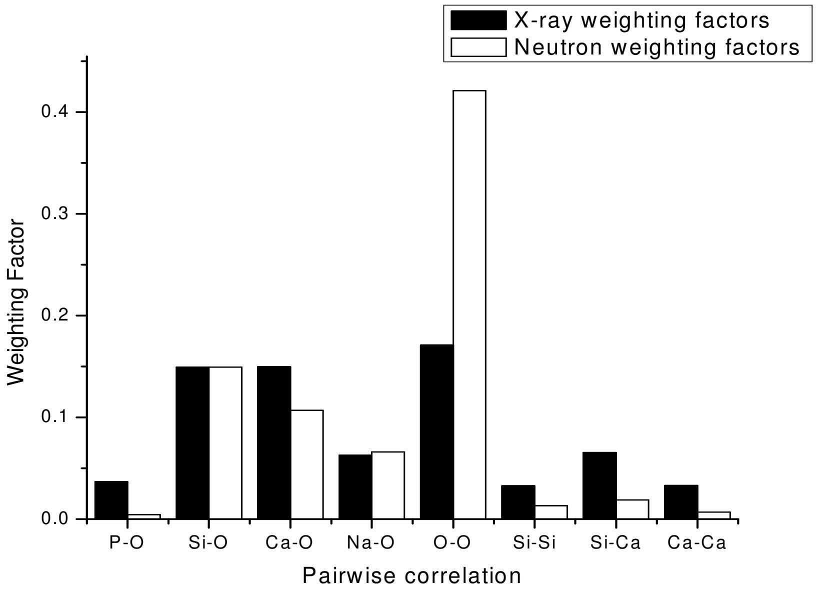

Figure 6.6: Histogram comparing relative X-ray and neutron scattering weighting factors for each pair correlation peak analysed in the fitting process (the total areas have in both cases been normalised to unity.)

This figure demonstrates that X-ray diffraction data are to be preferred for studying the intermediate-range order of oxide glasses, because the weighting factors of the Si···Si, Si···Ca and Ca···Ca correlations, which are strongly related to intermediate-range order of these glasses, are relatively larger for X-rays than for neutrons. The figure also shows that the neutron data is better conditioned for obtaining data associated with O···O correlations (as well as for the provision of better resolved real-space data *per se* as per equation 4.33 in section 4.3 of chapter 4. To this information the element-specific short-range data derived from NMR is added; the ability to use all of this data simultaneously within a single cogent model building process leads to the generation of a robust structural picture of the material.

The samples of Bioglass$^{®}$ for X-ray diffraction and solid state NMR experiments were supplied by Novamin Technology, Inc. The samples were in granular form. The Bioglass$^{®}$ sample for neutron diffraction was supplied by Imperial College London, prepared in the same fashion, but caste in the form of a solid glass rod. Composition analysis for both sets of samples was performed using a Bruker S4 X-ray fluorescence instrument. Density measurements were based on helium pycnometry performed using a Quantachrome multipycnometer. Composition and density results for both samples are shown in Table 6.3.

	Bioglass® powder sample for XRD	Bioglass® rod sample for ND
Density g/cm^3	2.709	2.700
Density atoms/ Å^{-3}	0.077	0.077
Composition XRF / mol%		
CaO	26.9	26.2
SiO_2	46.1	47.2
P_2O_5	2.60	3.15
Na_2O	24.4	23.8
Composition of Model / mol%		
CaO	25.9	26.2
SiO_2	48.0	47.2
P_2O_5	2.60	3.15
Na_2O	23.1	23.8
Side Length of RMC box / Å	32.78	32.77

Table 6.3: Sample characterisation: density measurements are based on helium pycnometry; X-ray fluorescence was used to provide compositional analysis. The compositions used in the RMC model were obtained on the basis of XRF measurements, charge balancing and solid state NMR data.

The high energy X-ray diffraction (HEXRD) data is the data described in the previous section. The neutron diffraction (ND) data was collected on the GEM total scattering instrument at the ISIS pulsed muon and neutron source at the Rutherford Appleton Laboratory. The data was reduced using the program *gudrun* described in Appendix 2. The ^{23}Na, ^{29}Si, ^{31}P NMR spectra were measured on a Bruker ASX-400 spectrometer (9.45 T) using a Bruker HP WB 73 A MAS probe at 105.857, 79.49 and 16 997 MHz, respectively. The ^{23}Na and ^{31}P NMR measurements were made using a 4 mm probe (typically 0.14 g sample size) at 13.0 to 13.5 kHz sample spinning, while the ^{29}Si NMR measurements were made using a 7 mm probe (0.64 g sample) at 7 kHz sample spinning speed. The ^{29}Si and ^{31}P NMR spectra were acquired using a single-pulse sequence. The ^{23}Na NMR spectrum was acquired using a spin-echo pulse sequence to suppress the effect of "probe ringing" and to obtain a flat baseline. An echo time of one rotor period ($1\tau = 76.92$ μs) was used. The chemical shifts (δ) were referenced to 1M NaCl for ^{23}Na and 85% H_3PO_4 for ^{31}P (0 ppm). The ^{29}Si spectrum was referenced to a secondary standard of kaolinite ($\delta = -91.5$ ppm relative to tetramethylsilane as its primary standard). The 90° pu1se widths for ^{29}Si and ^{31}P NMR were 5 μs and 3.5 μs, respectively. A selective pulse width of 2.5 μs (half of the liquid 90° pulse length) was used for ^{23}Na to observe the central transition (½↔-½). The recycle delay times used for ^{23}Na, ^{31}P and ^{29}Si were 1 s, 3 s and 60 s, respectively. These values are sufficiently long to allow the complete relaxation necessary to obtain quantitative information about spin populations. The total number of scans used for ^{23}Na, ^{29}Si and ^{31}P NMR spectra were 512, 256 and 5000, respectively. The NMR data was collected by Dr Gautam Sarkar and Dr John FitzGerald of South Dakota State University and analysed by Dr Dave Pickup of the University of Kent.

The RMC model box for the Bioglass® is made up of ~3000 atoms, with correct atomic number density and composition obtained from pycnometry measurements and X-ray fluorescence composition analysis respectively, as per Table 6.3. Charge-balancing was also used as an aid to building a box with the correct composition (especially important in terms of refining the oxygen content). The size chosen for the associated cubic box, determined in order to match the measured density, is also shown in Table 6.3.

In order to obtain as a starting configuration the four oxygen atoms around each silicon atom suggested on the basis of prior chemical knowledge, a random array of Si atoms was produced first which were moved out to a minimum distance of 2.85 Å, and then O atoms were inserted at the medium distance between each pair of neighbouring Si atoms. The P atoms, and corresponding additional O atoms, were then added to this pseudo-silica array at random positions. The details of the bonding constraints imposed via the RMC algorithm were decided upon using the solid state NMR values for Q speciation (i.e. the relative numbers of O_b and O_{nb}). Specifically, for the Q^2 units, the atoms in the box were moved such that each silicon atom was coordinated to two O_b and two O_{nb} (and each O was coordinated to only two other atoms, neither of which could be another O). After the base silica network was produced and phosphorous was included, the Ca and Na atoms were added randomly. Within this initial phase of defining the configuration of the box, there are two other considerations of importance: the definition of distances of closest approach for each pair of atom types, and the choice and use of the target goodness-of-fit value, σ. The latter parameter, along with the magnitude of the individual atom movements at each step, may be varied to help optimise the speed with which the constraints (and eventually the experimental data) are satisfied; ultimately however its value is chosen in order to correspond as far as is practicable with the average uncertainty associated with the experimental data. Distances of closest approach are empirically defined using the *T(r)* derived from the HEXRD and ND data by direct Fourier transformation as far as is possible. For those pairwise correlations that are not adequately resolved it is found that an iterative approach is required, employing whatever starting values might be available in the literature (e.g. for crystalline analogues or comparable amorphous systems). Naturally, this tends to be more problematic in the case of the HEXRD data since the real-space resolution is not as favourable as it is in the context of the ND data. As a guiding principle, the largest value of the distance for closest approach consistent with obtaining approximately Gaussian correlation peaks was used; e.g. care was taken to avoid setting values that resulted in having atoms ‘pile up’ against limiting distances as the algorithm attempts to fit the model to the experimental data. The values adopted in the present study are shown in Table 6.4.

	Å
Si···Si	2.80
Si-O_b	1.45
Si-O_{nb}	1.45
Si···P	2.90
Si···Ca	3.10
Si···Na	2.90
O_b···O_b	2.10
O_b···O_{nb}	2.10
O_b···P	1.35
Ca-O_b	2.10
Na-O_b	2.20
O_{nb}···O_{nb}	2.10
P-O_{nb}	1.35
Ca-O_{nb}	2.10
Na-O_{nb}	2.20
P···P	2.70
P···Ca	2.90
P···Na	2.90
Ca···Ca	3.30
Ca···Na	3.00
Na···Na	3.50

Table 6.4: Distances of closest approach used during the RMC modelling process.

Only when the initially random box of atoms satisfied the above constraints to a satisfactory level (> 98%) was the data added as the final additional constraint. After the ratio of successful to failed moves of the atoms within the box falls to its equilibrium value, about which it will fluctuate, the model was deemed to have reached a dynamic equilibrium. At this point, assuming an overall examination of the structure is satisfactory (e.g. that the SiO_4^{2-} units assume a roughly tetrahedral shape) it becomes possible to interrogate the model in order to generate information on possible partial pairwise correlations, $T_{ij}(r)$ – i.e. those correlations consistent with the experimental data.

The ^{29}Si, ^{31}P, ^{23}Na NMR spectra are shown in Figure 6.7.

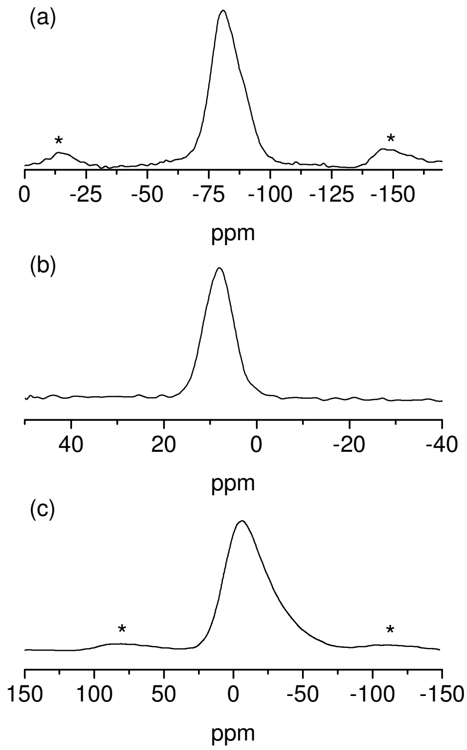

Figure 6.7: Solid state MAS NMR spectra: (a) ^{29}Si, (b) ^{31}P and (c) ^{23}Na.

The ^{29}Si spectrum exhibits one broad and asymmetric peak which can be deconvolved by Gaussian fitting into two resonance peaks centred at -88.1 and -80.4 ppm. ^{29}Si NMR spectra from oxide materials are normally discussed in terms of Q^n units, which describe the connectivity of the SiO_4 tetrahedra that make up the structure. Thus, Q^0, Q^1, Q^2, Q^3 and Q^4 units represent SiO_4 groups connected to 0, 1, 2, 3 or 4 other such groups, respectively. The two peaks observed in the ^{29}Si NMR spectrum from Bioglass® at -88.1 and -80.4 ppm are assigned to Q^3 and Q^2 units, respectively [6.10, 6.11]. The relative intensity (from Gaussian fitting) of the Q^3 and Q^2 peaks is 31% and 69%, respectively. This result therefore suggests that the silica network of the structure mostly consists of chains and rings of Q^2 SiO_4 tetrahedra with some degree of cross linking as represented by the presence of the Q^3 units.

The ^{31}P NMR spectrum consists of one broad resonance at 8.1 ppm. This can be assigned to the presence of phosphorus in an orthophosphate environment [6.10, 6.11] and thus suggests that phosphorus exists in isolated PO_4^{3-} anions in the structure, thereby removing sodium and calcium cations from a network-modifying role in the silicate network [6.10]. In fact, the chemical shift of the phosphorus resonance is midway between that of $Ca_3(PO_4)_2$ (0 ppm) and that of $Na_2(PO_4)$ (15.6 ppm) [6.12], providing evidence that the PO_4^{3-} anions are associated with the metal cations. In a molecular dynamics, MD, study [6.13] performed on Bioglass® the presence of some Q^1 species were suggested (~33%), and also some Q^2 (~2%), the Q^2 relating specifically to the presence of P-O-Si bonds. The data presented here are fitted satisfactorily without the need to include Q^1 or Q^2 species, and is in agreement with optical spectroscopic data on Bioglass® which also showed no evidence of P-O-Si bonds [6.14]. The experimental data is of course limited by its intrinsic sensitivity, and a very small fraction of Q^1 species may therefore be present – but the data would seem to rule out the ~33% postulated as a result of the MD study.

The ^{23}Na NMR spectrum exhibits one broad asymmetric resonance at -6.1 ppm. The asymmetry is due to residual second-order quadrupolar interactions which are not completely removed under MAS conditions [6.10]. Sodium ions present in different coordination environments have been correlated with distinct but overlapping solid-state ^{23}Na NMR chemical shifts or chemical shift ranges (4-coordinate sodium *ca.* – 50 ppm, 5-coordinate sodium *ca.* - 21 ppm and 6-coordinate sodium from ca. - 7.2 ppm to -3.0 ppm) for a number of compounds [6.15, 6.16]. The ^{23}Na NMR chemical shift for Bioglass® reveals that the likely sodium environment is six-coordinate in a pseudo-octahedral NaO_6 arrangement, although the presence of five-coordinate Na^+ ions cannot be completely excluded.

This direct experimental information is now utilised to produce an RMC model. In particular, the ^{29}Si NMR data was used to determine the Q speciation of the Si network. In each of the models generated, a constraint was included on the Si to ensure that the model contained 31% Q^3 units and 69% Q^2 units. Also, a constraint was added to the P in terms of its bonding to oxygen to ensure that it was present in an orthophosphate environment. These constraints were subsequently varied to examine the effect they had on the overall model. Changes to the constraints, within a reasonable limit, had little effect on the structural statistics derived from the final resultant model (i.e. after it had also been constrained by the diffraction data, see below), indicating that the model structure is itself robust against errors in the data. It also reinforces the important fact that 3-D RMC models, derived as they are from one-dimensional data, cannot be regarded as unique solutions. Due to the slightly different compositions of the two samples shown in Table 6.3, two separate models were generated initially – one for each of the powdered sample for the X-ray diffraction data and the glass rod for the neutron diffraction data.

The diffraction data and the corresponding RMC fits for each data set are shown in Figure 6.8 (*S(Q)'s*) and Figure 6.9 (*T(r)'s*).

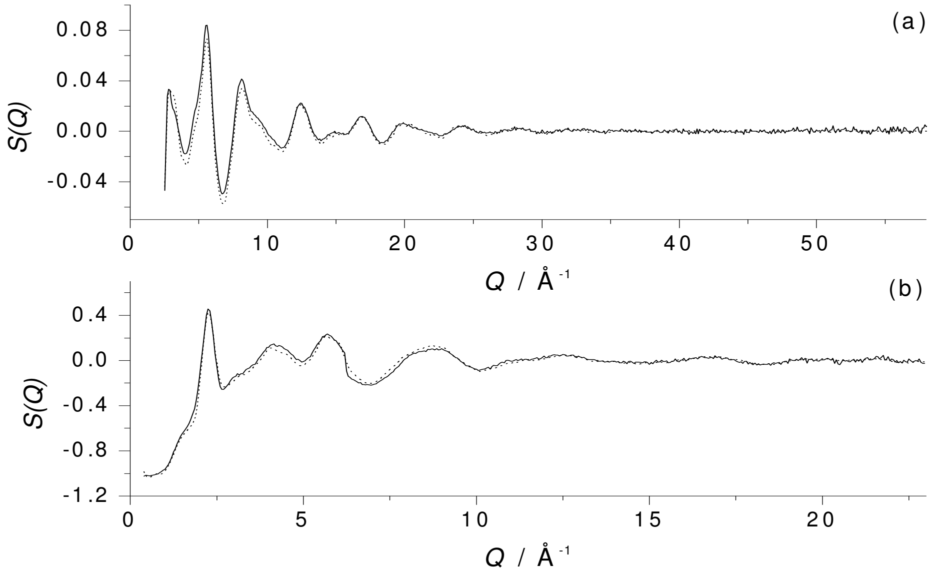

Figure 6.8: (a) Neutron diffraction data from the Bioglass® sample: Q-space structure factor *S(Q)* (solid line) together with RMC fit (dotted line); and (b) high energy X-ray diffraction data from the Bioglass® sample: Q-space structure factor *S(Q)* (solid line) together with RMC fit (dotted line).

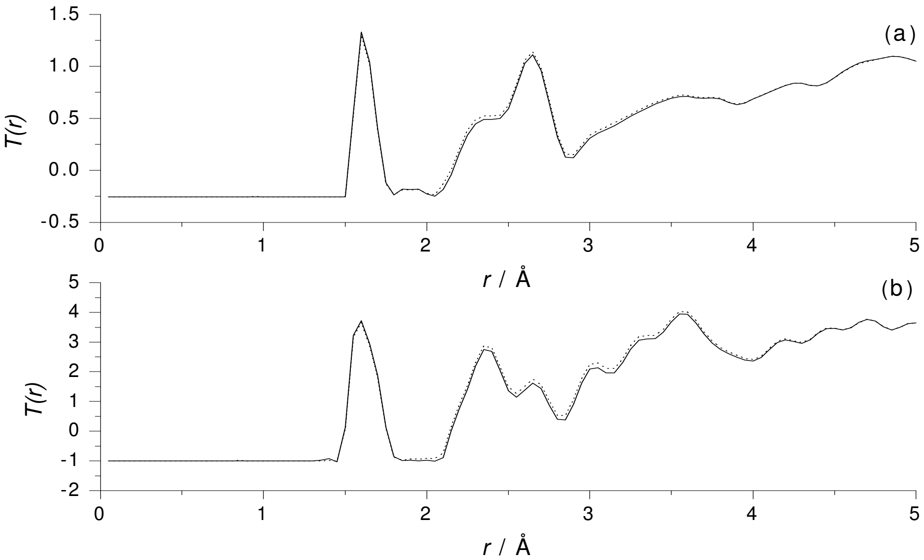

Figure 6.9: (a) Neutron diffraction data from the Bioglass® sample: pair distribution function *T(r)* (solid line) together with RMC fit (dotted line); and (b) high energy X-ray diffraction data from the Bioglass® sample – pair distribution function *T(r)* (solid line) together with RMC fit (dotted line).

After careful examination of the closely similar partial pair correlations and model structures resulting from each RMC model, it was considered appropriate to average the partial pair correlation functions, and thereafter to treat the data as coming from one combined model. In Figure 6.10, nine principal partial $T_{ij}(r)$ functions output from the RMC models are shown.

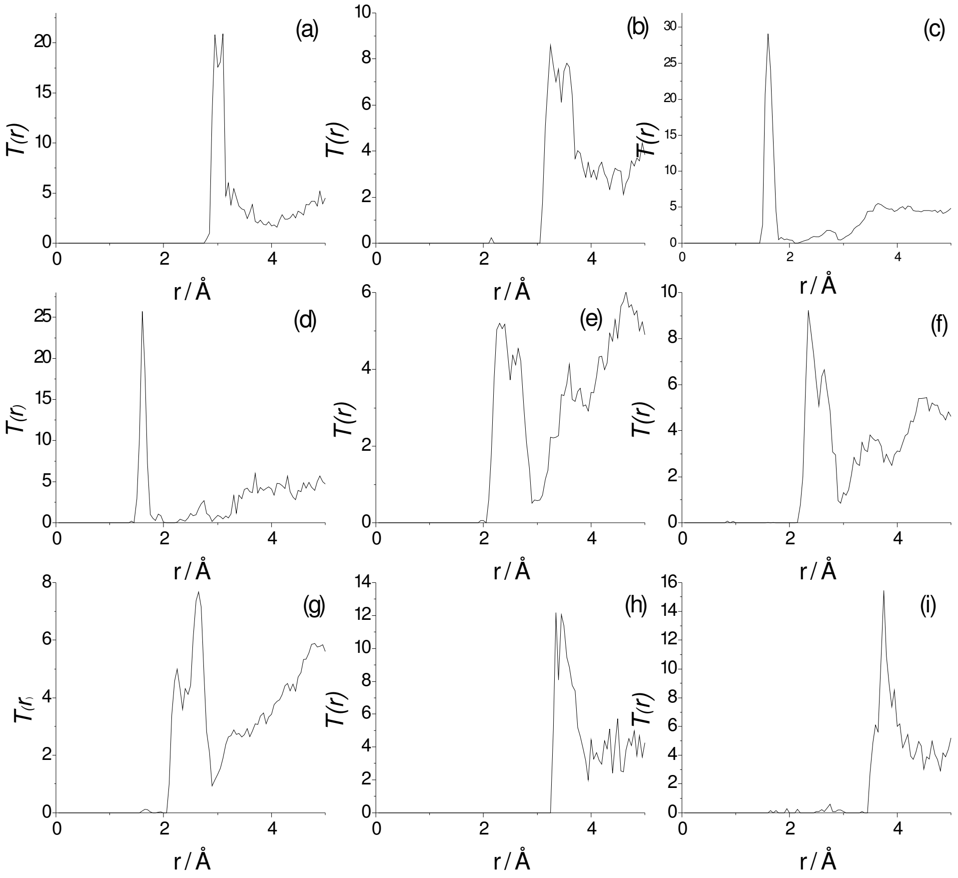

Figure 6.10: RMC partial $T_{ij}(r)$ functions, (a) Si···Si, (b) Si···Ca, (c) Si-O, (d) P-O, (e) Ca-O, (f) Na-O, (g) O···O, (h) Ca···Ca, (i) Na···Na.

The parameters obtained from the RMC model are shown in Table 6.5.

Sample	Correlation	R / Å	N	σ / Å
45S5 RMC partials	Si-O	1.61	~3.7	0.06
	Ca-O	2.31, 2.59	~4.9	0.24
	Na-O	2.35	~6.0	0.16
	O···O	2.64	~3.0	0.15
	Si···Na	2.96	~4.0	0.31
	Si···Si	3.03	~2.3	0.10
	Ca···Na	3.05	~3.6	0.16
	Si···Ca	3.25	~1.6	0.26
	Ca···Ca	3.48	~1.7	0.20
	Na···Na	3.75	~3.3	0.26
	P-O	*1.60*	*~3.9*	*0.04*
	P···P	*2.90*	*~0.2*	*0.10*
	P···Ca	*2.96*	*~2.6*	*0.59*
	P···Na	*2.97*	*~4.5*	*0.35*
	P···Si	*3.00*	*~0.3*	*0.07*

Table 6.5: Structural parameters obtained from RMC modelling; because there are relatively few P atoms in the RMC box, the parameters returned are regarded as having qualitatively less meaning. (σ is the full width half maximum of the peaks).

Due to the very small amount of phosphorous present, very little genuinely reliable information about the phosphorous environment within the glass network can be obtained from these results. Thus, one cannot place any weight on the details of the P···X correlations within the RMC model. Parameters regarding phosphorous have been included at the bottom of Table 6.5 for completeness only. (Given that the ^{31}P NMR results are consistent with orthophosphate (Q^0) units, and that the data indicates that the PO_4^{3-} anions are associated with the metal cations, one would expect to observe a P-O_{nb} bond at ~ 1.53 Å as found in $Ca_3(PO_4)_2$ [6.17] and in $Na_2(PO_4)$ [6.18]. Both of these materials exhibit one P-O_{nb} bond as long as ~1.58 Å however this does not agree with the four P-O_{nb} bonds at ~1.6 Å shown in Table 6.6. Despite the statistical limitations of our model, we nevertheless note the fact that the RMC model gave a P-O_{nb} coordination of ~3.9 and a P-O_b coordination of ~0.03. This would indicate the predominant presence of orthophosphate (Q^0) units within the model, as shown by the NMR data and explicitly incorporated into our model-building process. The associated modelled bond distance of ~1.6 Å is more usually associated with P-O_b bonds [6.4], but more probably indicates that the more dominant Si-O correlation at 1.6 Å is affecting our ability accurately to fit the relatively very weak P-O contribution)

The partial pair correlation functions derived from the RMC model place the Si-O peak at 1.61 Å with a coordination of slightly less than 4, as expected in silica based materials [6.7]. The Ca-O partial is seen to be an asymmetric feature in Figure 6.10 (e) centred at ~2.5 Å but extending from 2.05 Å to 2.90 Å with two partially resolved peaks, and a total coordination number of ~5. This is in good agreement with previous data obtained in a recent neutron diffraction with isotopic substitution experiment undertaken on an analogous bioactive calcia-silica sol-gel glass [6.2], and also with a corresponding molecular dynamics study [6.19].

The model Na-O partial pair correlation function indicates a distance of 2.35 Å, which is consistent with previous measurements [6.3], and a coordination of ~6, agrees with the ^{23}Na NMR data which indicated that the sodium environment is six-coordinate within a pseudo-octahedral NaO_6 arrangement.

The model O···O partial pair correlation is found as expected in a silica based material at 2.64 Å, with a coordination of ~3. The O-Si-O coordination number would tend towards six in a fully densified silica network, but is reduced here due to the presence of O_{nb} atoms. This would imply that the presence of Ca and Na is causing significant disruption to the base silica network.

The Si···Si, Si···Ca and Ca···Ca partial pair correlation functions derived from the RMC model give peak distances of 3.03, 3.25 and 3.48 Å respectively. The Si···Si coordination number of just above 2 agrees with the fact that Si is mostly present in Q^2 units.

Figure 6.11 shows an example of silica tetrahedra and Figure 6.12 shows a phosphorous tetrahedra from one of the RMC models after fitting to the data.

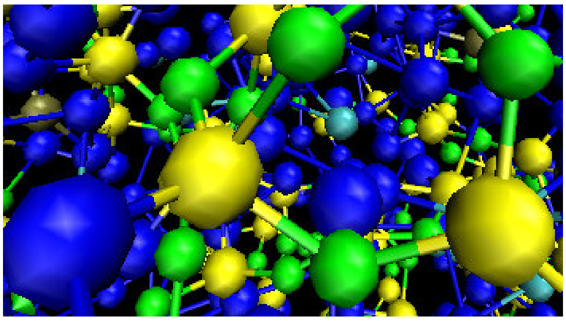

Figure 6.11: Example of Si atom (yellow) connected to three O_b atoms (green) and one O_{nb} atom (blue).

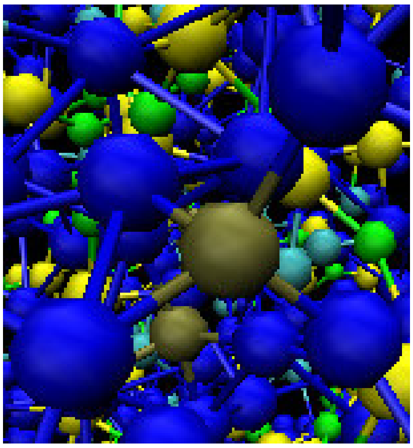

Figure 6.12: Example of phosphorous in an orthophosphate environment. P atom (brown) connected to four O_{nb} atoms (blue)

The model shows some evidence of a heterogenous distribution of calcium ion, i.e. clustering. This spatial clustering has been observed previously in an MD study [6.13]. The nearest neighbours distance of 3.48 Å obtained from the empirical RMC model, is significantly less than the Ca···Ca distance of 5.2 Å obtained by assuming a completely homogeneous (i.e. gas-like) Ca distribution. Also, the coordination expected for a homogenous distribution of ions, given by $N_{Ca\cdots Ca}(HOM) = (4/3)\pi R_c^3 \rho(Ca) - 1$, where R_c is the first minimum in the partial $T(r)$ function, $T_{Ca\cdots Ca}(r)$, and $\rho(Ca)$ is the number density of Ca in our model, predicts a Ca···Ca coordination of ~0.9, whereas the RMC model returns ~1.7. Thus, both approaches offer clear evidence for calcium clustering in Bioglass®. A comparable effect has previously been observed in analogous samples of sol-gel bioactive glasses, wherein it was suggested that clustering occurred, on the surfaces of the glass, as the concentration of Ca in the samples increased (and as a consequence influenced the acid/base properties of the bioactive glass surface) [6.20]. The results presented herein are necessarily limited to the suggestion that Ca clusters exist, *per se*; given that Bioglass® is a high-density melt-quenched glass, the question of surface segregation does not arise. Clustering does however have an immediate consequence for the observed bioactivity of the material in the sense that diffusion/dissolution pathways will be heavily influenced by the existence of connected volume elements of high Ca concentration within a modified silicate network.

Similarly, the nearest neighbour Na···Na correlation shell is determined to be centred at 3.75 Å, compared to a calculated distance of 4.3 Å if one assumes a completely homogeneous Na distribution. Likewise, the coordination number of ~3.3 derived from the RMC model may be compared with the value of ~2.9 expected for a homogeneous distribution. Thus, there is again some evidence for the possibility of sodium clustering. In the MD study of Bioglass® referred to above [6.13], it was suggested that Ca dominates the coordination of the orthophosphate groups.

6.4. Summary

The HEXRD of bioactive glasses 45S5 (Bioglass®) 55S5 60S5 and 77S5 are presented. It is shown that significant structural differences are observable in these samples as a function of composition and of preparation method. The main difference between preparation methods is that the sol-gel samples contain no Na and hence this can be seen clearly in the *T(r)* functions as a 'missing' feature at ~2.4 Å where the Na-O distance is found in the melt-quenched *T(r)*'s. The effect of increasing amounts of Ca and Na on the underlying Si network can be seen in the O-Si-O pair correlation peak coordination, as the more Ca and Na present in the sample the more disrupted the Si network is. In the 77S5 sample two P-O correlations can be seen corresponding to P-BO and P-NBO and the relevant coordination numbers indicate a majority of pyrophosphate (Q^1) units.

The X-ray diffraction *T(r)* simulation for Bioglass® can be compared with results output from RMC modelling. The data are mostly in good agreement, however the Si··Si coordination in the X-ray diffraction simulation was ~4 which one would expect to be ~2 in a glass consisting of mostly Q^2 species (as is indicated by NMR data). The RMC model reveals that the peak in the *T(r)* assigned to Si··Si actually contains contributions from Ca···Na, P···Ca, P···Na and P···Si pair correlations, which may explain the unusually high Si··Si coordination. Unfortunately using the current method it is impossible to fit all the peaks present in these multicomponent glasses, so although simulations of this X-ray diffraction data give a good insight into the structure of these materials, after a distance of ~ 3 Å, errors increase significantly due to overlapping peaks. This emphasises the need to utilise several structural characterisation techniques in order to obtain a robust structural picture of these types of material.

A model has been generated and interpreted on the basis of high energy X-ray and neutron diffraction study and multi-nucleus solid state NMR data on Bioglass®. The diffraction data, analysed using an RMC model which explicitly incorporates the results of the solid state NMR data, show a significantly disrupted silica network. The ^{29}Si NMR suggests that the host silica network primarily consists of chains and rings of Q^2 SiO_4 tetrahedra, with some degree of cross linking as represented by the presence of Q^3 units. The ^{31}P NMR indicates that phosphorus exists as isolated PO_4^{3-}

anions in the structure, which will remove sodium and calcium cations from a network-modifying role in the silicate network. However, there is a possibility that a small number of pyrophosphate units are present. The diffraction data show a broad Ca-O pair correlation at ~2.05 – 2.90 Å, with a total coordination of ~5, which is consistent with previous NDIS and MD results from an analogous bioactive calcia-silica sol-gel glass. The diffraction data suggest a Na-O distance of 2.38 Å and a corresponding coordination of ~6, which is in good agreement with previously published values; the coordination number is supported by the ^{23}Na NMR data presented here, which reveals that the likely sodium environment is six-coordinate in pseudo-octahedral NaO_6 arrangement, although there is the possibility of the presence of five-coordinate Na^+ ions. There is evidence of a non-homogeneous distribution of Na within the glass, which is important in the context of the relatively slow dissolution of the modified silica network. The data provides some evidence of Ca clustering, which is consistent with the predictions of a molecular dynamics simulation for a similar sample, and also implies the presence of CaO as the structural motif. This latter observation is of direct relevance to the understanding of the facile nature of Ca within such glasses which gives rise to its relatively rapid diffusion from the solid into solution (and therefore to its behaviour in terms of the material's overall bioactivity).

References

[6.1] Pickup, D.M., Mountjoy, G., Roberts, M.A., Wallidge, G.W., Newport, R.J., Smith, M.E., *J. Phys.: Condens. Matter.,* **12,** 3521, 2000.

[6.2] Skipper, L.J., Sowrey, F.E., Pickup, D.M., Drake, K.O., Smith, M.E., Saravanapavan, P., Hench, L.L., Newport, R.J., *J. Mater. Chem.,* **15,** 2369-2374, 2005.

[6.3] Du, J., Cormack, A.N., *J. Non. Cryst. Solids.,* **349,** 66-79, 2004.

[6.4] Hoppe, U., Walter, G., Barz, A., Stachel, D., Hannon, A.C., *J. Phys.: Condens. Matter.,* **10,** 261-270, 1998.

[6.5] Gaskell, P.H., Eckersley, M.C., Barnes, A.C., Chieux, P. *Nature*, **350**, 675, 1991.

[6.6] Mead, R.N., Mountjoy, G., *J. Phys*: *Chem. B,* **110,** 14273-14278, 2006.

[6.7] Wright, A.C.: *Experimental Techniques of Glass Science* ed C J Simmons and O H El-Bayoumi, American Ceramic Society, Westerville, 1993, p. 205-314.

[6.8] Pant, A.K., *Acta Crystallogr., Sect B: Struct. Sci*., **24,** 1077, 1968.

[6.9] Private communication, D Greenspan, Novamin Technology Inc., 13709 Progress Blvd., suite #23 Alachua, FL 32615, USA . Data to be published.

[6.10] Lockyer, M.W.G., Holland, D., Dupree, R., *J. Non-Cryst. Solids*, **351**, 173, 2005.

[6.11] Elgayar, I., Aliev, A.E., Boccaccini, A.R., Hill, R.G., *J. Non-Cryst. Solids*, **188**, 207, 1995.

[6.12] Mudrakovskii, I.L., Schmachkova, V.P., Kotsarenko, N.S., Mastikhin, V.M., *J. Phys. Chem. Solids*, **47**(4), 335-339, 1986.

[6.13] Tilocca, A., Cormack, A.N., de Leeuw, N.H., *Chem. Mater.*, **19**, 95-103, 2007.

[6.14] Cerrutti, M., Bianchi, C.L., Bonino, F., Damin, A., Perardi, A., Marterra, C., *J. Phys. Chem. B*, **109**, 14496-14505, 2005.

[6.15] Koller, H., Engelhardt, G., Kentgens, A.P.M., Sauer, J., *J. Phys. Chem.*, **98**, 1544, 1994.

[6.16] Stebbins, J.F., Xue, X.Y., *Physics and Chemistry of Minerals,* **20**, 297-307, 1993.

[6.17] Yashima, M., Sakai, A., Kamiyama, T., Hoshikawa, A., *J. Solid State Chem.,* **175**, 272-277, 2003.

[6.18] Harrison, R.J., Putnis, A., Kockelmann, W., *Phys. Chem. Chem. Phys.,* **4**, 3252-3259, 2002.

[6.19] Mead, R.N., Mountjoy, G., *Chem. Mater.,* **18**, 3956-3964, 2006.

[6.20] Cerruti, M., Bolis, V., Magnacca, G., Morterra, C., *Phys. Chem. Chem. Phys.,* **6,** 2468-2479, 2004.

Chapter 7

Reaction mechanisms of Bioglass®

7.1 Introduction

In this chapter the reaction mechanisms of Bioglass® are investigated using grazing incidence X-ray diffraction (GIXRD) and high-energy X-ray diffraction (HEXRD). GIXRD is used to observe the growth of, and identify the calcium phosphate layer on the surface of three compositions of melt-quenched bioactive glass, 45S5 (Bioglass®), 52S5 and 55S5 (again where S denotes the network former SiO_2, e.g. 45 mol% for 45S5 followed by the specific Ca/P molar ratio of 5), when immersed in tris buffer solution (TBS, a standard cell culture medium). The HEXRD data is used to compare the reaction mechanisms of Bioglass® immersed in TBS to those immersed in simulated body fluid (SBF, a simulated physiological fluid).

7.2 Grazing Incidence X-ray diffraction

TBS has been used in the earliest studies on Bioglass® [7.1-7.3], and also in more recent studies [7.4]. It is used in this study because SBF has a high concentration of Ca, P and other ions that could easily precipitate in the presence of just a few nucleation sites, whereas TBS contains no such ions and one therefore observes only the processes involving the ions available from Bioglass® itself, or the other compositions of bioactive glass [7.5].

Glass samples were provided as discs roughly 20 mm in diameter and 4.5 mm thick, by Novamin Technology Inc, Alachua Florida. The samples were dry-polished using polishing plates of 68, 36 and 12 microns, and then polished using diamond grit down to 0.5 microns. After each stage, the sample was examined under the microscope before proceeding to the next step. This process ensured an optically flat surface suitable for X-ray diffraction at shallow angles of incidence.

For the reactions, 200 ml of TBS was placed in a beaker and pre-heated to 37 °C. The sample was submerged, polished face up, in the beaker, which was covered with parafilm and placed in an oven at 37 °C. Glass samples were reacted for either 1 hour or 24 hours. The method used for TBS preparation can be found in Appendix 4.

Using a Philips *X'Pert* diffractometer with a wavelength derived from the Cu Kα line (1.5405 Å), X-ray diffraction measurements were undertaken at a shallow angle of incidence. With the sample aligned correctly, the diffraction patterns obtained are biased towards the surface of the samples, although with some bulk scattering contributing an underlying diffraction pattern. (Note that one would have to be at an angle of incidence less than the critical angle for total external reflection in order to ensure that the observed diffraction was truly confined towards the surface layer itself [7.6]). As the depth of penetration of the X-rays is not known, and neither are the details of density and composition in the near-surface regions, quantitative analysis of these results cannot be performed. However, a reliable interpretation of the growing crystalline phase on the surface can nevertheless be achieved.

In previous data recorded by Dr Valentin Craciun on a disc of 45S5 glass placed in water overnight, sharp peaks were observed in the θ: 2θ scan, as well as the GIXRD scans, with $\omega = 0.5$ ° and 3.0 °, shown in Figure 7.1. His sample was however polished using water as a lubricant, and then put in an oven at 37 °C to dry before being placed to soak in water overnight. In the present work, another sample of Bioglass® was placed in water overnight (for ~18 hours) in order to try to reproduce the previous data.

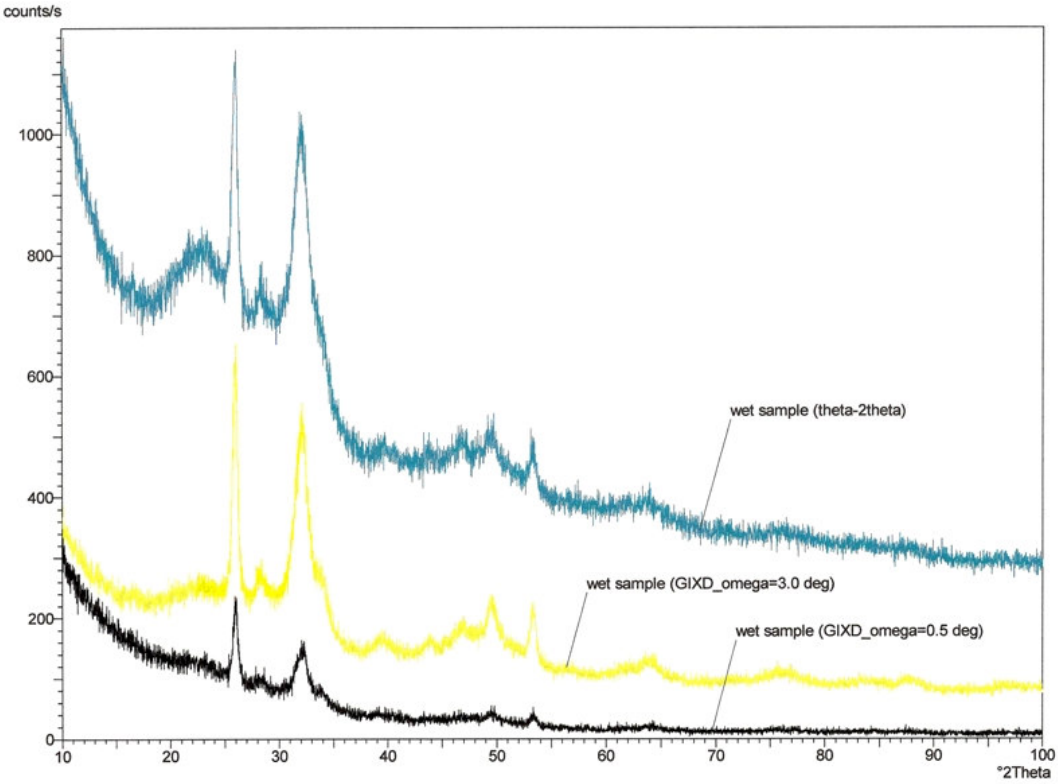

Figure 7.1: Dr Valentin Cruicin data for 45S5 in water overnight (after prior wet-polishing)

A sample of 45S5 was dry-polished, left in water for ~18 hours, then GIXRD data was collected using ω=1.0 °. The results are shown in Figure 7.2. Although this cannot be directly compared to the data taken by Valentin, since the ω value adopted is not the same, one would nevertheless expect to observe qualitatively similar results. It does however appear that the way the sample is polished (i.e. wet or dry) has an effect on the overall reaction of the glass, as no evidence of any Bragg peaks are observed in Figure 7.2. Therefore, all other samples examined in this project were polished dry so as to eliminate any effect that wet-polishing may have on the overall reactions taking place.

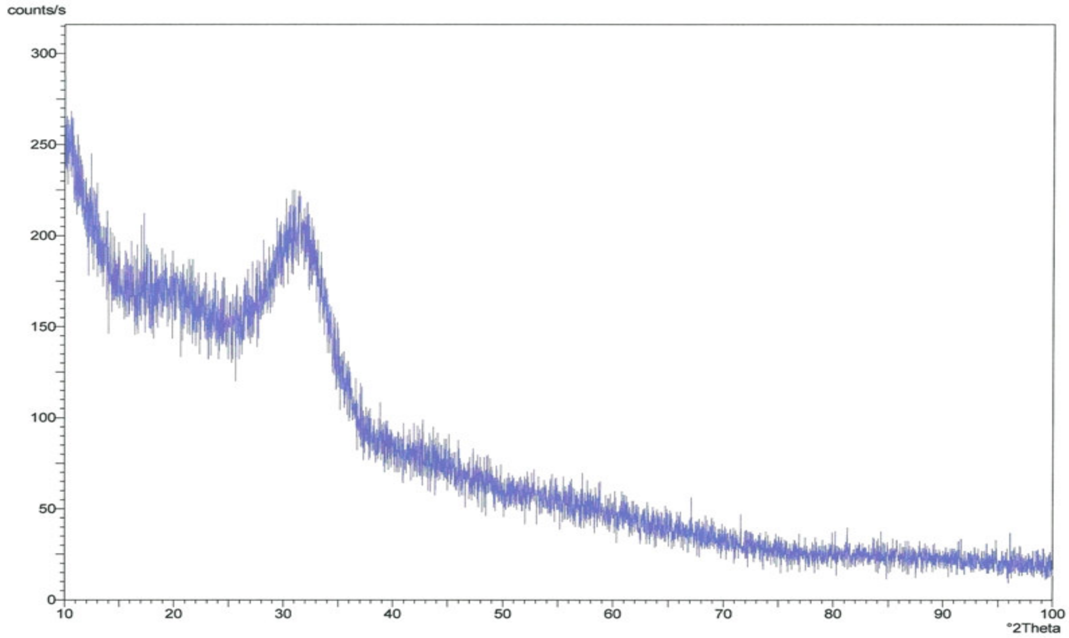

Figure 7.2: 45S5 sample in water overnight after dry-polishing (ω=1°).

Figure 7.3 shows a comparison of three compositions of unreacted, dry-polished, bioactive glass. The (unmodified) surface structures are very similar to one another, although with slightly different intensities associated with the two main diffuse features observed at angles between 10 and 30 °. The structure of the glass surface is evidently, at all compositions, amorphous.

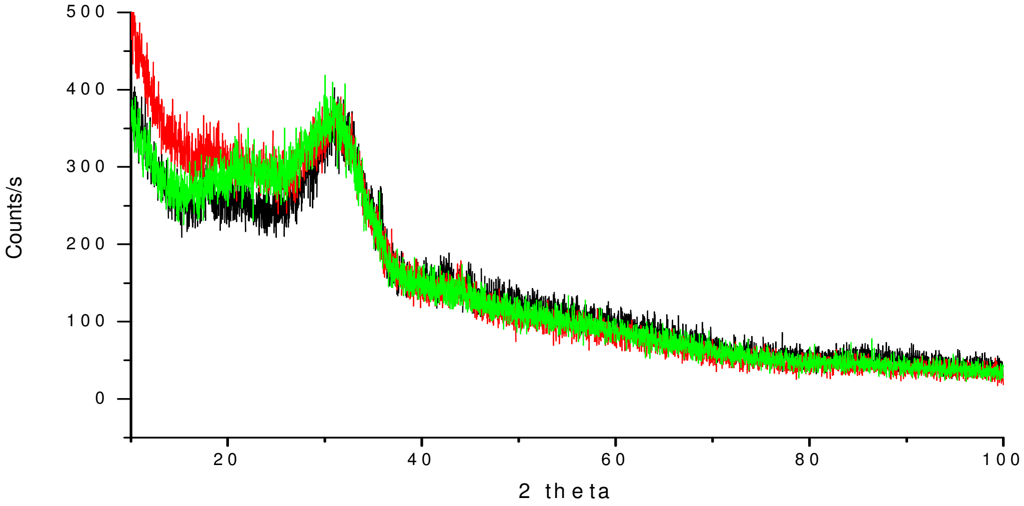

Figure 7.3: Comparison of compositions: 45S5 (black line), 52S5 (red line) and 55S5 (green line). (ω=1 ° for all samples)

Figure 7.4 shows the corresponding data for the 45S5 sample before and after reaction with TBS at 37 ºC for both 1 hour and 24 hours. The data show that after 1 hour, the relative amplitude of the diffuse scattering features has altered and thus structural changes are occurring on the glass surface, but the surface is still amorphous; there is no evidence of crystallisation. After 24 hours in TBS however, significant structural changes are occurring on the surface and a crystalline phase is evident.

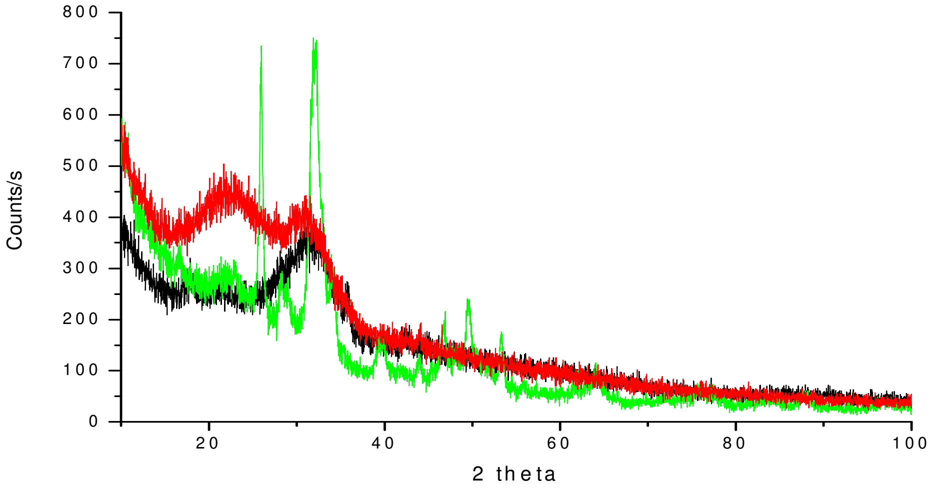

Figure 7.4: Data for 45S5 Bioglass sample: unreacted (black line), 1 hour immersion in TBS (red line) and 24 hours immersion in TBS (green line). (ω=1 ° for all samples).

Figure 7.5 shows the data for the 52S5 composition of bioactive glass. As above, the unreacted scan is shown along with that taken on the glass after 1 hour immersion in TBS and after 24 hours in TBS. Similarly to the 45S5 composition, after 1 hour the surface is still amorphous, and after 24 hours in TBS the surface is highly crystalline.

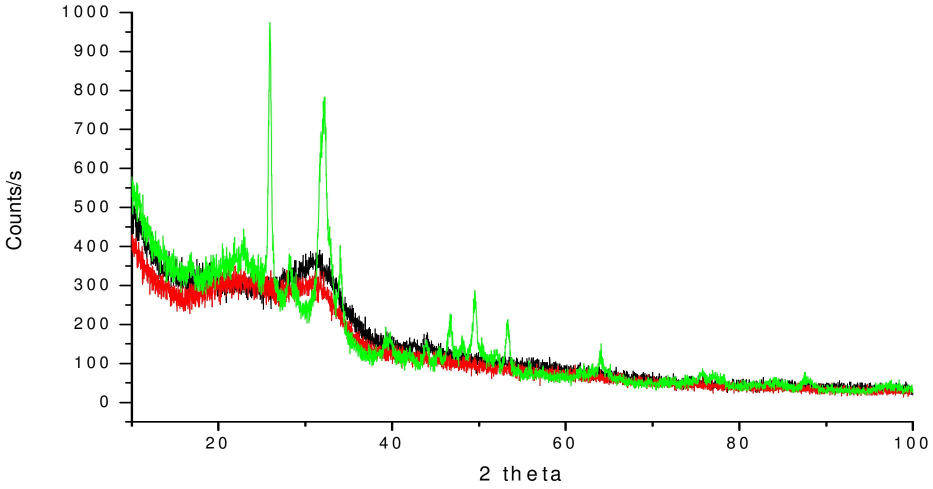

Figure 7.5: Data for 52S5 bioactive glass sample: unreacted (black line), 1 hour immersion in TBS (red line) and 24 hours immersion in TBS (green line). (ω=1 ° for all samples).

Figure 7.6 shows the data for the 55S5 composition of bioactive glass. After 1 hour it is evident that some structural changes have occurred, but the surface is still amorphous. However, in this case the 24-hour scan exhibits only a subset of the Bragg peaks occurring in the previous two samples; the bulk of the material (i.e. the substrate) is still amorphous but the surface is beginning to crystallise. This gradation in activity is perhaps to be expected given that this composition is the least bioactive of the three compositions examined.

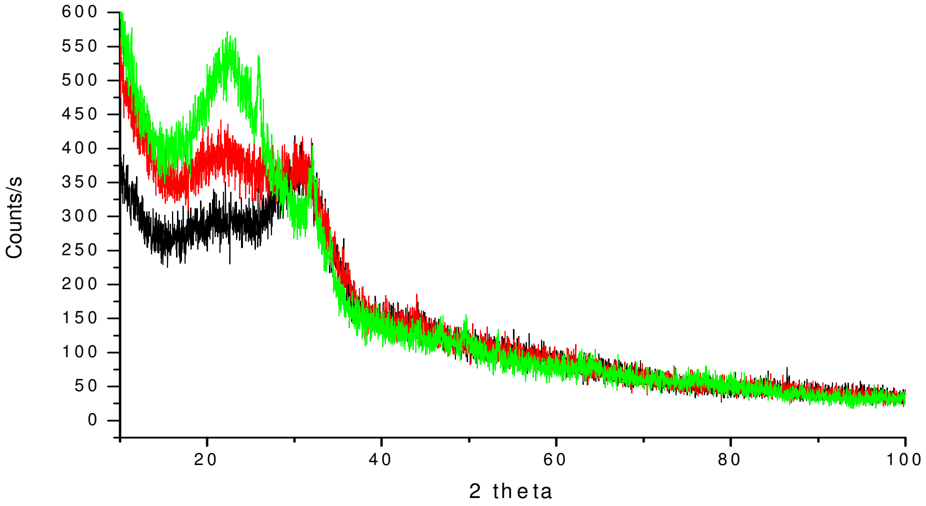

Figure 7.6: Data for the 55S5 bioactive glass sample: unreacted (black line), 1 hour immersion in TBS (red line) and 24 hours immersion in TBS (green line). (ω=1 ° for all samples).

Figures (7.7-7.9) show the 45S5 glass immersed in TBS for 24 hours along with diffraction data for three types of calcium phosphate, namely tricalcium phosphate [7.7], octacalcium phosphate [7.8] and hydroxyapatite [7.9]. Although the diffraction data for the three calcium phosphates is very similar, the peak positions and intensities clearly show that the crystalline phase on the surface of the 45S5 Bioglass® is hydroxyapatite.

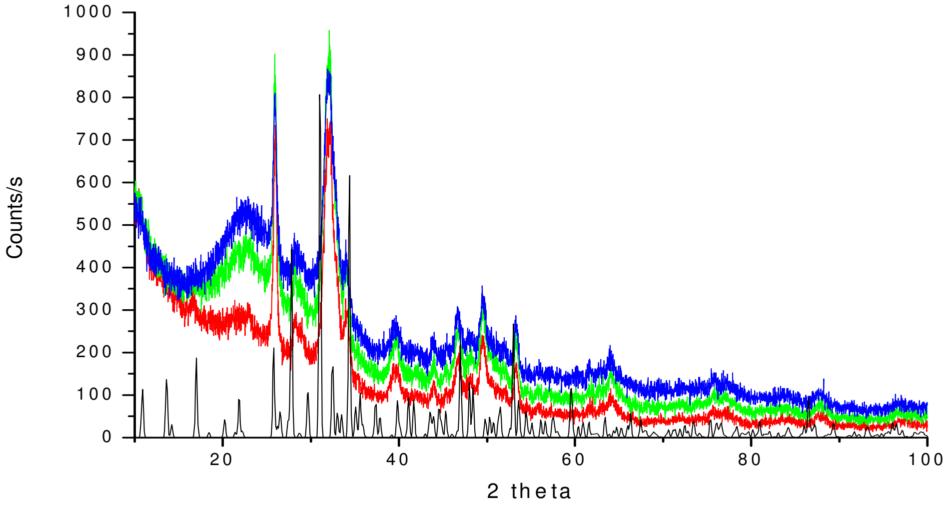

Figure 7.7: 45S5 24 hours in TBS data: ω=1 ° (red line), ω=2 ° (green line), ω=4 ° (blue line) compared to diffraction data for tricalcium phosphate (black line).

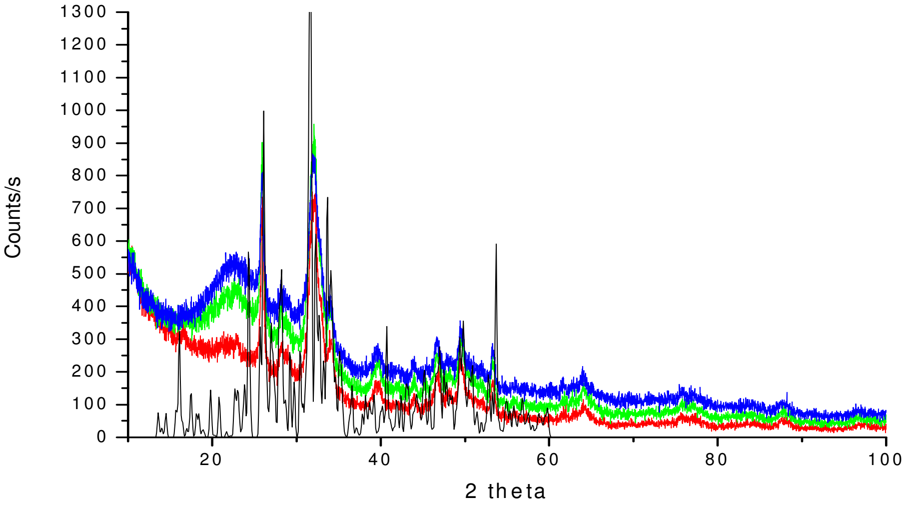

Figure 7.8: 45S5 24 hours in TBS data: ω=1 ° (red line), ω=2 ° (green line), ω=4 ° (blue line) compared to diffraction data for octacalcium phosphate (black line).

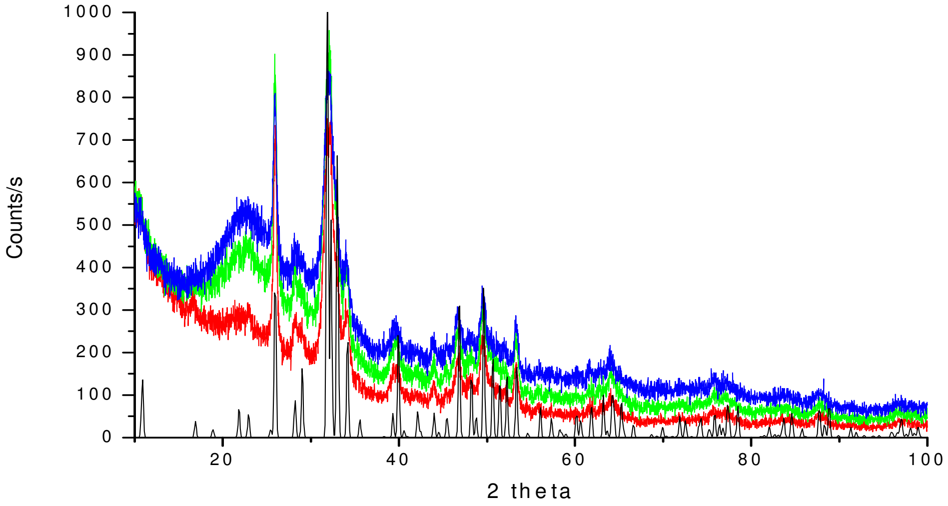

Figure 7.9: 45S5 24 hours in TBS data: ω=1 ° (red line), ω=2 ° (green line), ω=4 ° (blue line) compared to diffraction data for hydroxyapatite (black line).

In Figure 7.10 we show the 52S5 bioactive glass immersed in TBS for 24 hours along with the diffraction data from hydroxyapatite. It is apparent that for this composition of glass also, the crystalline phase growing on the surface is hydroxyapatite. In Figure 7.11 we show the 55S5 bioactive glass immersed in TBS for 24 hours along with the diffraction data from hydroxyapatite. In this case, although the crystalline phase beginning to grow on the surface does show a correlation with the diffraction pattern of hydroxyapatite, the evidence is less clear.

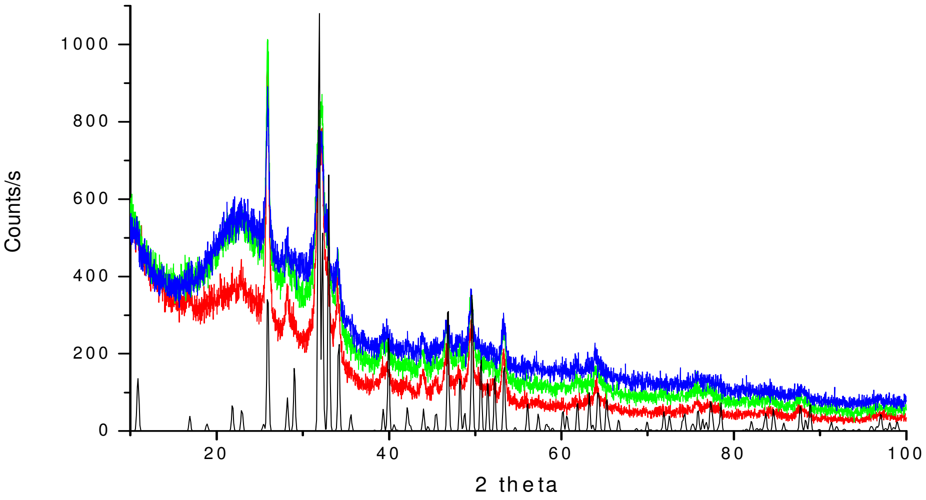

Figure 7.10: 52S5 24 hours in TBS data: ω=1 ° (red line), ω=2 ° (green line), ω=4 ° (blue line) compared to diffraction data for hydroxyapatite (black line).

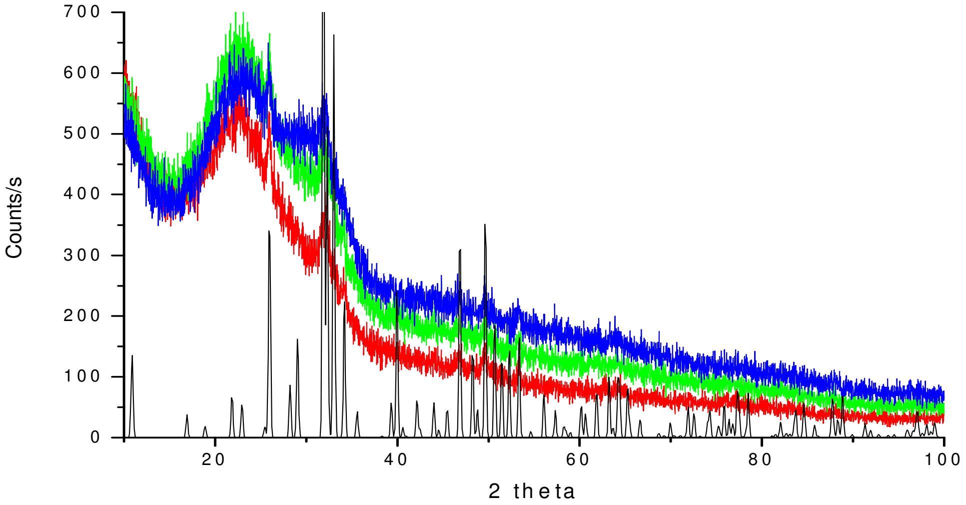

Figure 7.11: 55S5 24 hours in TBS data: ω=1 ° (red line), ω=2 ° (green line), ω=4 ° (blue line) compared to diffraction data for hydroxyapatite (black line).

The results shown above indicate that for the 45S5 Bioglass® and the 52S5 bioactive glass, crystalline hydroxyapatite has formed on the surface of the glasses after 24 hours immersion in TBS. These results agree with several sets of previously published data (however using SBF not TBS). For example, Kontonasaki *et al.* [7.10] examined hydroxycarbonate apatite (HCA) formation on particulate Bioglass® (Perioglass®). Using Fourier Transform Infrared Spectroscopy (FTIR) and Scanning Electron Microscopy (SEM) with associated Energy Dispersive Spectroscopy (EDS), they investigated Perioglass® powder with particle size 20-63μm that had been immersed in simulated body fluid (SBF) for 12, 18, 24 and 48 hours. They concluded that after 12 hours in the SBF, an amorphous $CaO-P_2O_5$ -rich layer had formed on the surface of the glass. Also, the results revealed that after 24 hours in SBF, a well-defined crystalline HCA layer had formed on the surface. The results shown in this GIXRD study agree well with those of Kontonasaki *et al.* in that we have shown that, after 24 hours immersion in tris buffer solution (TBS), a crystalline layer of hydroxyapatite has formed on the surface of both 45S5 Bioglass® and 52S5 bioactive glass. The results from the samples reacted in TBS for 1 hour show a definite change in the amorphous surface, which could be the beginnings of the growth of an amorphous $CaO-P_2O_5$ -rich layer (although there is no direct evidence for this in these samples).

Another set of experiments of interest are those carried out by Skipper *et al.* [7.11-7.13] on calcia-silica sol-gel derived bioactive glasses use techniques such as extended X-ray absorption fine structure (EXAFS), X-ray absorption near edge structure (XANES), high energy X-ray powder diffraction (XRD), neutron diffraction and magic angle spinning nuclear magnetic resonance (MAS NMR) to investigate the structural changes in the sol-gel glasses as a function of time immersed in SBF. In the paper regarding EXAFS, XANES and XRD [7.11], the results show the presence of an amorphous calcium phosphate after only 1 hour in SBF, which crystallises as hydroxyapatite once samples are annealed to 650°C. In the paper regarding XRD and solid state NMR [7.12], the results significantly extend the previous work by revealing the formation of a hydroxyapatite-like layer on the glass after exposure to SBF, which XRD confirms is amorphous overall (although the NMR data indicates some local chemical ordering, and indicates that as early as 30 minutes exposure to SBF, the presence of a calcium phosphate is observed). Again, the samples had to be annealed at 650 °C to confirm the presence of hydroxyapatite. In the final paper [7.13], dealing with high energy X-ray diffraction (HEXRD), the results indicated the growth of crystallites within the sample at only 1 hour exposure time to SBF. At 5 hours exposure time, these peaks appear stronger and are attributed to the presence of calcium phosphate; specifically, certain peaks in the 1 hour and 5 hour samples are associated with octacalcium phosphate rather than with hydroxyapatite *per se*. After 25 hours exposure time to SBF the appearance of a poorly crystalline hydroxyapatite layer is evident. Even after 72 hours in SBF, the samples had to be annealed at 650°C in order to reveal the presence of clearly defined Bragg diffraction peaks associated with polycrystalline hydroxyapatite.

Returning to the 45S5 and 52S5 samples, data shows that the hydroxyapatite layer may be growing with preferred orientation. Figures 7.12 and 7.13 show the data plotted against scaled hydroxyapatite, and the data shows that for both samples the peak assigned to the (*002*) reflection is highly developed compared to other peaks, indicating the hydroxyapatite layer has preferred orientation in the (*00l*) plane.

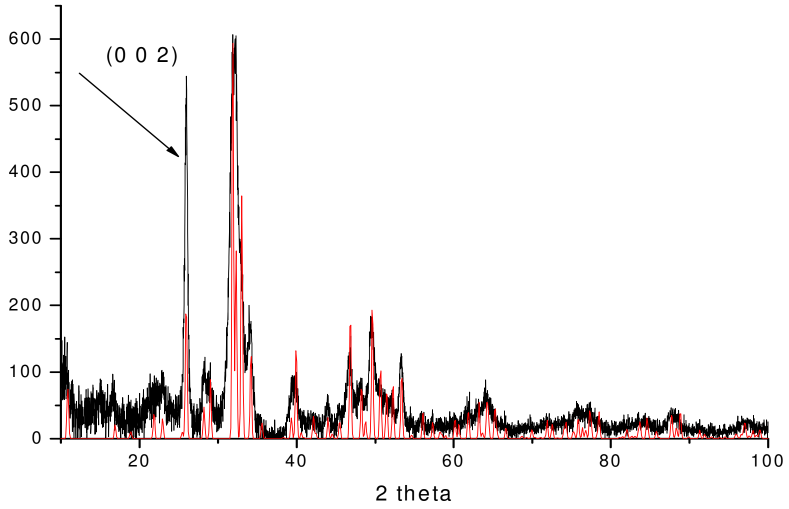

Figure 7.12: Graph showing the preferred orientation of hydroxyapatite growing on 45S5 after 24 hours in TBS. 45S5 24 hours in TBS with background subtracted (black line) and scaled hydroxyapatite (red line).

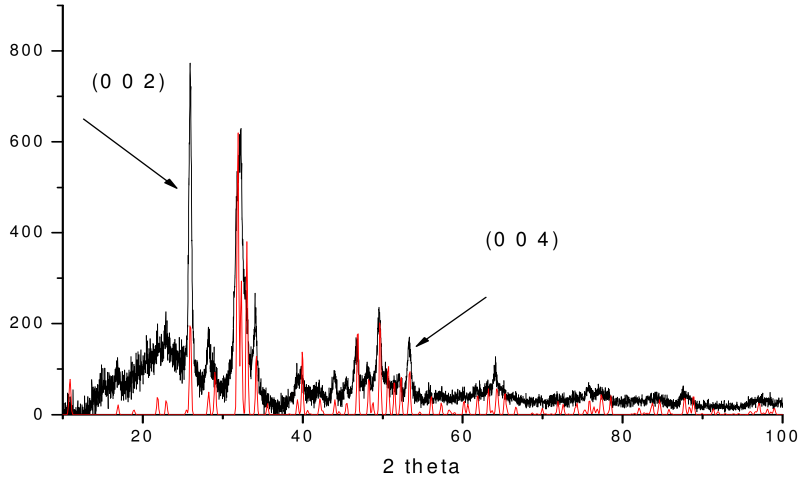

Figure 7.13: Graph showing the preferred orientation of hydroxyapatite growing on 52S5 after 24 hours in TBS. 52S5 24 hours in TBS with background subtracted (black line) and scaled hydroxyapatite (red line).

This has been observed previously by Rehman *et al.* [7.14] when observing the growth of apatite layers on Bioglass® when reacted in SBF for 7, 14 and 30 days. The paper shows that after 7 days immersion time in SBF, hydroxyapatite was observed to be growing on the surface of the glass with preferred orientation in the (*00l*) plane. Our data have shown that this occurs as early as 24 hours immersion time, in TBS. The paper indicated that this preferred orientation effect becomes reduced with time.

7.3 High Energy X-ray diffraction

The experiment carried out by Skipper *et al.* [7.13] is now performed on Bioglass®, using both SBF and TBS in order to compare the reaction mechanisms of Bioglass® with a calcia-silica sol-gel bioactive glass and also to observe any differences between the reactions carried out in TBS to those carried out in SBF.

Samples of Bioglass® powder were provided by Novamin Technology Inc, Alachua Florida. Samples were finely ground, and reacted in SBF or TBS (SBF and TBS preparation methods are described in Appendix 4). 50 ml of SBF or TBS was heated to 37 ºC in a beaker and allowed to reach thermal equilibrium, after which 75 mg of finely ground powder was added, with constant stirring, for times of 1, 2 and 10 hours, 2, 6 and 7 days. After each time period, each solution was filtered, rinsed briefly with deionised water and then acetone. The reacted powders were then dried in an oven at 100 ºC overnight.

The high energy X-ray diffraction (HEXRD) data were collected on Station 9.1 at the synchrotron radiation source (SRS), Daresbury Laboratory, UK. The finely powdered samples were enclosed inside a 0.5 mm thick circular metal annulus by kapton windows and mounted onto a flat-plate instrumental set-up. For the samples reacted in SBF the wavelength was set at $\lambda = 0.4875$ Å, and calibrated using the K-edge of a Ag foil; this value was low enough to provide data to a high value of momentum transfer ($Q_{\max} = 4\pi sin\theta/\lambda$ ~23 $Å^{-1}$). For the samples reacted in TBS the wavelength was set at $\lambda = 0.5090$ Å, and calibrated using the K-edge of a Pd foil; this value was low enough to provide data to a high value of momentum transfer ($Q_{\max} = 4\pi sin\theta/\lambda$ ~21 $Å^{-1}$). The data were corrected using the collection of programs described in Chapter 4. X-ray fluorescence analysis was carried out on all samples to allow analysis of the high-energy X-ray diffraction. Figure 7.14 shows the XRF results for all samples.

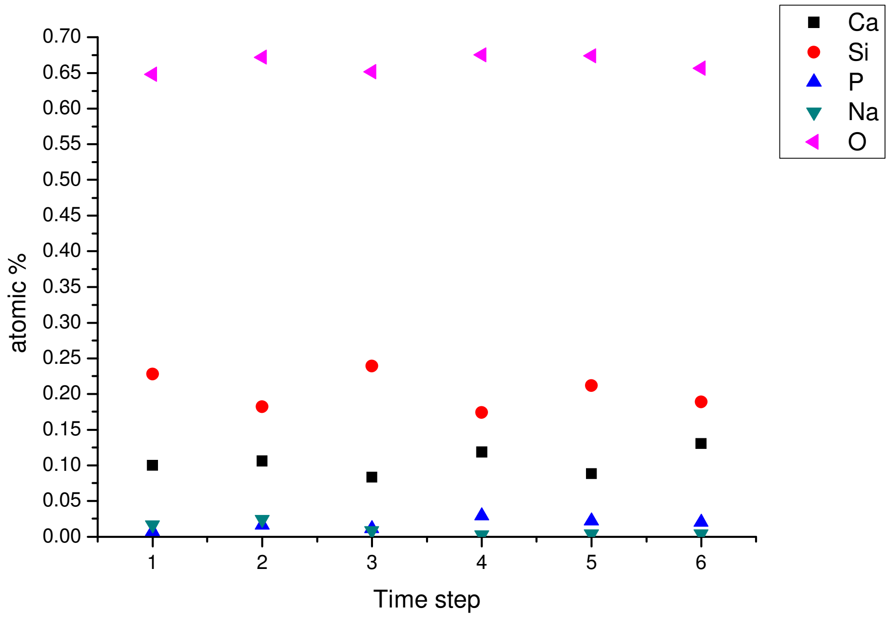

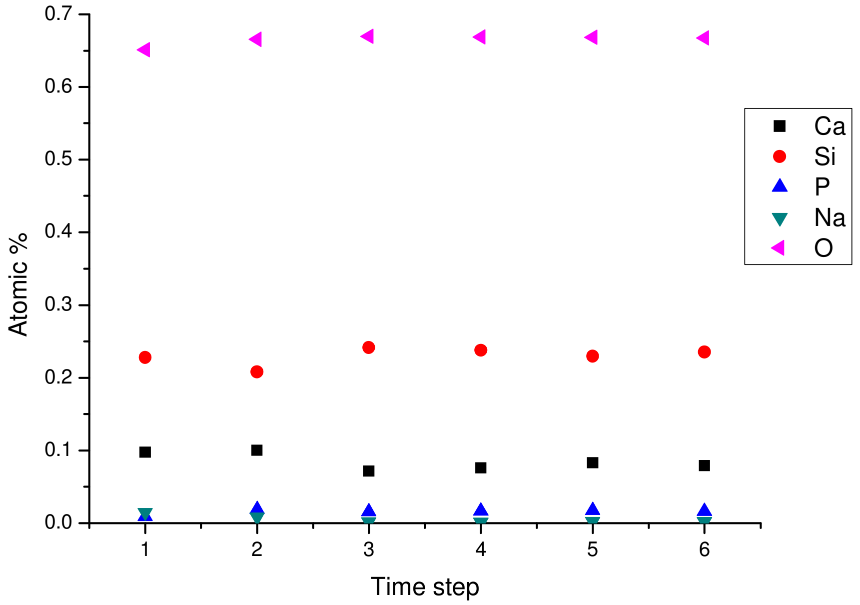

Figure 7.14: Graphs to show the sample characterisation on the basis of XRF, (using charge balancing to determine oxygen concentrations), for samples reacted with SBF (top graph) and TBS (bottom graph).

From the XRF results one can see that these samples are not behaving the same in the two solutions (one a simulated physiological fluid, the other a standard cell culture medium). Both samples appear to be behaving as expected, with calcium, phosphorus and silicon content fluctuating as the reactions take place, and the sodium content decreasing as reaction time increases, however, these fluctuations do not appear to be happening at the same rate.

Figure 7.15 and 7.16 show the high energy X-ray diffraction *S(Q)*'s and *T(r)*'s respectively for the samples of Bioglass® reacted in SBF.

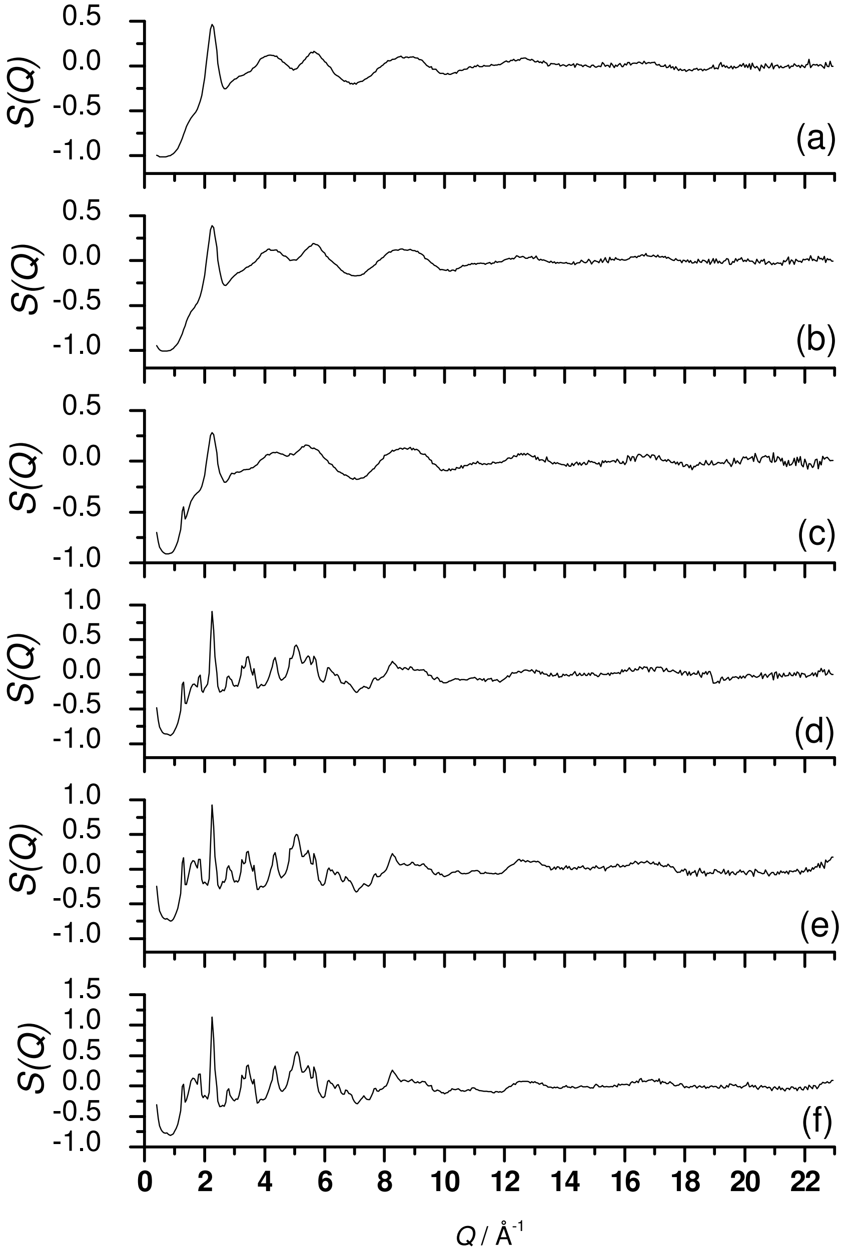

Figure 7.15: High energy X-ray diffraction *Q*-space data (*S(Q)*'s): (a) 1 hour, (b) 2 hours, (c) 10 hours, (d) 2 days, (e) 6 days, (f) 7 days, immersion time in SBF.

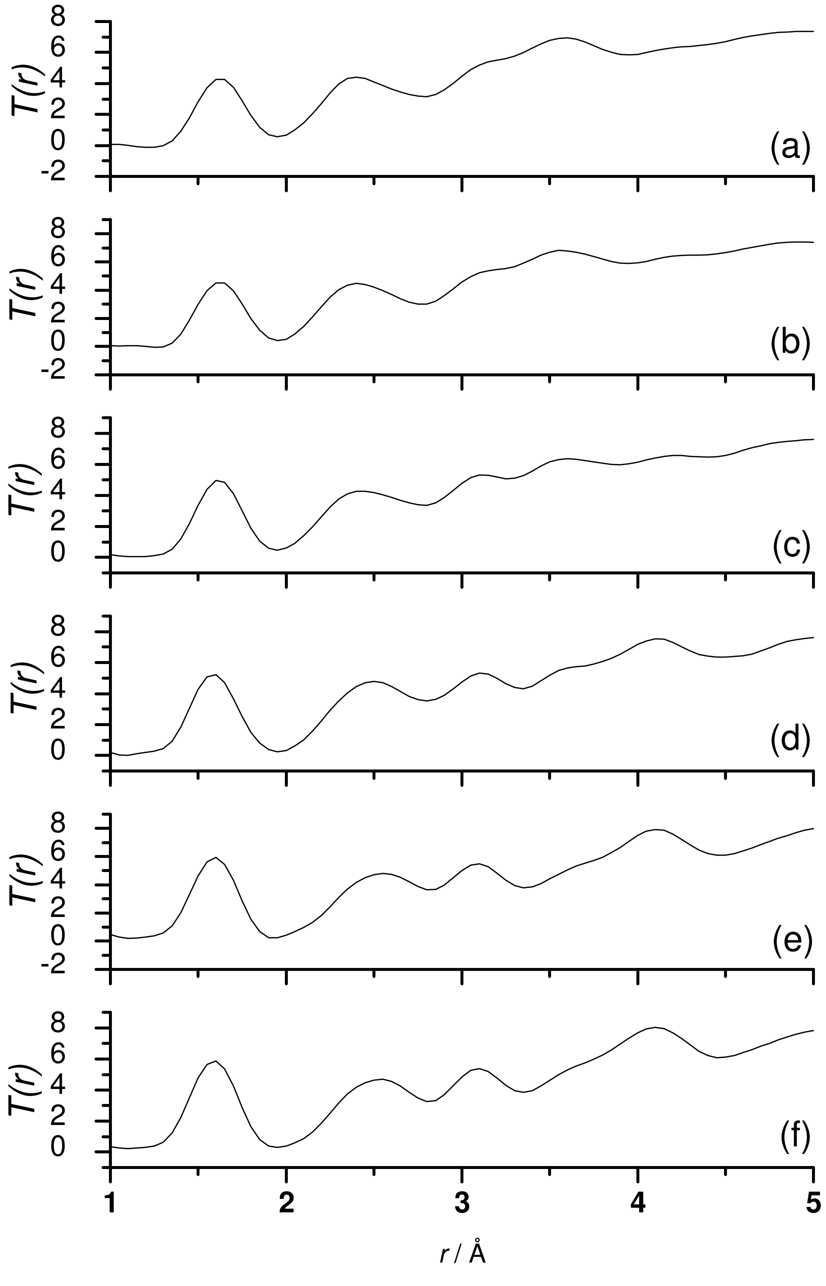

Figure 7.16: High energy X-ray diffraction *r*-space data (*T(r)*'s): (a) 1 hour, (b) 2 hours, (c) 10 hours, (d) 2 days, (e) 6 days, (f) 7 days, immersion time in SBF

Figure 7.17 and 7.18 show the high energy X-ray diffraction *S(Q)*'s and *T(r)*'s respectively for the samples reacted in TBS.

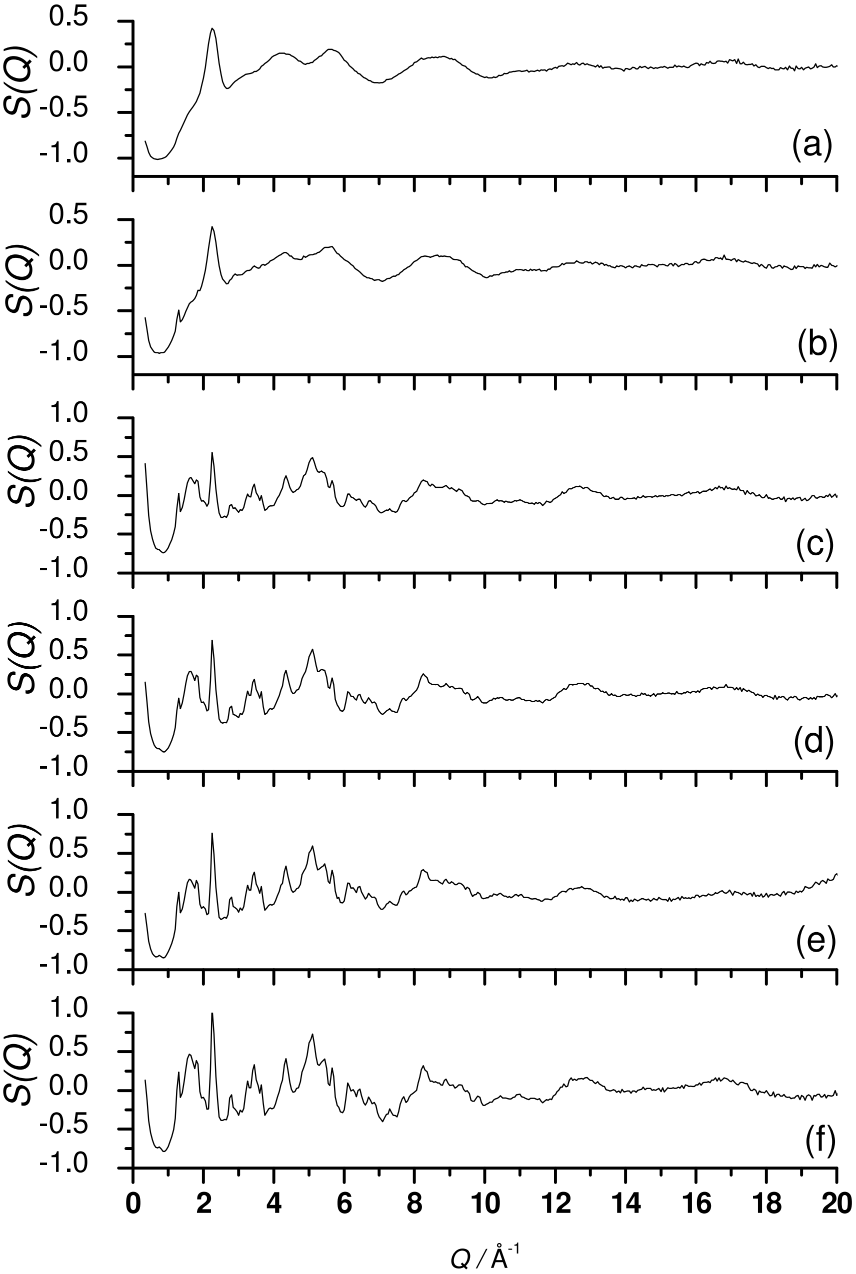

Figure 7.17: High energy X-ray diffraction *Q*-space data (*S(Q)*'s): (a) 1 hour, (b) 2 hours, (c) 10 hours, (d) 2 days, (e) 6 days, (f) 7 days, immersion time in TBS.

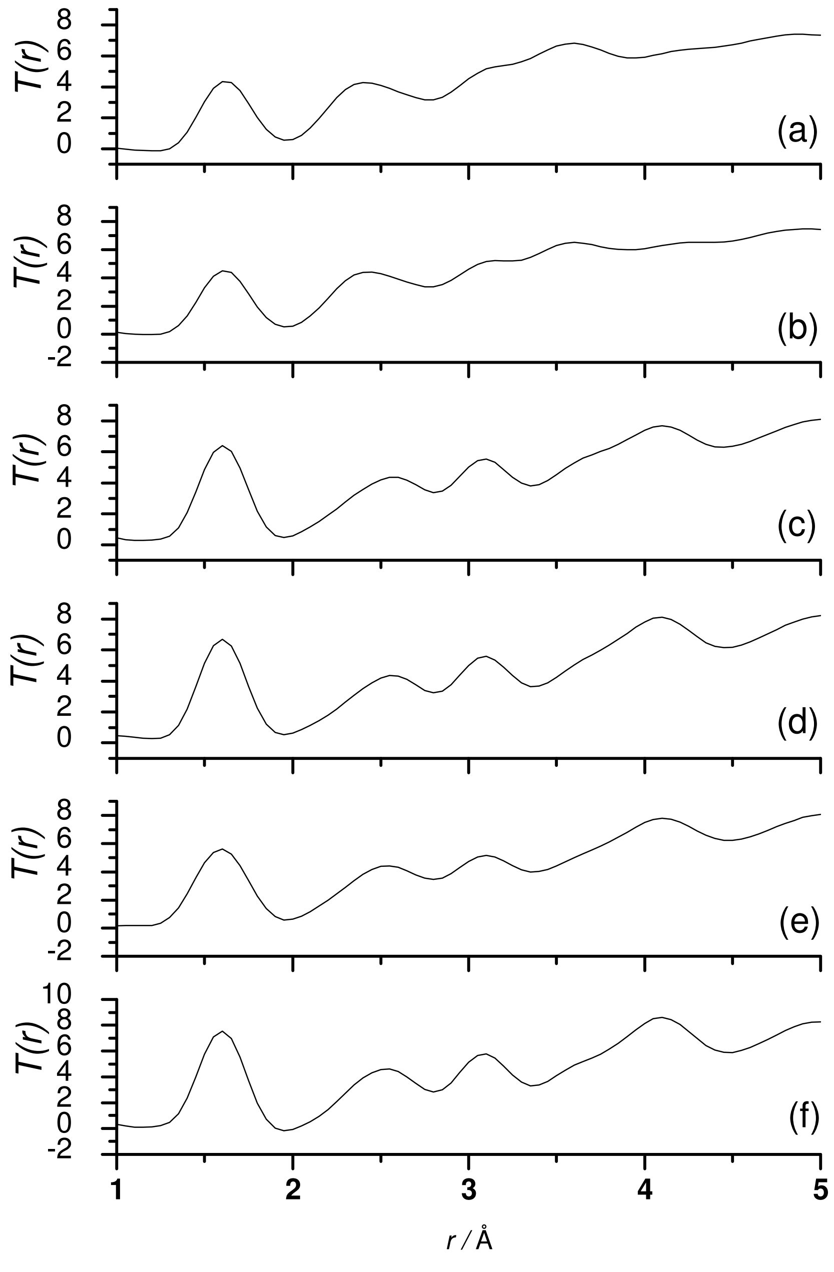

Figure 7.18: High energy X-ray diffraction *r*-space data (*T(r)*'s): (a) 1 hour, (b) 2 hours, (c) 10 hours, (d) 2 days, (e) 6 days, (f) 7 days, immersion time in TBS.

Figures 7.15-7.18 show significant differences between the reaction in SBF compared to the reaction in TBS. In the *S(Q)* data for each, the data shows that the glass sample begins amorphous, and then as reaction time increases a crystalline phase begins to appear. This can be seen after 2 days in the Bioglass® sample immersed in SBF, however this occurs earlier for the Bioglass® sample immersed in TBS, at 10 hours. As SBF contains Ca and P ions, one would expect that the growth of the calcium phosphate layer upon the silica rich layer would occur faster for the Bioglass® sample immersed in SBF, however the data seems to contradict this. It may be the case that the reaction is occurring more slowly in TBS, as expected, and the reason the crystalline phase is observed earlier in the TBS solution is because the reaction is slower, therefore larger crystals are forming (albeit of lower total volume), hence the early observation of Bragg peaks in the X-ray data. The slower a crystal is formed, the larger they can become, so in the *Q-space* data the crystalline phase is observed earlier for the sample reacted in TBS. By 7 days of immersion time in each solution, the two samples appear to be at the same stage in the reaction process, with both samples showing very similar *S(Q)*'s.

The main change observed in the *r-space* data is in the peak centred on ~3.1 Å, which corresponds to Si···Si, P···Ca, P···Si and Si···Ca bond distances (see Chapter 6). In the TBS reaction, this peak becomes more defined after 10 hours of reaction time, whereas in the SBF reaction the peak becomes more prominent after 2 days reaction time. Also the peak centred on ~2.4 Å appears to shift to longer *r* (to ~2.6 Å) after 10 hours in the TBS reaction and after 2 days in the SBF reaction. This may be due to the leaching of Na ions into the TBS/SBF, as the Na-O correlation is found at ~2.4 Å. If the Na ions are being leached out, as is shown in the XRF data in Figure

7.14, the peak at 2.4 Å will decrease in area. In the *T(r)*'s, as in the *S(Q)*'s, the samples appear to be at the same stage of the reaction process after 7 days reaction time.

When comparing the data from the Bioglass® samples to that obtained on calcia-silica sol-gel bioactive glass studied by Skipper *et al.* some similarities can be observed. Firstly, the obvious differences between the samples are the absence of Na in the sol-gel samples, and also Skipper *et al.* observed a peak in the *r-space* data at 2.02 Å which was assigned to second neighbour O···H bond lengths found in hydrated calcium phosphates, which is not visible in the data presented on the Bioglass® samples reacted in either SBF or TBS. The similarities between the two types of glass are the peak at ~2.6 Å and also the peak at ~3.1 Å becoming more prominent as the reaction time increases.

7.4 Summary

The GIXRD data confirm the growth of hydroxyapatite on the surface of Bioglass® when immersed in TBS for 24 hours. The data indicate that in this 24 hours the hydroxyapatite crystals grow with preferred orientation in the (001) direction, as seen before on Bioglass® immersed in SBF for 7 days [7.14]. The data show that samples of 45S5 and 52S5 clearly show the growth of hydroxyapatite on the surface after 24 hours in TBS, however the 55S5 sample only shows the very beginnings of Bragg peaks after 24 hours in TBS, and is still mostly amorphous.

The high-energy X-ray diffraction data have shown that after 7 days immersion time the Bioglass® immersed in SBF appears to have the same structure as that immersed in TBS. The intermediate stages appear to show that the Bioglass$^{®}$ immersed in TBS reacts more quickly than that in SBF, which is not what one would expect given the composition of each of the fluids. This could be due to the growth of crystals actually being slower on the sample reacted in TBS, however the crystals growing larger and hence making them visible earlier.

References

[7.1] www.novabone.com

[7.2] Hench, L.L., *J. Am. Ceram. Soc*., **74**, 1487-510, 1991.

[7.3] Ogino, M., Ohuchi, F., Hench, LL., *J Biomed. Mater. Res.*, **14,** 55, 1980.

[7.4] Kim, C.Y., Clark, A.E., Hench, L.L., *J Biomed. Mater. Res.,* **26**, 1147, 1992.

[7.5] Cerruti, M., Greenspan, D.C., Powers, K., *Biomaterials*, **26**, 1665-1674, 2005.

[7.6] Zhong, J.P., Greenspan, D.C., Feng, J.W., *J. Mater. Sci., Mater. Med.,* **321**, 2002.

[7.7] Yashima, M., Sakai, A., Kamiyama, T., Hoshikawa, A., *J. Solid State Chem.,* **175** 272-277, 2003.

[7.8] Mathew, M., Brown, W.E., Schroeder, L.W., Dickens, B., *Journal of Crystallographic and Spectroscopic Research,* **18**, 235-250, 1988.

[7.9] de Andrade, A.V.C., da Silva, J.C.Z., Paiva-Santos, C.O., Weber, C., dos Santos Utuni, V.H., Tebcherani, S.M., Ferreira Borges, C.P., da Costa, E., Martinez Manent, S. *Ceramic Engineering and Science Proceedings,* **25,** 639-645, 2004.

[7.10] Kontonasaki, E., Zorba, T., Papadopoulou, L., Pavlidou, E., Chatzistavrou, X., Paraskevopoulos, K., Koidis, P., *Cryst. Res. Technol*., **37**, 1165-1171, 2002.

[7.11] Skipper, L.J., Sowrey, F.E., Pickup, D.M., FitzGerald, V., Rashid, R., Drake, K.O., Lin, Z., Saravanapavan, P., Hench, L.L., Smith, M.E., Newport, R.J., *J. Biomed. Mat. Res*., **70 A,** 356 – 360, 2004.

[7.12] Skipper, L.J., Sowrey, F.E., Rashid, R., Newport, R.J., Lin, Z., Smith, M.E**.,** *Phys. Chem. Glasses.*, **46,** 376, 2005.

[7.13] Skipper, L.J., Sowrey, F.E., Pickup, D.M., Drake, K.O., Smith, M.E., Saravanapavan, P., Hench, L.L., Newport, R.J**.,** *J. Mat. Chem*., **15**, 2369 – 2374, 2005.

[7.14] Rehman, I., Knowles, J.C., Bonfield, W., *J. Biomed. Mater. Res.,* **41**(1), 162-166, 1998.

Chapter 8

X-ray diffraction of bioactive calcia-silica sol-gel foams

8.1 Introduction

This chapter presents high energy X-ray diffraction to investigate the structure of a calcia-silica sol-gel glass with bioactive properties. Recent work has highlighted the potential of sol-gel derived calcium silicate glasses for the regeneration or replacement of damaged bone tissue. The mechanism of HCA layer formation and the requirements for optimisation of the properties of these materials are as yet only partially understood, but have been linked in previous studies [8.1, 8.2] to the particular nature of the calcium site in the glass, and to the way in which this controls the calcium dissolution from the glass matrix. The study carried out by Skipper *et al.* [8.2] was performed on powdered calcium silica sol-gel glasses of the composition $(CaO)_{0.3}(SiO_2)_{0.7}$, S70C30, which is the most highly bioactive composition of calcia-silica sol-gel glass. However, arguably the more interesting topical method for the production of bioactive glass scaffolds, with a similar morphology to trabecular bone, is the foaming of sol-gel derived bioactive glasses [8.3]. Whilst it is not anticipated that there will be a significant difference between the foamed and powdered glasses in terms of the atomic scale structure – it is the nature of the porosity that differentiates the two forms of calcium silicate material – it is nevertheless important to investigate in more detail the nature of the reaction mechanisms involved. Thus, the analogous experiment to that of Skipper *et al.* [8.2] has now been undertaken on these novel foamed bioactive calcia-silica sol-gel glasses.

In the earlier study on the higher density sol-gel derived glasses, complex multi-stage dissolution and mineral growth phases were observed as a function of reaction time with simulated body fluid, SBF, of between 30 minutes and 7 days. Using genuinely *in-situ* and time-resolved methods of X-ray diffraction, this experiment has now been taken one step further. The new *in-situ* methodology provides insight into the structure of key sites in these materials as they evolve through the various stages involved in the glass-SBF reaction. It thereby allows a detailed study of the mechanisms of reaction rather than merely providing a limited number of 'snapshots' at pre-defined times within a 'stop-go' experiment, in which the reaction was halted using an acetone wash and the resultant samples were then dried. Thus, the present study not only allows the careful study of the reaction, with significantly finer time steps, on a single sample, but moreover allows that study to take place with the sample fully immersed in SBF (i.e. 'wet'); it is therefore possible to comment more generically on their behaviour as bone regenerative materials.

The experiments described herein were focused on examining foamed calcium silicate sol-gel samples in order to investigate:- i) the effects on initial structure and HCA layer formation of foamed compared to non-foamed samples; and ii) the effects on the underlying structure of calcining foam preforms in the range 600-1000 ^{o}C.

Extensive measurements of bioactivity in previous studies [8.2, 8.4, 8.5] have shown that the above factors have profound effects on the bioactivity of non-foamed calcium silicates. The aim of the present diffraction experiments is therefore to relate this prior knowledge to the underlying structure of the calcium silicate network within a genuinely *in-situ*/time-resolved environment, and understand any difference in the effects these factors have on the kinetics and structure of *in-vitro* HCA formation in the case of a foamed sample.

8.2 *Ex-situ* X-ray diffraction

Firstly, the analogous experiment to that of Skipper *et al.* [8.2], was undertaken to investigate any differences in structure or reaction mechanisms that could occur from foaming the S70C30 bioactive sol-gel glass. An identical experiment to that carried out by Skipper *et al.* was undertaken on the foamed glass. Samples of S70C30 foamed glass, provided by Imperial College London, were ground into a fine powder, and reacted in SBF (SBF preparation described in Chapter 7). 50 ml of SBF was heated to 37 ºC in a beaker and allowed to reach thermal equilibrium, after which 75 mg of finely ground powder was added, with constant stirring, for times of 10, 20 and 30 minutes, 2, 5 and 24 hours. After each time period, each solution was filtered, rinsed briefly with deionised water and then acetone. The reacted powders were then dried in an oven at 100 ºC overnight.

The high energy X-ray diffraction (HEXRD) data were collected on Station 9.1 at the synchrotron radiation source (SRS), Daresbury Laboratory, UK. The finely powdered samples were enclosed inside a 0.5 mm thick circular metal annulus by kapton windows and mounted onto a flat-plate instrumental set-up. The wavelength was set at $\lambda = 0.4875$ Å, and calibrated using the K-edge of an Ag foil; this value was low enough to provide data to a high value of momentum transfer ($Q_{\max} = 4\pi sin\theta/\lambda$

~23 Å^{-1}). The data were corrected using the collection of programs described in Chapter 4.

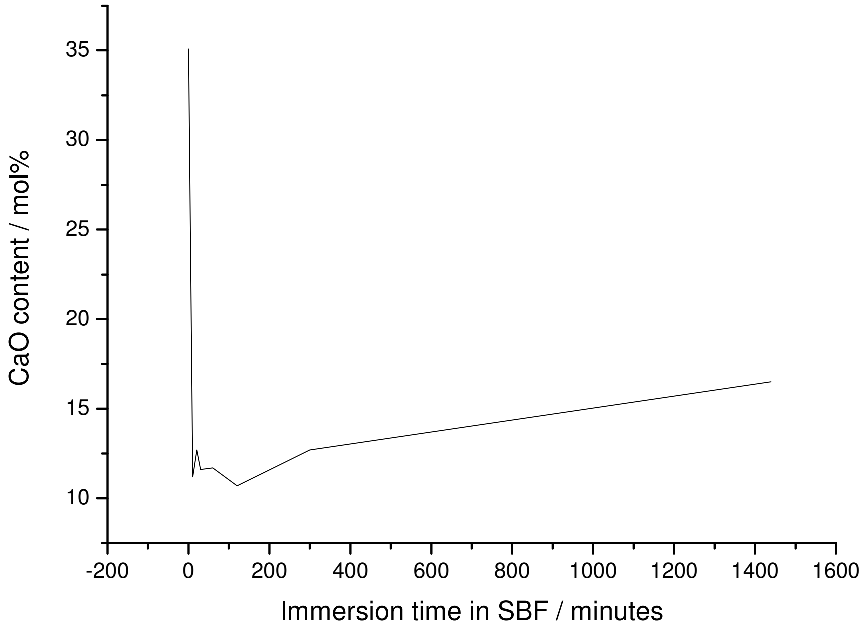

Figure 8.1: X-ray fluorescence data showing the calcium content of the glass as a function of time immersed in simulated body fluid; note the very rapid rate of loss during the first minutes of the reaction. (The variation of the phosphorus content of the glass is, approximately, the inverse of this – a rapid initial rise followed by a slower and more monotonic increase thereafter.)

Characterisation of the samples, necessary for the analysis of the diffraction data, was carried out. The sample compositions were determined using X-ray fluorescence (XRF) spectrometry and are shown in Figure 8.1. The XRF measurements were performed using a Bruker S4 X-ray fluorescence spectrometer, the densities of the samples were determined by helium pycnometry using a Quantachrome Multipycnometer.

Approximately 80% of the initial calcium content is lost from the sample within 30 minutes of reaction time, after which a gradual increase in calcium content occurs. A key observation is that the calcium content undergoes a series of oscillations during the initial reaction period, before entering a long period of more monotonic increase thereafter.

Experimentally determined structure factors *S(Q)* are shown in Figure 8.2. After 30 minutes the shape of the *S(Q)* has altered significantly, most notably on the high-Q side of the first principle diffraction peak. This is associated with the initial rapid dissolution of Ca. By 24hrs the *S(Q)* has the appearance of a poorly crystalline hydroxyapatite overlaying a (Ca-depleted) silicate glass interference pattern.

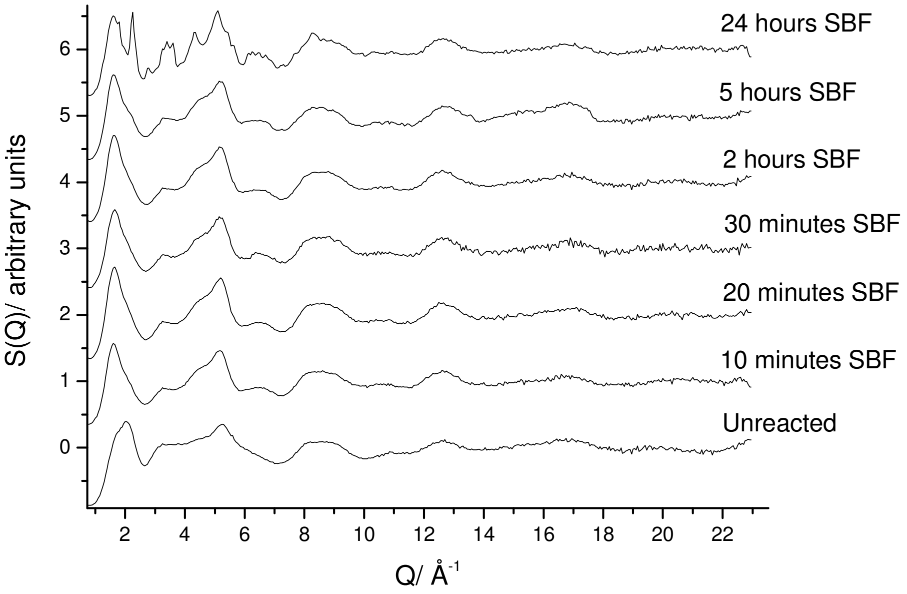

Figure 8.2: *S(Q)* functions for samples of S70C30 foamed bioactive glass, unreacted, and reacted in SBF for 10, 20, 30 minutes and 2, 5, 24 hours.

The structure factors are now Fourier transformed to produce the corresponding real-space pair correlation functions shown in Figure 8.3. In the corresponding real-space pair correlation functions, *D(r)*, the major feature at 2.02 Å only present in the SBF reacted samples corresponds to second neighbour O···H bond lengths found in hydrated calcium phosphates. All the peak changes mirror in real space the changes already identified in the *S(Q)*: the removal of Ca from the glass network and growth of a calcium phosphate layer followed by an increasingly ordered form of hydroxyapatite.

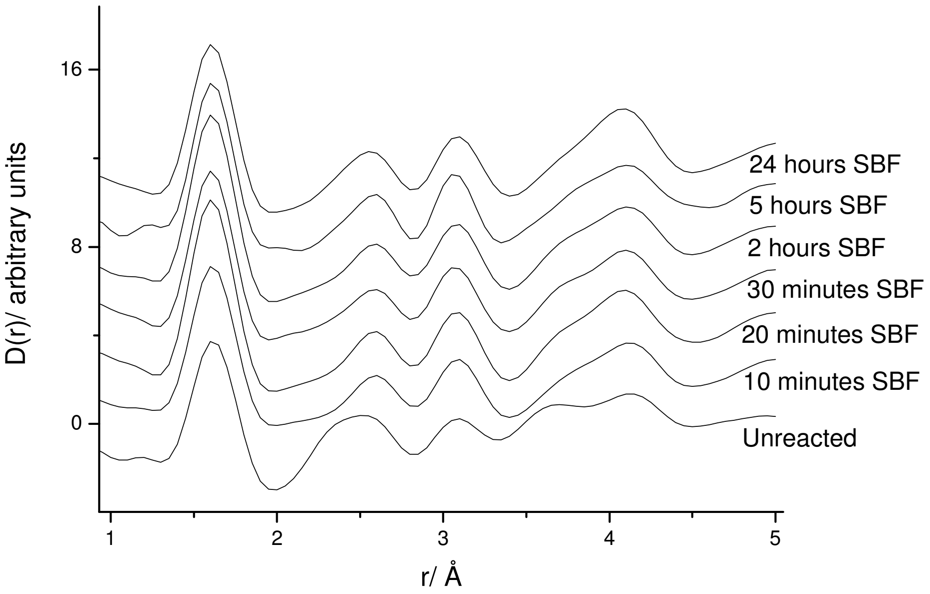

Figure 8.3: *D(r)* functions for samples of S70C30 foamed bioactive glass, unreacted, and reacted in SBF for 10, 20, 30 minutes and 2, 5, 24 hours.

The results of this experiment suggest that there are no atomic scale structural differences between the sol-gel S70C30 bioactive glass when it is unfoamed, or foamed. The principal peaks in the *D(r)* functions all match those identified in the experiment carried out by Skipper *et al*.

8.3 Raman Analysis

Two samples from the previous HEXRD experiment were analysed by Dr Simon FitzGerald, of HORIBA Jobin Yvon Ltd, using Raman spectroscopy. The two samples were S70C30 foam, and S70C30 foam reacted in SBF for 2 hours. The data for the two samples is shown below in Figures 8.4 and 8.5.

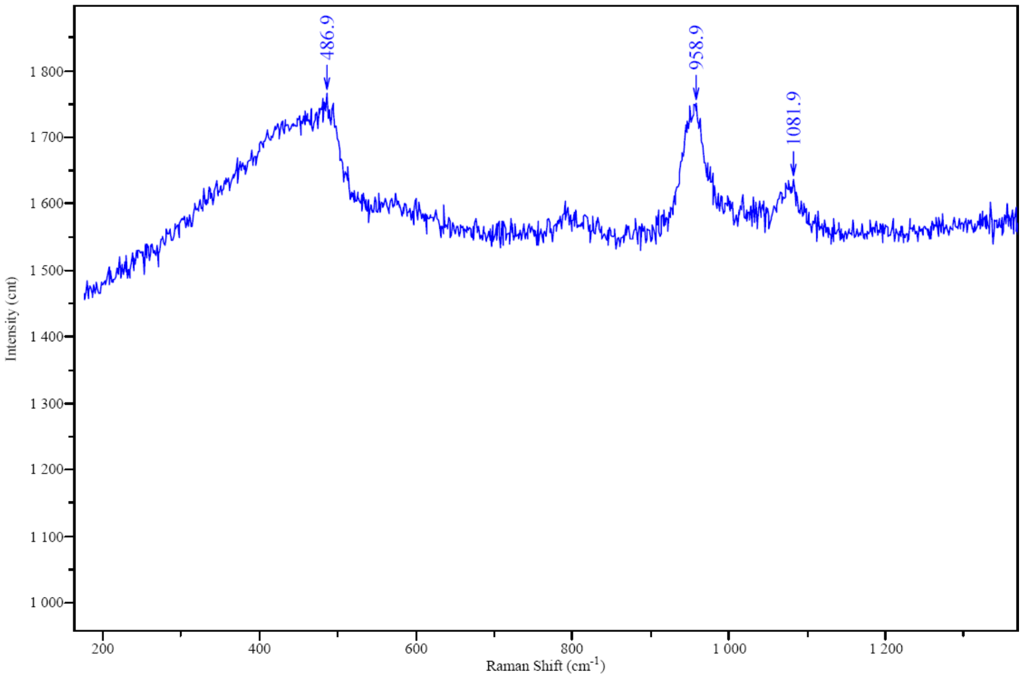

Figure 8.4: Raman data for the S70C30 foam.

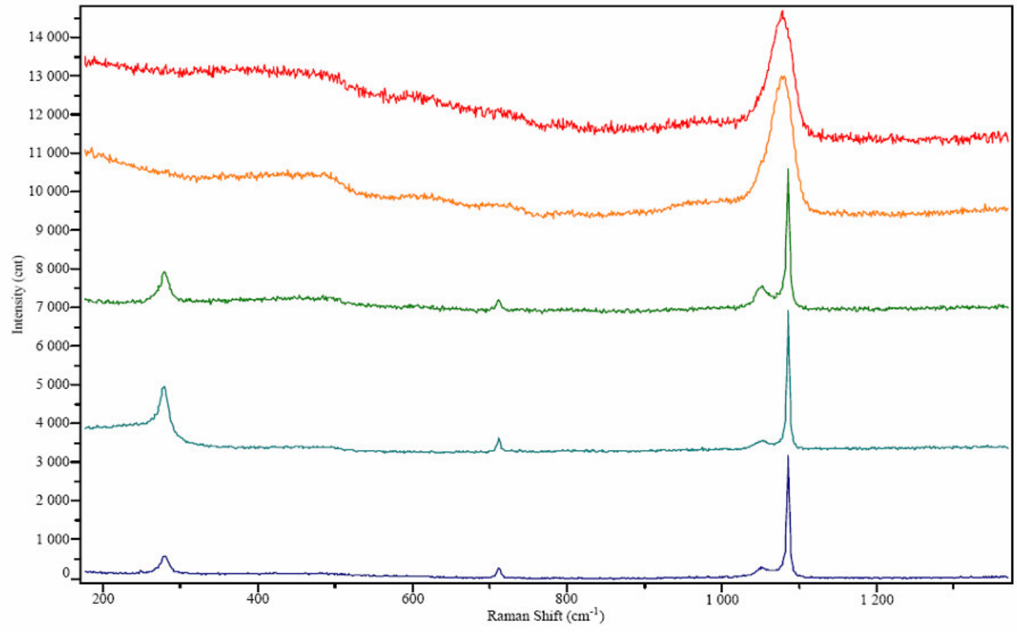

Figure 8.5: Raman data for S70C30 foam reacted in SBF for 2 hours.

The data for the unreacted S70C30 glass show only a weak Raman signature, with a relatively strong fluorescence background. Three peaks are visible, one at 487 cm^{-1} corresponding to an Si-O-Si band, one at 959 cm^{-1} corresponding to Si-O$_{nb}$ band and one at 1082 cm^{-1} corresponding to an Si-O-Si band. The data for the S70C30 glass reacted in SBF for 2 hours shows two distinct forms, one with very sharp bands (280, 712, and 1085 cm^{-1}) indicative of strong crystallinity, and the other with a broader weaker peak at 1080 cm^{-1} most likely due to an amorphous Si-O-Si structure. Any crystallinity in the SBF reacted sample would be due to the growth of calcium phosphates (as shown in the data in the previous HEXRD experiment), and previous measurements on a bioactive glass [8.6] showed a peak at ~ 1078 cm^{-1} which could be assigned to PO_4^{3-} tetrahedral. Therefore it is possible that the sharp peak observed at 1085 cm^{-1} is the P-O band involved with PO_4^{3-} tetrahedral. The small peak at 280 cm^{-1} is the region where one would expect to find metal-O Raman bands [8.7], and so this peak is assigned to the Ca-O band, showing some order in the new calcium environment also.

8.4 *In-situ* X-ray diffraction

For the next experiment on the same sample (S70C30 foam), the SBF treatments were carried out *in-situ* whilst high energy X-ray diffraction (HEXRD) data were collected on beamline ID15B at the ESRF, Grenoble, France. Samples of foam were held in a specially produced cell, which could be rotated, and heated in the beam (the temperature was kept at 37 ºC, i.e. to mimic the *in-vivo* environment, throughout the reaction by illumination using a halogen lamp, and monitored using a thermocouple). The cell is designed such that it allows *in-situ* mixing of the sol-gel precursors (i.e. for a study of the sol-gel processing itself [8.8]) or for the addition of liquid components, as was necessary for the present case. A diagram of the *in-situ* cell is shown in Figure 8.6. The cell was built to hold a sample of foam in the beam whilst SBF is passed over it by rotating the entire cell throughout the reaction. As shown in Figure 8.7, a cuboid sample of foam was held in place by two aluminium prongs. In order to retain the SBF in the cell, thin polymide (kapton) windows were used, held against an 'O'-ring seal. The sample cell was positioned in the 0.25 mm^2 X-ray beam, ensuring that the beam travelled through the middle of the cell, and had no contact with the aluminium prongs.

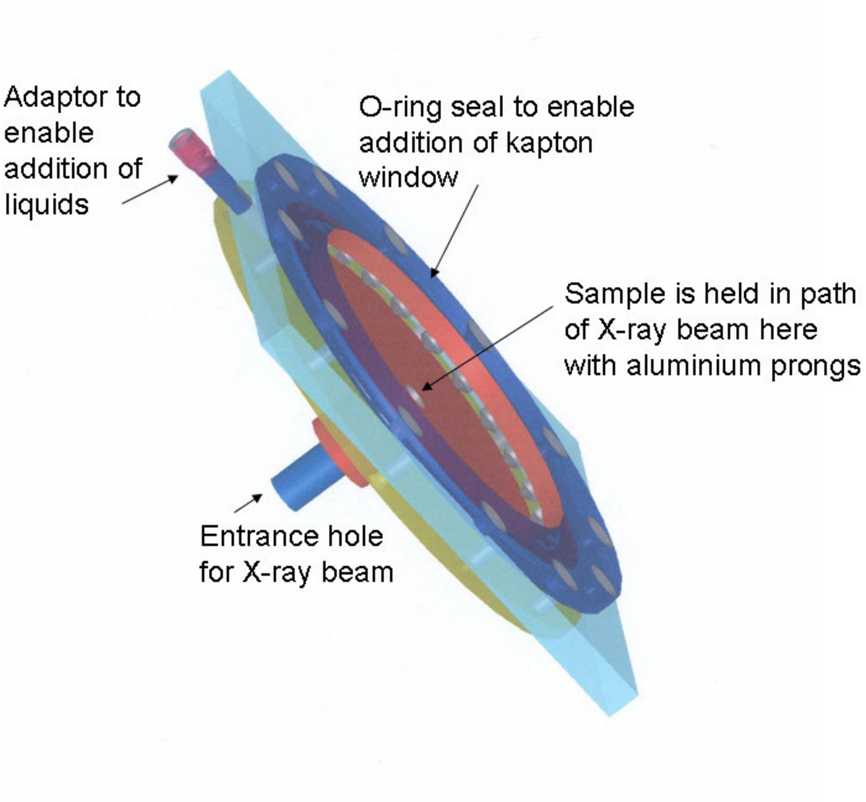

Figure 8.6: Schematic diagram of the *in-situ* cell.

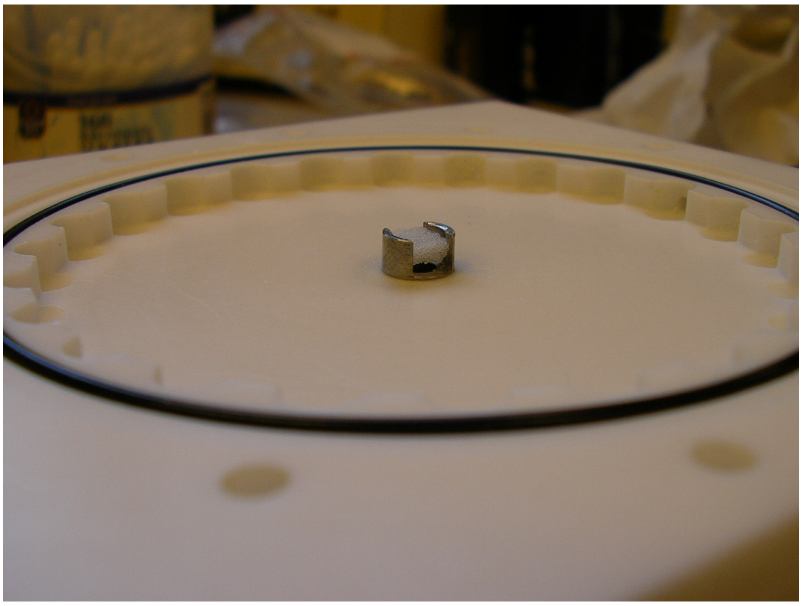

Figure 8.7: Photograph showing how the sample was loaded into the *in-situ* cell.

The X-ray photon energy was set to 97.5 keV, corresponding to a wavelength of λ = 0.127 Å. The beam size was collimated to 0.5 mm x 0.5 mm. The cell was positioned so that the sample to detector distance was 300 mm, which enable a Q range of ~2 to 23 $Å^{-1}$ to be detected by the MAR® 345 area detector. The experimental setup can be seen in Figure 4.4 in Chapter 4. A diffraction pattern was collected with SBF only in the cell in order to provide a suitable background. The dimensions of the sample and its mass were measured before and after each reaction.

After taking several scans of the unreacted sample with kapton windows in place, the SBF was injected into the cell; and the cell was then set rotating, and data collection was begun within approximately five minutes. Complete diffraction patterns were taken on a rolling basis every ~50s for the first 20 minutes, after which a pair of comparable ~50s scans were taken every 15 minutes. The reaction was monitored for up to 16 hours. When the reaction was stopped, the sample was removed and dried and it's mass and dimensions post-reaction measured.

The 2-dimensional images collected by the MAR345 detector were radially integrated about the centre of the image. The centre of the image and also the tilt of the detector were found and corrected for using software written in Matlab in-house at the ESRF, as described in Chapter 4, section 4.4.

Data analysis requires that the density and the composition of the sample is known; this creates obvious difficulties in the case of a time-resolved study of an *in-situ* reaction. We have made an *ad hoc* assumption that the mass changes linearly with time, which therefore gave a corresponding density for the sample in the beam for each scan. Also, previous results (shown in Figure 8.1), show the change of composition of a broadly similar sample with time immersed in SBF, measured *ex-*

situ; these were used to estimate the composition of the sample in the beam for each scan.

Each radial integration was normalised to the incident beam intensity. Corrections are made for the absorption due to the sample as well as for the absorption due to the air along the X-ray's optical path. The background associated with the scattering caused by the X-rays travelling through the air and empty cell is also measured and subtracted. Due to self-shielding and excluded volume effects, the scattered intensity recorded with the SBF alone is actually greater than that recorded with a sample inserted; thus, a linearly scaled version of the measured SBF background must be removed such that the resultant was positive at all points. After 2.5 hours in SBF at 37 °C, there were no significant differences between any two scans taken in each 15 minutes period, so these scans were summed together, after being normalised, in order to improve the statistical quality.

The data presented herein, have only been analysed semi-quantitatively due to the limitations of this study described above. During the *in-situ* experiment the composition and density of the sample at each stage had to be estimated as there was no way of measuring these quantities during the reaction. X-ray fluorescence data from previous work on unfoamed S70C30, was used to estimate the composition of the sample at each stage, and the density was assumed to change linearly with time (the mass of the sample before and after the reaction was used to calculate it). Therefore, the data in question is now analysed semi-quantitatively, as the areas of the peaks are subject to uncertainty on an absolute scale, although relative trends will be reasonably reliable, and in the context of attempting to follow the reaction processes these are extremely useful despite the limitations. Peak positions in the data should be reliable, and can provide some structural information on the sample during the reaction.

Figure 8.8 shows the structure factors for the unreacted foam samples, calcined at 600, 800 and 1000 ºC; there are evident differences between each sample.

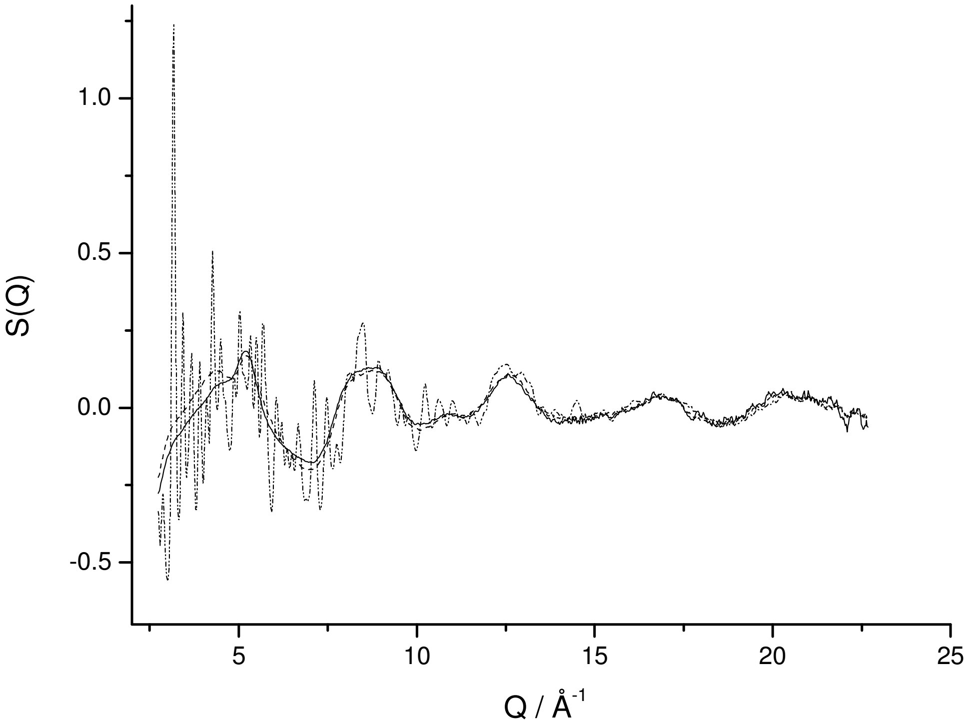

Figure 8.8: High energy X-ray diffraction data for the unreacted foam structure factors, *S(Q)*, corresponding to 600 °C (black line), 800 °C (dashed line) and 1000 °C (dotted line).

Figure 8.9 shows the high energy X-ray diffraction pair distribution functions for the unreacted samples. The main difference between the foam heated to 600 ºC and the foam heated to 800 ºC in the *S(Q)* functions is the peak at 4.4 Å^{-1} which is more prominent in the 800 ºC foam *S(Q)* than in the 600 ºC foam *S(Q),* where it appears only as a shoulder. The *Q*-space data for the 1000 ºC foam shows that this sample is at least partially crystalline, as evidenced by the many Bragg peaks, whereas the other two samples appear to be amorphous. This agrees with conventional XRD spectra obtained on S70C30 foams, which were shown to be amorphous after sintering for 2 h at 800 ºC and showed Bragg peaks corresponding to natural wollastonite after sintering for 2h at 1000 ºC [8.2]. The Bragg peaks revealed in the present data are indicative of a mixture of wollasonite and pseudowollastonite type material. [8.9, 8.10, 8.11]

When looking at the corresponding real-space data associated with these three samples, one must remember that the minimum *Q* value for these samples was > 2 $Å^{-1}$ which would influence the Fourier Transform to *T(r).* Three major features are seen to occur in all *T(r)* functions. The first major peak is assigned to the Si-O correlation at 1.61 Å. The second peak, centred at 2.5 Å, is associated with the Ca-O first-shell correlations and the second-shell O···O correlations. The third peak, centred at 3.2 Å, is associated with the Si···Si correlation and the Si···Ca correlation shells. To assign these peaks in the present samples, data from a previous experiment on the same composition of (non-foamed) glass was used [8.2].

Figure 8.9 shows the three *T(r)* functions together. The differences between the 600 ºC and 800 ºC foams are small, and mostly visible in the peak centred at 2.5 Å.

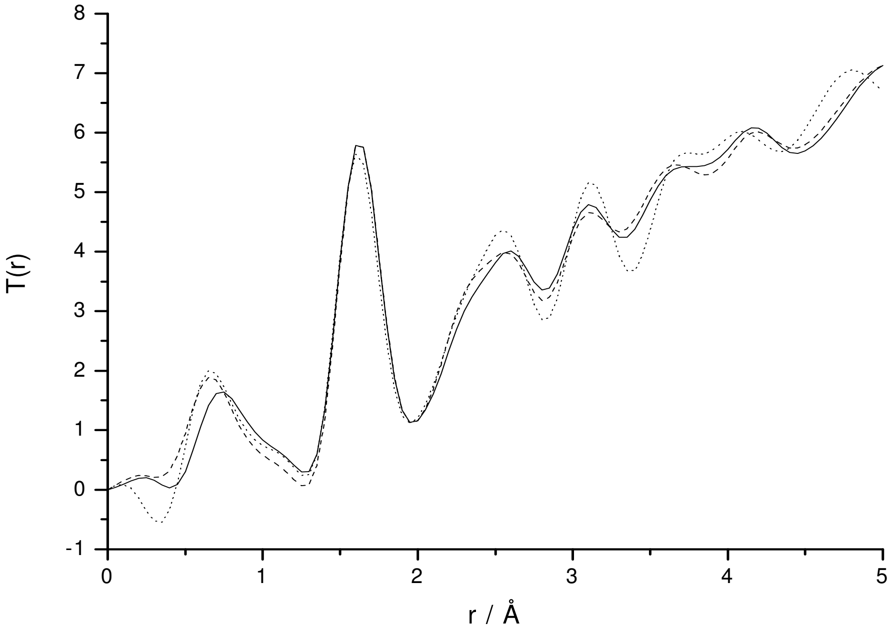

Figure 8.9: High energy X-ray diffraction data for the unreacted foam pair distribution functions, *T(r)*, corresponding to 600 °C (black line), 800 °C (dashed line) and 1000 °C (dotted line).

This broad peak comprises three Ca-O correlation shells at 2.3, 2.5 and 2.8 Å, along with the O···O coordination at 2.6 Å. The 800 ºC foam appears to have a more prominent peak at 2.3 Å and a weaker peak at 2.8 Å than the 600 ºC foam. This is taken to imply that there is a difference in calcium environment between the two samples. The 1000 ºC foam appears to have a stronger contribution from Ca-O peaks at 2.3 and 2.5 Å, and a weaker contribution from the Ca-O peak at 2.8 Å than either of the other two samples. Jones *et al.* [8.3] showed the 1000 and 800 ºC foams to form HCA layers at 3 days in SBF compared to 8 hours for the 600 ºC foam. This result could indicate that the Ca-O correlation at 2.8 Å is the correlation relating to the dissolution of Ca in the first stage of reaction in SBF. Given that the 1000 ºC foam shows strong Bragg peaks in the *Q*-space data, with a strong peak at 2.53 Å and a slight shoulder at 2.3 Å in the corresponding *r*-space data, we may surmise that at the near-neighbour scale, this sample has structural similarities to a psuedowollastonite type of material in which the Ca environment is 8-fold coordinated with an average Ca-O correlation occurring at ~2.53 Å [8.9, 8.11, 8.12]. We note however that pseudowollastonite has a particularly diffuse Ca-O environment in which bond lengths range from 2.28 to 2.72 Å.

Figure 8.10 shows the *in-situ* diffraction data for the foam sintered at 600 ºC. The reaction was followed for ~16 hours. The data shows that within a few minutes of the SBF being added to the glass, changes in the *S(Q)* are apparent. After ~1 hour there is clear evidence for the formation of Bragg diffraction peaks, which indicates the growth of crystallites in the sample. After ~3 hours the Bragg peaks appear very strong, indicating a significant polycrystalline layer. The peaks are indicative of tricalcium phosphate, HA, and after 5 hours peaks indicative of HCA are visible, e.g. the peak at 5.08 $Å^{-1}$ [8.9]. The peaks are atop the underlying amorphous pattern. While a comparable qualitative observation was made in the context of the *ex-situ* unfoamed samples [8.2], in the case of the foamed samples examined in this paper the polycrystalline phase remains present in the glass right up until the reaction was stopped at ~16 hours, whereas in the unfoamed materials the initial crystallite growth was seen to become more like an amorphous HA at 10 hours of immersion. Thus, it is apparent that the porosity and/or calcination temperature-linked glass network connectivity of the material has an important effect on its *in-vitro* reaction with SBF. Alternatively, it may be possible that in the data for the non-foamed samples, the sample contains a mixture of many calcium phosphate phases which, when combined, yield an apparently amorphous pattern due to the overlapping of Bragg peaks.

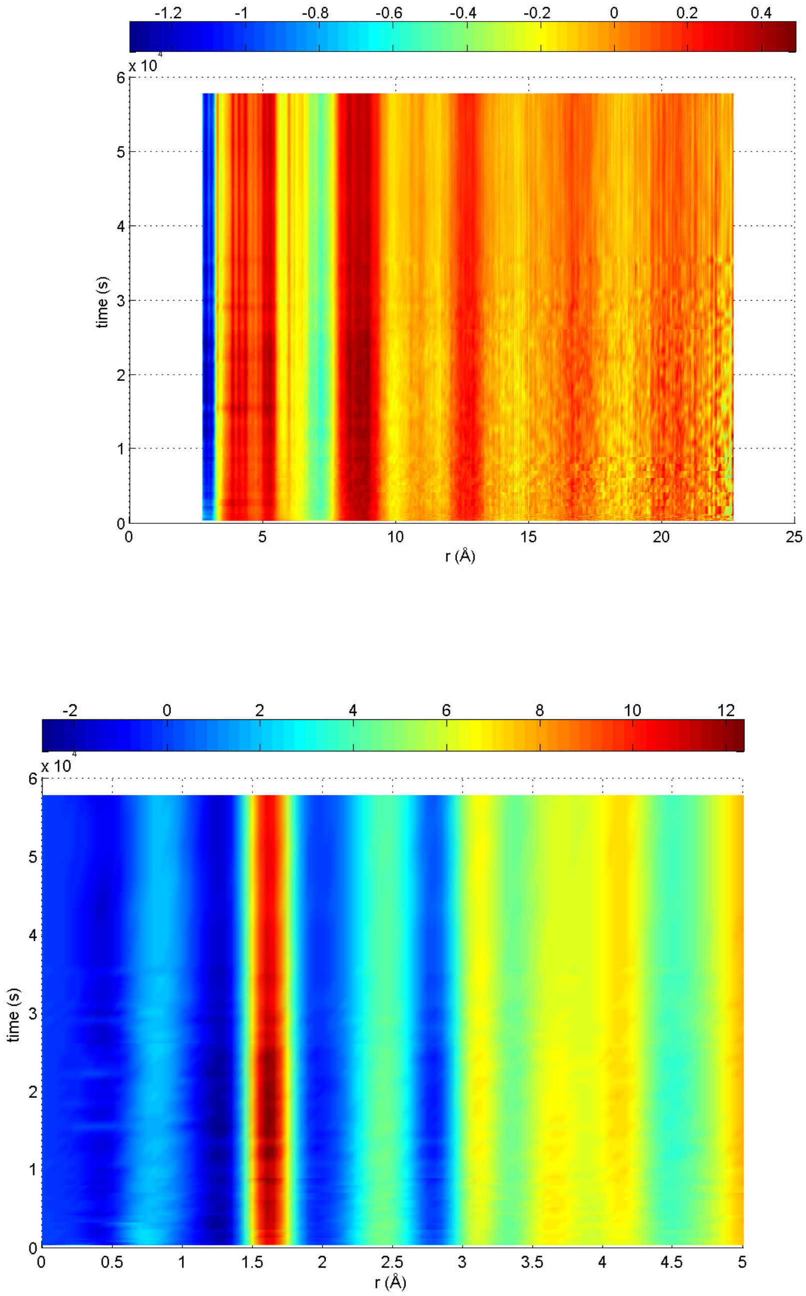

Figure 8.10: High energy X-ray diffraction data for the 600 ºC foam throughout reaction in simulated body fluid to ~16 hours, (a) *Q*-space structure factors, *S(Q)*, and (b) pair distribution functions, *T(r)*.

The first peak in the *T(r)* functions is assigned to the Si-O peak, in the unreacted data, but to a combination of Si-O and P-O correlations in the reacted-glass data. The peak is at ~1.6 Å for all data runs, and the change in height of the peak may be associated with the fluctuating phosphorus content in the sample as the reaction takes place. A previous study [8.2] showed that the phosphorus content mirrors that of Ca and increases sharply when the reaction begins before undergoing a series of oscillations during the initial reaction period and then levelling off. The first peak in the *T(r)* functions shows an increase in intensity as soon as the reaction is started, which then increases slowly during the reaction, fluctuating slightly. This peak intensity change is in unison with the measured phosphorus content for the first 16 hours of reaction as seen in Skipper *et al.* [8.2].

The second feature in the *T(r)* functions centred at 2.5 Å, arising from both Ca-O and O···O correlations, appears as a broad peak in the unreacted sample, and then becomes a narrower feature centred at 2.4 Å as the reaction proceeds. The data implies that from near the point at which the reaction is started, there is a rapid impact on the Ca-O distances of 2.3 and 2.8 Å, which is almost certainly associated with initial calcium loss, as previously observed [8.13].

In molecular dynamics simulations of a sol-gel glass of the same composition and density to that studied by Skipper *et al.* [8.2], three Ca-O environments were also postulated [8.14]. The three environments were shown to correspond with Ca-O_{nb} (~2.3 Å), Ca-OH (~2.5 Å) and Ca-O_b (~2.7 Å). The studies performed by Skipper *et al.* [8.2] and Newport *et al.* [8.13] indicated that during the initial 30 minutes of reaction time, the peak at 2.3 Å decreased significantly in area, and the peak at 2.5 Å became dominated by the peak at 2.7 Å. This is indicative of the formation of calcium phosphates after immersion in SBF as the Ca-O correlations in calcium phosphates are found at longer bond distances. In the *in-situ* data presented herein, the peak at 2.3 Å significantly decreases in area with the introduction of SBF, however the peak at 2.5 Å increases with intensity, and the peak at ~2.7 Å disappears. This could also be indicative of the growth of calcium phosphates, given the large number of possible alternatives. However, it certainly indicates that during the *in-situ* experiment we observe more Ca-OH correlations, which may not have been apparent in the *ex-situ* 'stop-go' reaction data due to the drying of the samples after reaction in SBF.

There are other significant differences in the present *in-situ* data compared with the previously observed *ex-situ* data. It appears from Figure 8.11 that the O···O correlation peak, associated primarily with the host silica network, weakens as the reaction takes place which indicates that the reaction is disrupting the underlying glass network. The O···O correlation is evidently moving to shorter distances, as the calcium is removed from the glass network and the growth of a calcium phosphate layer occurs. In addition, Fig. 8.11 also shows that the peak at ~3.2 Å, associated with the Si···Si second nearest neighbour distance and the Si···Ca correlation, narrows; implying an increase in Si···Ca hetero-coordination and a decrease in Si···Si homo-coordination. This may be due to the growth of a calcium phosphate layer, followed by an increasingly ordered form of HA, and then HCA.

Figure 8.11 shows the *in-situ* diffraction data for the reaction of the 800 ºC foam in SBF. Both the *Q*-space and the *r*-space data show that the reaction of the foam calcined to 800 ºC is different from the 600 ºC calcined foam's reaction in many ways.

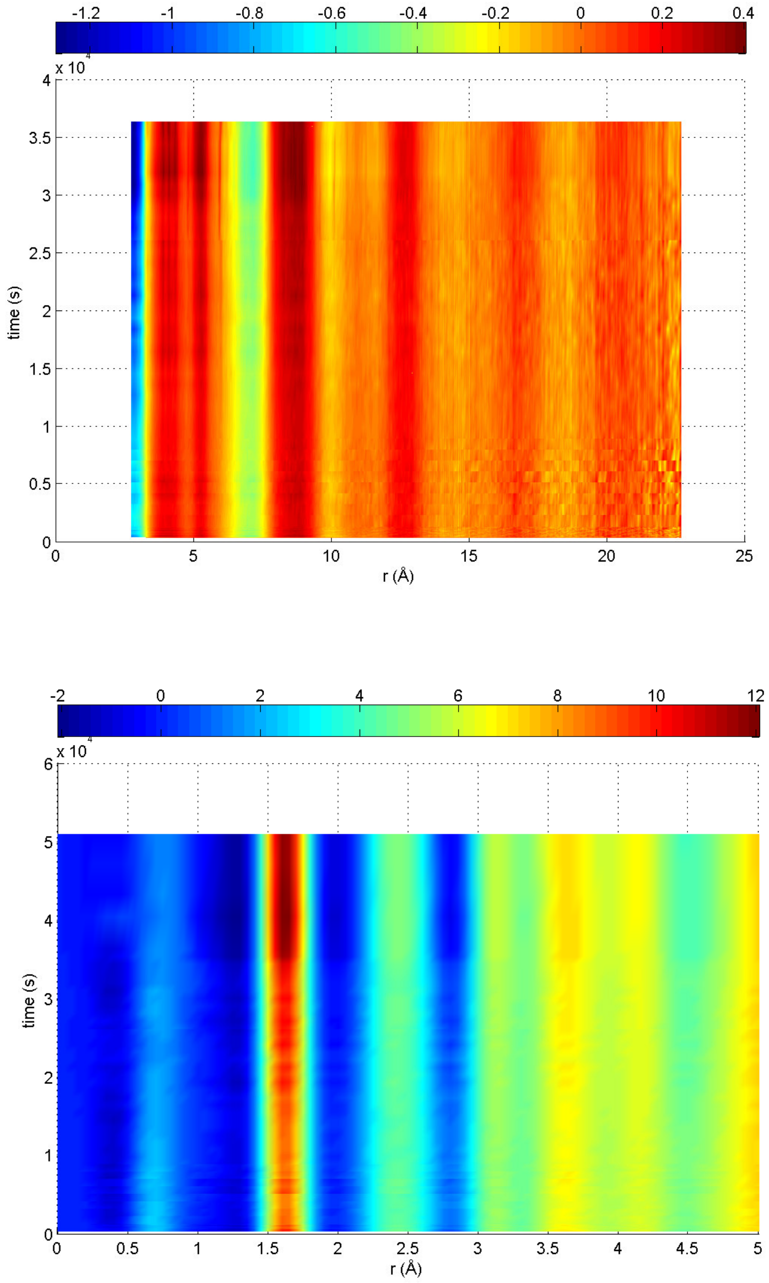

Figure 8.11: High energy X-ray diffraction data for the 800 °C foam throughout reaction in simulated body fluid for ~16 hours, (a) Q-space structure factors, $S(Q)$, and (b) pair distribution functions, $T(r)$.

Firstly, the *Q*-space data reveals that the Bragg peaks, which are beginning to form after only 1 hour in SBF for the 600 ºC foam, start to form only much later on in the reaction for the 800 ºC foam, at ~ 8 Hr. The Bragg peaks associated with tricalcium phosphate and HA are visible, but in this case there is no indication of the growth of HCA. In the *T(r)* functions, similar changes are occurring in the Si-O/P-O peak at 1.6 Å and in the peak corresponding to the Ca-O correlations and O···O correlations, however they appear to be changing at a slower rate than for the 600 ºC foam. The main difference between samples is however observed in the peak at ~3.6 Å, which in the 800 ºC foam is present throughout the reaction, although becoming slightly narrowed and more prominent. In the 600 ºC foam however, the corresponding peak at first became narrow and more prominent, but then ceases to change in height or width, after which the peak at 4.1 Å then becomes more prominent. At no point in the ~16 hours of the reaction for the 800 ºC foam does the peak at 4.1 Å become more prominent than the peak at 3.6 Å. The peak at 3.6 Å was associated in the unreacted sample with Ca···Ca correlations, and with Ca···Ca and Ca···P correlations once the reaction has started. The peak at 4.1 Å may be associated with inter-tetrahedral P···P and P-O correlations in HA (or, were it present, HCA).

The techniques developed here have allowed the non-invasive *in-situ* monitoring of the surface reactions of bioactive glass foams in real time. The foam sintered at 600 ºC shows indications of Bragg peaks after only 1 hour immersion, and after 5 hours shows Bragg peaks related to HCA. The foam sintered at 800 ºC shows the same reaction stages as the 600 ºC foam; however the reaction appears to be occurring at a slower rate. Bragg peaks begin to form after 8 hours immersion, and they are indicative of tricalcium phosphate and HA but not HCA. The changes in dissolution and bioactivity are due to changes in the atomic structure which were shown in previous XRD data brought about by sintering [8.3]. The changes in atomic structure dictate the nanopore size and specific surface area (SA/V). The modal nanopore size of foams sintered at 600 °C was 17 nm (SA/V = 107 m^2g^{-1}), while foams sintered at 800 °C had a modal nanopore size of 12nm (SA/V = 42 m^2g^{-1}).

8.5 X-ray fluorescence investigation

During the course of work performed on the foamed S70C30 bioactive glass, some anomalous results for composition were obtained. Therefore a detailed compositional study was undertaken. Samples of powdered foam were analysed using x-ray fluorescence measurements, along with samples of whole foam. The foams are produced in cylindrical form, shown in Figure 8.12. The foams were placed in the XRF machine with one flat side down, and then turned over so that the composition of each 'side' could be compared. The results from these measurements are shown in Table 8.1 along with the ICP analysis of one foam, and the XRF results from an unfoamed sample of S70C30 glass.

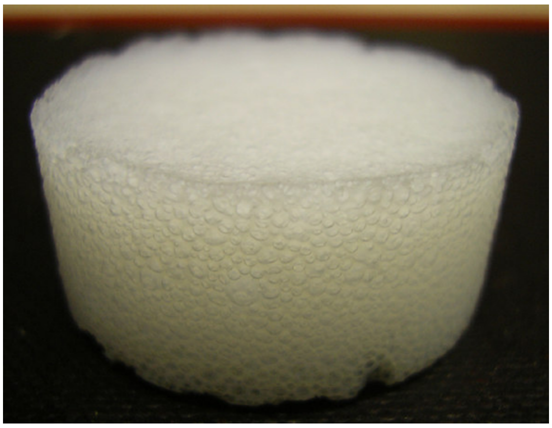

Figure 8.12: Photograph showing foam produced.

Sample	CaO / wt%	SiO_2 / wt%	Ca / at%	Si / at%	O / at%
MEDAC ICP analysis			0.0568	0.2246	0.6823
XRF analysis of sample analysed by MEDAC	34.8	65.2	0.1380	0.2413	0.6207
Unfoamed sample	30.3	69.5	0.1184	0.2535	0.6281
Powdered foam A	32.7	67.3	0.1288	0.2474	0.6238
Powdered foam B	26.7	73.3	0.1032	0.2645	0.6323
ρ=0.184 whole foam side A	34.2	65.8	0.1354	0.2431	0.6216
ρ=0.184 whole foam side B	22.8	77.2	0.0871	0.2753	0.6377
ρ=0.206 whole foam side A	30.8	69.2	0.1206	0.2529	0.6265
ρ=0.206 whole foam side B	24.1	75.9	0.0924	0.2717	0.6359
ρ=0.214 whole foam side A	22.8	77.2	0.0871	0.2753	0.6377
ρ=0.214 whole foam side B	20.1	79.9	0.0762	0.2826	0.6413
ρ=0.219 whole foam side A	21.6	78.4	0.0822	0.2785	0.6393
ρ=0.219 whole foam side B	24.1	75.9	0.0924	0.2717	0.6359

Table 8.1: Table of x-ray fluorescence results comparing several different S70C30 foams. Also included are ICP results for reference, and results for an unfoamed sample of S70C30 glass.

Results show differences in composition between foam samples. The ICP analysis performed by MEDAC Ltd, shows that the amount of Ca is less than would be expected, and the reason for this has been mentioned in chapter 6. For all samples, ICP analysis appears to underestimate the calcium content, and therefore no ICP results have been used in compositional analysis in any of the experiments. The XRF results for the sample analysed using ICP shows more realistic results for composition, as was found in the study of Bioglass® presented in chapter 6. Two powdered foams were analysed using XRF, and the results differed significantly. The results from taking XRF measurements from both sides of the whole foam pieces showed that in all cases, there was a significant difference in composition between each side. Specifically, one side of the foam contained a higher concentration of calcium than the other. This is believed to be caused during the materials processing of the foam, when the foam is at the drying stage of processing. After foaming, the sol is placed into moulds and sealed to age at 60 ºC for 72 hours, then the temperature is increased to 130 ºC and the seal broken to allow slow solvent evaporation as the foam dries. During the aging process, the calcium nitrate is in liquor form and the foam is stationary (i.e. there is no further agitation of the sample). During the drying process, the $CaNO_3$ is deposited on the pores from the liquor, however as the foam is dried and solvent evaporation occurs, the evaporation occurs at the top of the foam first, leaving more time for $CaNO_3$ to be deposited from an increasingly concentrated fluid at the bottom of the foam's container. This could cause an eventual higher concentration of Ca at the bottom layer of the foam.

During all experiments carried out on the foams, the composition of the particular foam used was taken before each experiment and used in the data analysis so this will not affect the results. The one exception is the *in-situ* X-ray diffraction experiment described in section 8.3 above. However, in this experiment it was not feasible to measure the composition throughout, so estimates were made using previous XRF measurements on a foamed and unfoamed sample of S70C30 glass. This was not ideal, however it enabled the results to be analysed semi-quantitatively and allowed the demonstration of a new method of *in-situ* investigation into these materials and their reaction mechanisms in SBF.

8.6 Summary

The initial experiment was designed to investigate any structural differences between the S70C30 foamed and unfoamed, and also any differences in reaction mechanisms with SBF. This was done by performing an analogous experiment to that performed on unfoamed S70C30 glass. It is clear from the results that foaming the glass has little or no effect on the structure of the glass or on the reaction mechanisms when immersed in SBF. In this HEXRD data we observe the growth of calcium phosphates after 24 hours immersion in SBF; however Raman spectroscopy data reveal that after 2 hours in SBF there is evidence of calcium phosphate forming.

Describe herein is a method which may be used for *in-situ* time resolved high energy X-ray diffraction studies of reaction mechanisms such as those involved when a bioactive calcia-silica sol-gel glass is immersed in SBF. Although, in this particular case, the method can only generate semi-quantitative data, it is nevertheless demonstrated that structural changes in the glass as a function of reaction time can be observed. Analysis of the XRD data from this experiment yields reliable atomic distances (i.e. pair correlations) at different stages of the glass dissolution and of the surface-related calcium phosphate/hydroxyapatite formation. Changes in the atomic distances and relative coordination numbers may therefore be assessed as a function of time in relation to the structure of both the glass matrix and the reaction products, and thus allow an insight beyond the ‘snapshots’ available hitherto. This detailed structural information facilitates a clearer discernment of the ways in which materials processing affect a given sample; in the present case, to inform the optimisation of calcium silicate materials used in tissue engineering applications.

References

[8.1] Saravanapavan, P., Verier, S., Jones, J.R., Beilby, R., Shirtliff, V.J., Hench, L.L., Polak, J.M., *Bio-Med Mats & Engineering*., **14**(4), 467-486, 2004.

[8.2] Skipper, L.J., Sowrey, F.E., Pickup, D.M., Drake, K.O., Smith, M.E., Saravanapavan, P., Hench, L.L., Newport, R.J., *J. Mater. Chem.,* **15,** 2369-2374, 2005.

[8.3] Jones, J.R., Ehrenfried, L.M., Hench L.L. *Biomaterials*, **27**, 964-973, 2006.

[8.4] Sepulveda, P., Jones, J.R., Hench, L.L., *J. Biomed. Mater. Res.,* **59**, 340-348, 2002.

[8.5] Saravanapavan, P., Jones, J.R., Pryce, R.S., Hench, L.L., *J. Biomed. Mater. Res.*, **66A**, 110-119, 2003.

[8.6] Notingher, I., Boccaccini, A.R., Jones, J.R., Maquet, V., Hench, L.L., *Materials Characterisation*, **49**(3), 255-260, 2002.

[8.7] Smith, E., Dent, G., *Modern Raman Spectroscopy-A Practical Approach*, John Wiley & Sons Ltd, Chichester, UK, 2005.

[8.8] Drake, K.O., PhD Thesis, A multi-technique study of the structural evolution of selected silicate-based sol-gel materials, September 2006, University of Warwick.

[8.9] Fletcher, D.A., McMeeking, R.F., Parkin, D., *J. Chem. Inf. Comput. Sci.*, **36**, 746-749, 1996.

[8.10] Ohashi, Y., *Phys. Chem. Minerals,* **10**, 217-229, 1984.

[8.11] Yang, H.-X., Prewitt, C.T., *American Mineralogist*, **84**, 929-932, 1999.

[8.12] Sowrey, F.E., Skipper, L.J., Pickup, D.M., Drake, K.O., Lin, Z., Smith, M.E., Newport , R.J., *Phys. Chem. Chem. Phys.,* **6**, 188-192, 2004.

[8.13] Newport, R.J., Skipper, L.J., FitzGerald, V., Pickup, D.M., Smith, M.E., Jones, J.R., *J. Non. Cryst. Solids,* **353**, 1854-1859, 2007.

[8.14] Mead, R.N., Mountjoy, G., *Chem. Mater.,* **18***,* 3956-3964, 2006.

Chapter 9

Small angle X-ray scattering from calcia-silica bioactive sol-gel foams

9.1 Introduction

This chapter describes work undertaken using small angle X-ray scattering to investigate the structure of a bioactive calcia-silica sol-gel foam scaffold. The technique was used to investigate the structural changes occurring as a function of stabilisation temperature in order to observe the growth of mesopores, which control the degradation rate and may act as sites for cell or protein attachment [9.1, 9.2]. The textural mesopores contribute most heavily to the surface area, and therefore affect the dissolution of Ca and the deposition and growth of calcium phosphates and hydroxyapatite (i.e. the mineral component of bone) – and it is these pores focused upon in this chapter. In this study the stages associated with materials processing are investigated. This materials processing follows an established generic procedure [9.2] and is illustrated in Figure 5.1 in Chapter 5.

Specifically, the processing of the dried gel is followed, which previous solid state NMR and Raman spectroscopy experiments (conducted on non-foamed samples [9.3]) suggest is comprised of relatively well-defined stages of network modification that may impact upon the porous nature of the material (and thereby, ultimately, on the dissolution of the resultant glass both *in-vitro* and *in-vivo*). (Results shown in Figure 9.1).

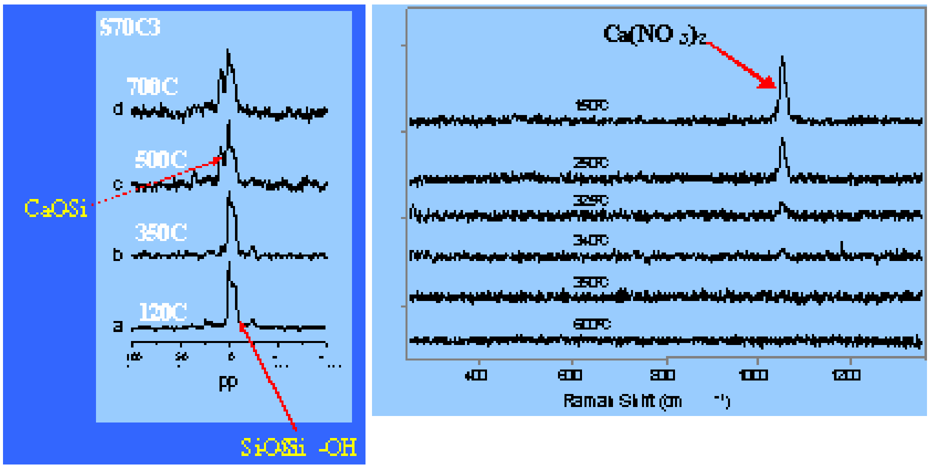

Figure 9.1: NMR and Raman spectroscopy data investigating the dried bioactive calcia-silica sol-gel foam at various stages of the stabilisation process [9.3].

There are two key pertinent points to emerge from these earlier studies on non-foamed materials: *i*) it is only at around 350 ºC that the Ca, initially incorporated into the reaction mixture as the nitrate, is finally incorporated into the silica glass network. This is highly likely to be associated with changes to the porosity of the material and/or the surfaces of those pores present; and *ii*) this specific effect will take place against the background of the evolution of the mesoporous material as a function of temperature, which is likely to include both mass and surface effects associated with the progression from a relatively low density hydrated xerogel to the final thermally stabilised (yet still porous, [9.2]) glass. In this experiment the heating of the sol-gel scaffold is follwed, *ex-situ*, to 600 ºC, which corresponds to the stabilisation and densification of the foam in the process.

Also in this chapter time-resolved *in-situ* data is presented following the foamed bioactive glass as it reacts with simulated body fluid (SBF, a standard solution of salts in water described in Chapter 7) at 37 ºC. Previous solid state NMR and X-ray diffraction data on the non-foamed analogue materials [9.4] showed that the dissolution of the Ca from the glass (and more slowly, the dissolution of the silica) is associated with the growth of minerals onto and within the porous glass. This evidence suggested that an amorphous – or, rather, a highly disordered polycrystalline – calcium phosphate phase forms after only 1 hour of immersion, which then partially crystallised within 5 hours; this is followed by the formation of a disordered hydroxyapatite phase by ~24 hours, which itself eventually crystallises.

The reaction is followed by both SAXS, which reveals the nature of the pores in the solid phase as a function of reaction time, and simultaneously using X-ray diffraction (wide-angle X-ray scattering, WAXS) which monitors the mineral growth phases.

9.2 Heat treated foams

Bioactive glass foam scaffolds of foamed S70C30 bioactive sol-gel glass, supplied by Imperial College, London, were taken through the processes outlined in Figure 5.1, Chapter 5, up to and including the drying stage at 130 ºC. Thermal stabilisation of the foams involves the heating profile shown in Table 9.1. The samples studied in the present work were taken through this stabilisation process in stages, namely to 100, 300, 400 and 600 ºC. Samples were removed from the oven at the specified temperatures, allowed to cool to room temperature, and then ground into powder before being thinly sprinkled between two mica windows that were held between a pair of simple annular metal rings. Two foams of the same composition were studied sequentially in order to assess reproducibility and thereby to provide a more reliable final set of data. The second set of data may be found in graphical form in Appendix 5.

Temperature / ºC	**Step / ºC.minute^{-1}**
100	**1**
300	**0.5**
HOLD	**2 HOURS**
600	**1**
HOLD	**5 HOURS**
COOL	**5**

Table 9.1: Table showing the heat-treatment procedure used in the final (stabilisation) stages of sol-gel foam processing.

The small angle X-ray scattering, SAXS, experiments were carried out using station 6.2 at the Daresbury Laboratory Synchrotron Radiation Source (SRS), UK. The beamline was equipped with a 2-crystal double-bounce, sagittaly-bent Si(111) monochromator that yielded a monochromatic (λ = 1.40 Å) and horizontally focused beam. The WAXS detector is mounted rigidly onto a nosecone sited adjacent to the sample position, and in this position it has an acceptance angle of 7° to 67° in 2θ in the upwards vertical plane. Beyond the nosecone, a variable-length evacuated small-angle X-ray scattering (SAXS) camera tube is fitted, with a length of 4 m chosen for this study. At the end of the SAXS tube a 2-dimensional small-angle detector is aligned to be effective in the downward vertical plane. The SAXS detector utilises a standard aperture design of a 60° quadrant and is functionally complementary to the curved WAXS detector, i.e. enabling truly synchronised SAXS and WAXS measurements to be made. [9.5] Given this instrument geometry, the dynamic range of the SAXS data extended from $Q = 2.12\ 10^{-3}$ Å^{-1} to $Q = 0.246$ Å^{-1}, where $Q = 4\pi \sin\theta/\lambda$. The corresponding range for the WAXS detector was $Q = 0.65$ to 5.03 Å^{-1}.

For the thermal stabilisation experiment, three scans (frames) of 120s each were taken of each sample. Data was normalised to compensate for the variation in the incident beam flux. The three frames were then averaged together before the background of the empty sample holder was removed.

SAXS data was calibrated using a reference of wet rat tail collagen [9.6], and WAXS data was calibrated using a reference of silicon powder [9.7].

Where Bragg peaks were observed in the WAXS data, the Scherrer equation (9.1) was used in order to estimate crystallite sizes [9.8],

$$d = \frac{K\lambda}{\beta \cos\theta} \qquad (9.1)$$

where β is the full width at half-maximum height (FWHM) of a diffraction peak at angle θ (duly corrected for instrumental broadening using the peaks observed from Si), and λ is the wavelength of the X-rays used. The value of the constant K is dependent on the method used to derive the equation. In this work it is taken as 1.0, but the exact value for K is not important as the crystallite size is only expected to be accurate to ±10%. The FWHM determined for a given isolated diffraction peak, after correction for instrumental broadening, was used within the Scherrer equation to obtain an estimate for the crystallites' size, then the values calculated for each peak were averaged together in order to reduce the potential problems associated with preferred orientation effects.

Figure 9.2 shows the SAXS and WAXS data associated with the *ex-situ* heat-treatment of the dried calcia-silica xerogel. Both the SAXS and WAXS data show that significant structural changes are occurring in the foam as a function of stabilisation temperature.

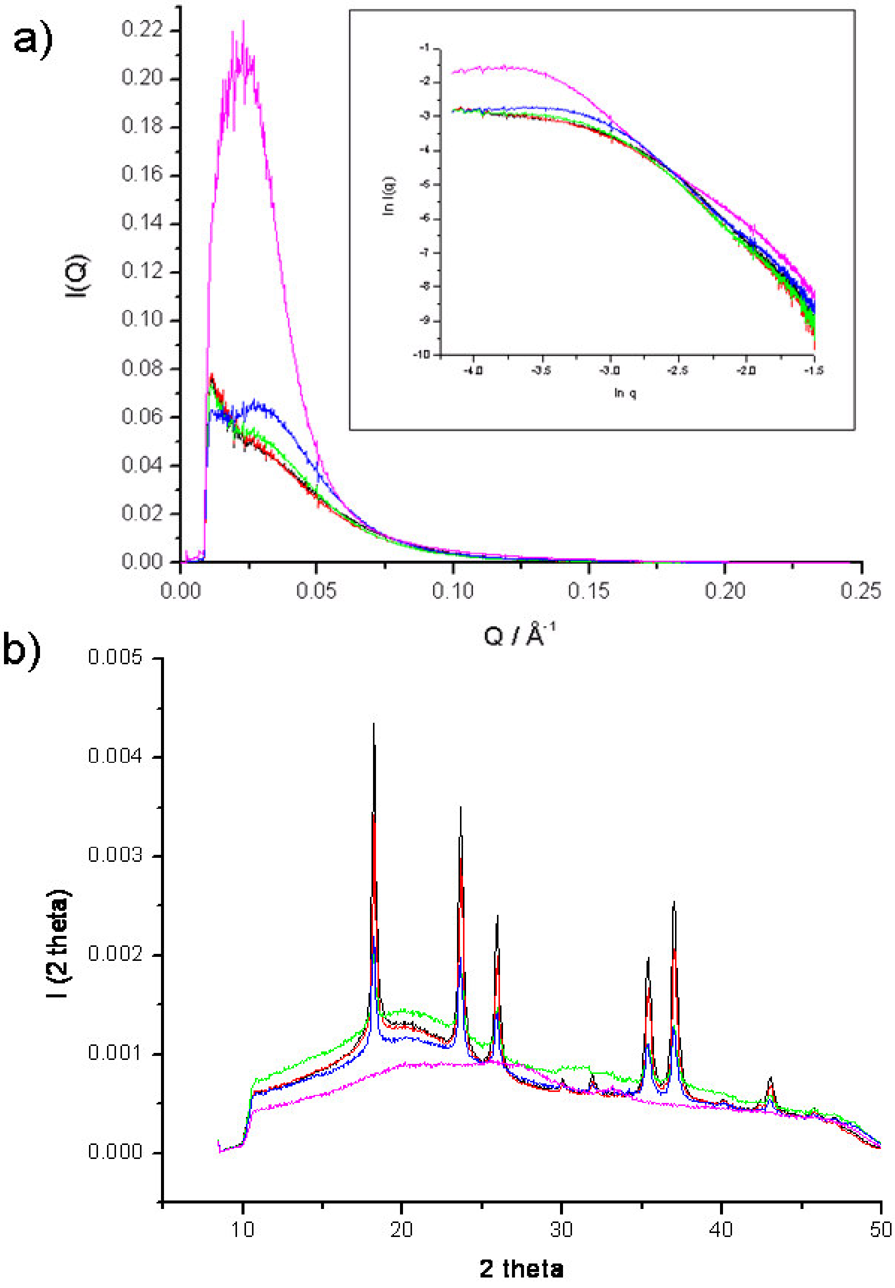

Figure 9.2: a) SAXS data for foam one: dried foam (black), foam stabilised at 100 °C (red), foam stabilised at 300 °C (green), foam stabilised at 400 °C (blue), foam stabilised at 600 °C (magenta). **b)** WAXS data for foam one: dried foam (black), foam stabilised at 100 °C (red), foam stabilised at 300 °C (green), foam stabilised at 400 °C (blue), foam stabilised at 600 °C (magenta).

The WAXS data for the dried foam, and foams stabilised to 100, 300 and 400 ºC all show Bragg diffraction peaks, whereas the foam stabilised to 600 ºC appears completely amorphous. The Bragg peaks in the WAXS data can be assigned as calcium nitrate ($Ca(NO_3)_2$), which is the precursor form in which Ca is introduced into the sol-gel synthesis route adopted [9.9]. The WAXS data therefore indicates that the calcium is not fully incorporated into the silica network until a stabilisation temperature of > 400 ºC. The WAXS data shown herein reveals a decrease in the intensity of calcium nitrate Bragg peaks as the heat-treatment temperature increases, and by a point between 400 ºC and 600 ºC the calcium nitrate has evidently decomposed. This observation is consistent with previous differential thermal analysis (DTA) data [9.10] which concluded that the complete decomposition of the nitrate had occurred by approximately 500 ºC. These observations are also supported by the tabulated decomposition temperature of bulk calcium nitrate (>400 ºC [9.11]), and are entirely consistent with previous NMR work on an analogous unfoamed sample of the same composition [9.3] (Figure 9.1). Although measured on a coarse temperature grid, the NMR data nevertheless revealed, via the presence of a Ca-O-Si peak, that the calcium is incorporated into the silica network by 700 ºC. Similarly, Raman spectroscopy data presented in the same study showed no sign of calcium nitrate after ~350-360 ºC [9.3] (Figure 9.1). In this latter comparison, one is unable to discern whether the minor difference in decomposition temperatures is due to the fact the samples studied by Raman spectroscopy were unfoamed (i.e. they contained no macropores, with the consequential upper limitation to included crystallite sizes) or to some artefact associated with small variations in the experimental thermal processing.

Figure 9.3 shows the average crystallite size as a function of heat treatment temperature, derived using Equation 9.1.

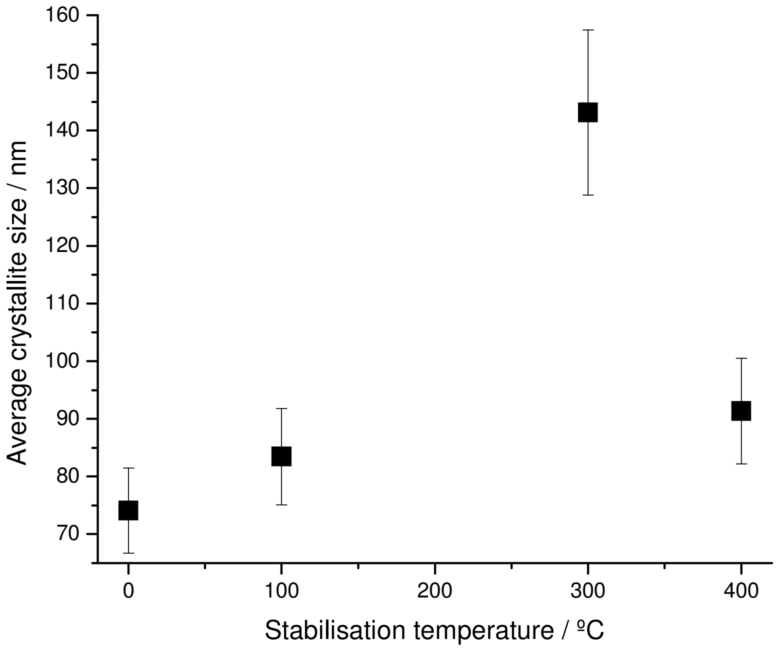

Figure 9.3: Average crystallite size as a function of temperature.

As the dried foam is heated, the crystallites of calcium nitrate grow, presumably via coalescence, and reach a maximum at a temperature of ~300 °C. At a temperature between 300 °C and 400 °C the crystallites decrease in size, presumably as material is progressively lost from their surfaces. When considered together with earlier diffraction-based experimental work and related molecular dynamics atomistic simulations on comparable sol-gel calcia-silica materials [9.12, 9.13], these results provide additional insight into the facile nature of Ca dissolution. Calcium is bonded only weakly to the host silica xerogel network, with the presence of connected pores (see below) facilitating the access of SBF, the outward diffusion of the Ca ions and the subsequent deposition/growth of calcium phosphates.

The SAXS data (Figure 9.2 b) reveal a major change in structure beginning to occur by a temperature of 400 ºC, with a structural peak apparent at 0.03 $Å^{-1}$, which becomes prominent by 600 ºC, albeit at a slightly shifted position at 0.023 $Å^{-1}$. In real-space these correspond to length-scales of ~21 nm and ~31.5 nm for material heated to temperatures of 400 ºC and 600 ºC respectively. Furthermore, the FWHM of the peak for a sample heated to a temperature of 600 ºC suggests a range of length-scales of 16.5-62 nm. This is in accord with nitrogen adsorption data from a previous experiment carried out on samples of the same composition [9.1] which revealed a pore size range of 8-60 nm for samples synthesised with varying levels of foaming. The pores observed correspond to the textural mesopores, inherent to the sol-gel process, which contribute most heavily to the bioactive material's surface area, and therefore to the dissolution and re-deposition processes. The data presented herein therefore shows that these important mesopores appear at a temperature of ~ 400 ºC, and may not be fully developed until the temperature of the heat-treatment has reached ~600 ºC.

Figure 9.4 shows the radius of gyration (R_g) as a function of temperature; this indicates an increase in R_g as the temperature increases. The WAXS data discussed above in the context of the Scherrer equation demonstrates that R_g cannot correspond to the calcium nitrate crystallites. It is therefore likely that the radius of gyration observed is due to the pore structure associated with the silica network: thus, the mesopores grow in size with heat-treatment temperature. However, previous studies using nitrogen sorption have shown that as the temperature increases above 700 °C, the mesopore size begins to decrease, due to viscous flow sintering [9.2].

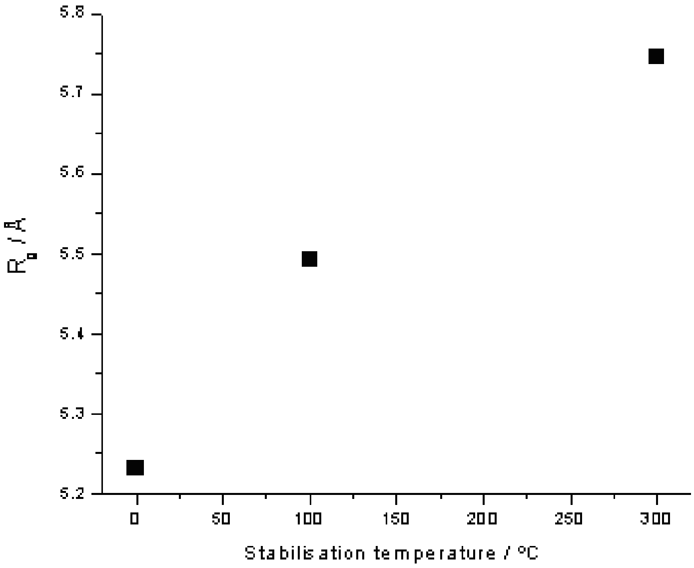

Figure 9.4: Radius of gyration as a function of temperature.

In Figure 9.5 we present an analysis of the data from an intermediate range of *Q*, again as a function of stabilisation temperature. The results show a progressive move away from a power law index of -4 (which would indicate a smooth surface/boundary) as the foams are heated to higher temperatures, and this indicates that the surfaces becomes relatively rougher. This occurs irrespective of the change in the overall size of the pores themselves.

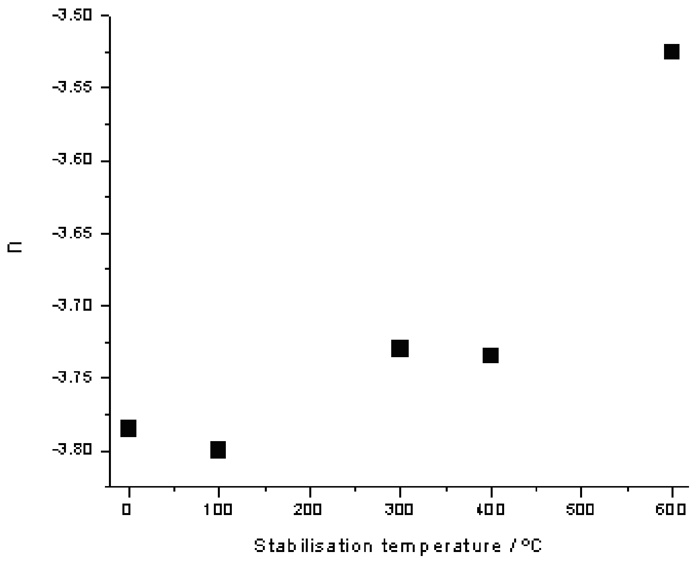

Figure 9.5: Power-law exponent at the intermediate Q-range as a function of temperature.

This insight must be combined with that from Figure 9.6, which shows a Porod analysis of the high *Q* region of the data. The data show that, as the foams are heated, the specific surface area per unit volume is approximately constant until a temperature of ~300 ºC, after which it increases with temperature. This increase in specific surface area per unit volume is most probably associated with the growth of the mesopores, identified earlier, which are seen to begin growing at a temperature of between 300 ºC and 400 ºC.

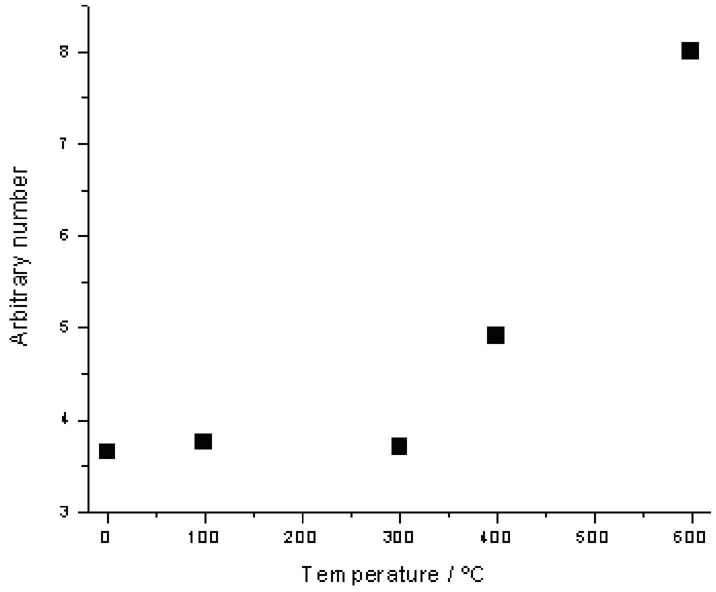

Figure 9.6: Qualitative variation of the specific surface area per unit volume as a function of temperature.

9.3 SAXS/WAXS study *in-situ* of foams in SBF

For the *in-situ* experiment, the same setup was used as above, however a specialised cell was used which allowed the SBF, heated to 37 °C, to flow over a cuboid of foamed glass. A photograph of the specially designed cell is shown in Figure 9.7, and a schematic of the experimental setup is shown in Figure 9.8.

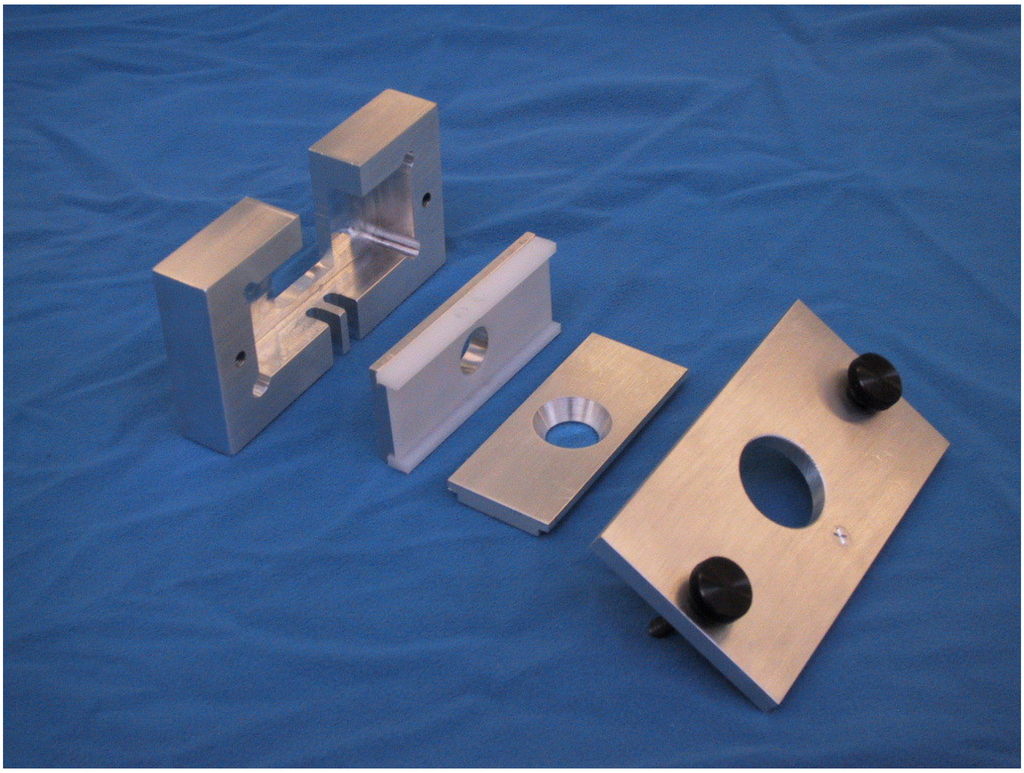

Figure 9.7: Photograph showing components of sample cell. The slice of foam is placed inside the hole in the white plastic spacer. Thin mica windows are sealed with Si sealant to ensure no leaking.

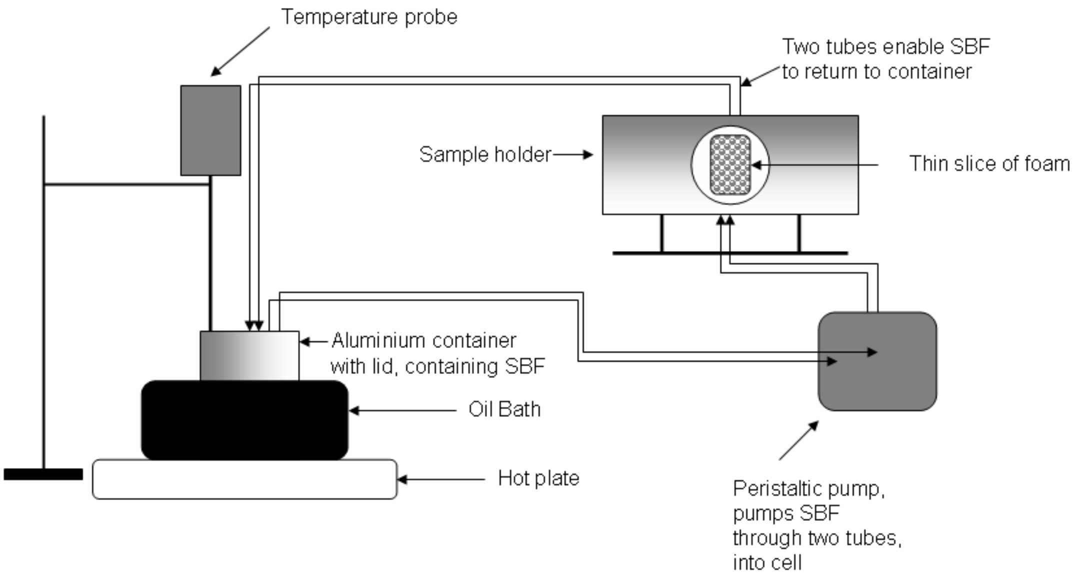

Figure 9.8: Schematic of the SAXS experimental setup. The SBF is kept at 37 ºC and pumped over the foam through two tubes using a peristaltic pump.

Frames were taken of the SBF alone in the cell, and of the foam alone in the cell, then SBF was added and sets of two consecutive 120 s scans were taken 1 minute apart for ~ 10 hours. The data was normalised and 'background' associated with the SBF alone was removed from the *in-situ* data; a minor multiplicative scaling of the SBF background was required in order to compensate for the self-shielding effects of the volume element associated with the sample's position in the X-ray beam. The experiment was carried out three times, in order to ensure reproducibility of data. The other two sets of data are presented in Appendix 5 for reference. The particular data set chosen to be investigated fully was a reaction involving no interruptions (e.g. due to various circumstances such as transitory beam interruptions at the synchrotron, which could last for over an hour).

Figure 9.9 shows *in-situ* small angle scattering data taken on a time-resolved basis for a piece of foam immersed in SBF for a total of approximately 6 hours. The data show that, as the foam reacts with SBF, the main peak decreases in intensity and shifts to higher *Q*. At the beginning of the reaction the average pore diameter is 40.5 nm, and after ~ 6 hours in SBF the average pore diameter has decreased in size to 30.7 nm. This result is what would be expected on the basis of earlier *in-vitro* experiments which have shown that the growth of calcium phosphates, and the later formation of hydroxyapatite (HA) and hydroxycarbonate apatite (HCA) as these materials react with SBF: i.e. the decrease in average pore diameter could be due to the growth of these calcium phosphates on the glass surfaces, causing the pore diameters to decrease with time immersed in SBF.

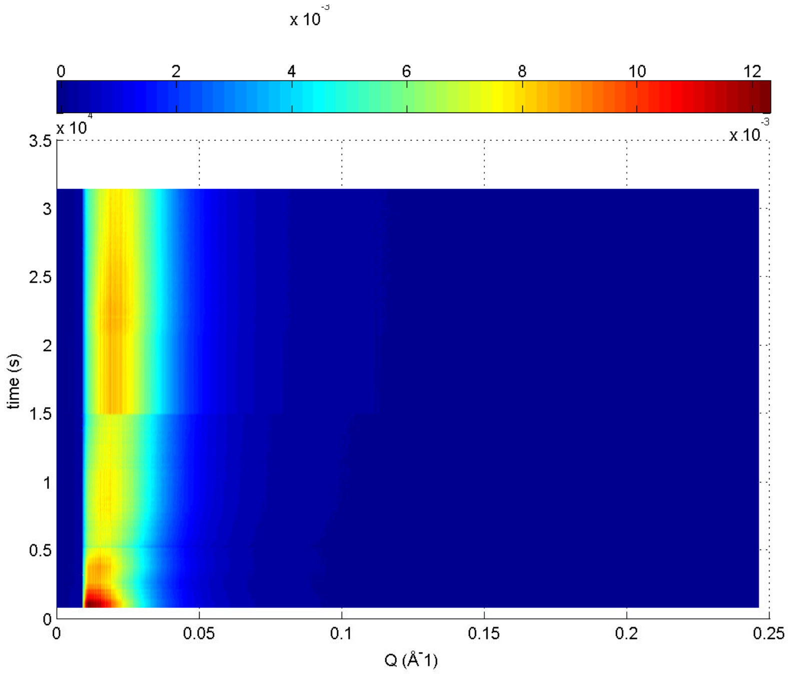

Figure 9.9: Graphical representation of SAXS data for the foam immersed in SBF as a function of time.

Figure 9.10 shows the simultaneously observed WAXS for the foam immersed in SBF. The WAXS data show evidence of Bragg peak growth after only 30 minutes in SBF. The Bragg peaks occurring are indicative of calcium phosphates, principally tricalcium phosphate [9.14] after 30 minutes in SBF and later HCA [9.15] after approximately 1.5 hours in SBF.

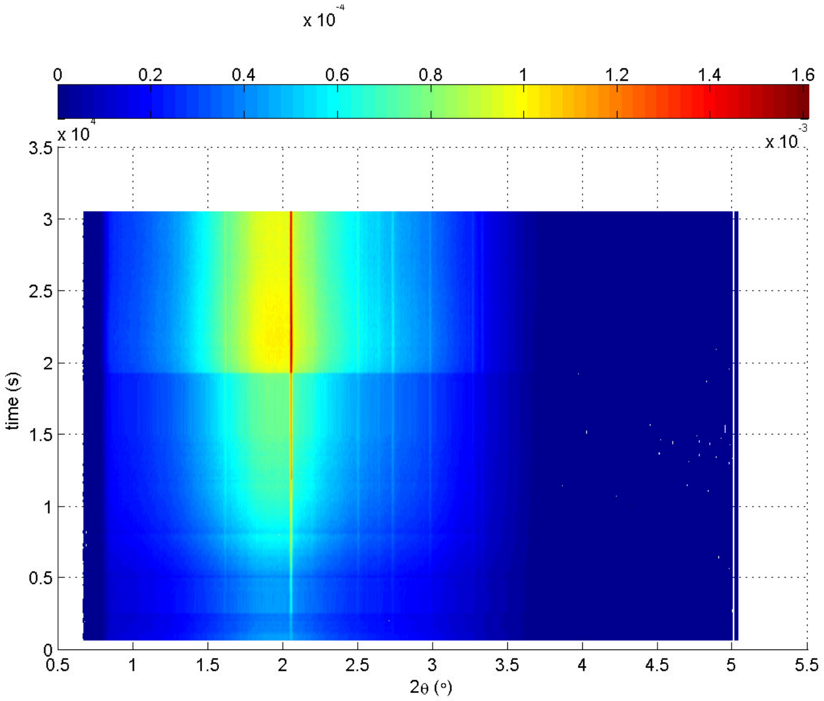

Figure 9.10: Graphical representation of WAXS data for the foam immersed in SBF as a function of time.

Given the relative peak intensities observed, and the absence of some predicted peaks, the HCA appears to be growing with some preferred orientation in the *(h,k,0)* plane.

9.4 Summary

The data have shown that, during the stabilisation stage of bioactive glass foam processing, calcium nitrate crystallites grow in size up to a temperature of 300 ºC and then begin to decrease in size, and that it is not until a temperature of >400 ºC that the precursor calcium nitrate in the foams is fully decomposed and the calcium is incorporated into the silica glass network. Mesopores appear to begin growing by 400 ºC, with an average pore diameter of ~21 nm, which then increases to 31.4 nm when the material is heated to 600 ºC. The dispersion in the length scales associated with the latter sample was shown to correspond to a range of pore diameters of 16.5 – 62 nm.

The *in-situ* time resolved data show that pore size decreases as a function of immersion time in SBF as calcium phosphates grow on the surfaces of the glass. The calcium phosphate growth occurs after only 1 hour immersion in SBF, and the phases observed are tricalcium phosphate and hydroxycarbonate apatite. The HCA appears to have preferred orientation in the *(h,k,0)* direction.

As with the earlier discussion of the atomic- and meso-scale effects of thermal stabilisation, one may relate the *in-vitro* behaviour of the material when reacted with SBF to its observed structure. In this case, the *in-situ* and time-resolved study show that the mesopores are progressively filled with calcium phosphates, and ultimately HCA, as the host glass matrix is dissolved by the SBF. Although deposition will presumably also be occurring on the inner surfaces of the macropores formed as a direct consequence of the initial foaming procedure, this will necessarily have comparatively little effect on their diameter. Thus, the mesoporous network facilitates the rapid growth of relatively high-density HCA, which will therefore eventually replace the initial silicate glass as the material bounding the macropores.

The relationship between the observed atomic- and meso-scale structure of this bioactive glass material and its observed in vitro behaviour and attributes has been further elucidated.

References

[9.1] Sepulveda, P., Jones, J.R., Hench, L.L., *J. Biomed. Mater. Res.,* **59**, 340-348, 2002.

[9.2] Jones, J.R., Ehrenfried, L.M., Hench, L.L., *Biomaterials*, **27**, 964-73, 2006.

[9.3] Skipper, L.J., Sowrey, F.E., Rashid, R., Newport, R.J., Lin, Z., Smith, M.E., *Phys Chem Glasses,* **46**(4), 372-376, 2005.

[9.4] Skipper, L.J., Sowrey, F.E., Pickup, D.M., FitzGerald, V., Rashid, R., Drake, K.O., Lin, Z., Saravanapavan, P., Hench, L.L., Smith, M.E., Newport, R.J., *J. Biomed. Mater. Res.,* **70**A, 354, 2004.

[9.5] http://www.srs.ac.uk/srs/stations/station6.2.htm

[9.6] http://www.srs.dl.ac.uk/NCD/computing/manual.otoko.html

[9.7] Toebbens, D.M., Stuesser, N., Knorr, K., Mayer, H.M., Lampert, G., *Materials Science Forum*, **378**, 288-293, 2001.

[9.8] Nuffield, E.R. X-Ray Diffraction Methods. New York: Wiley & Sons; 1996.148p.

[9.9] Vegard, L., Bilberg, L. Skrifter utgitt av det Norske Videnskaps-Akademi i Oslo 1: Matematisk-Naturvidenskapelig Klasse, **31**, 1-22, 1931.

[9.10] Saravanapavan, P., Hench, L.L., *J. Non. Cryst. Solids*, **318,** 1-13, 2003.

[9.11] http://www.hummelcroton.com/axxo/lo1m.html

[9.12] Skipper, L.J., Sowrey, F.E., Pickup, D.M., Drake, K.O., Smith, M.E., Saravanapavan, P., Hench, L.L., Newport, R.J., *J. Mater. Chem.,* **15,** 2369-2374, 2005.

[9.13] Mead, R.N., Mountjoy, G., *Chem. Mater.,* **18**, 3956-3964, 2006.

[9.14] Yashima, M., Sakai, A., Kamiyama, T., Hoshikawa, A., *J. Solid State Chem.*, **175,** 272-277, 2003.

[9.15] Fleet, M.E., Xiaoyang, L., *J. Solid State Chem.*, **177**, 3174-3182, 2004.

[9.16] Rehman, I., Knowles, J.C., Bonfield, W., *J. Biomed. Mater. Res.,* **41**(1), 162-166, 1998.

Chapter 10

Conclusions and Future Work

10.1 Conclusions

This chapter summarises the achievements of the work presented in this thesis. Detailed conclusions for each investigation can be found at the end of results chapters 6-9.

It is shown in this thesis that diffraction techniques can be used to investigate the structure of bioactive glasses, and that the atomic scale structure can be linked to the bioactive properties of the glasses. It has been demonstrated that, using diffraction techniques, combined with element specific MAS NMR data and computer simulation, a robust model of the structure of Bioglass® can be produced. The model shows that the sodium environment in Bioglass® is six-coordinated in a pseudo-octahedral arrangement, and shows evidence of a non-homogeneous distribution of sodium in the glass, which is important in the context of the relatively slow dissolution of the modified silica network. The calcium appears to be five-coordinated, with more than one correlation sub-shell, and the calcium distribution in the model offers evidence of clustering, which is of direct relevance to the understanding of the facile nature of calcium within such glasses, which gives rise to its relatively rapid diffusion from the solid into solution. The phosphorus has been shown to exist as mainly orthophosphate units, which remove sodium and calcium cations from a network modifying role in the silica network.

Hydroxyapatite has been confirmed as the calcium phosphate phase which grows on the surface of Bioglass® when immersed in a standard cell culture medium, and data indicates that in the first 24 hours in TBS the hydroxyapatite crystals are growing with preferred orientation in the *(00l)* plane. Diffraction data taken in order to compare the reaction of a bioactive glass immersed in SBF to one immersed in TBS has shown that the solution does effect the reaction rate in the early stages, however the data showed that after 7 days immersion time both samples appeared to have very similar structure.

High-energy X-ray diffraction (HEXRD) experiments carried out on a foamed bioactive calcia-silica sol-gel glass have shown that foaming has no effect on the structure of the glass. The diffraction data shows that after 24 hours immersion time in SBF the growth of calcium phosphates are observed, however Raman spectroscopy data indicates that the growth of calcium phosphates is occurring as early as 2 hours immersion time in SBF.

Described in this thesis is a new method which can be used for *in-situ* time resolved high-energy X-ray diffraction studies of reaction mechanisms such as those involved when a bioactive glass is immersed in a simulated physiological solution. Although the data presented in this thesis can only be analysed semi-quantitatively, it has been demonstrated that structural changes in glass as a function of reaction time can be observed.

Small-angle X-ray diffraction has been used as a characterisation technique to investigate the mesoporous structure present in the foamed bioactive calcia-silica sol-gel glass. During the stabilisation stage of the sol-gel processing, which involves heating the foam after ageing and drying, up to 600 ºC, it is not until 400 ºC that the mesopores appear to begin growing. The mesopores have an average pore diameter of ~21 nm, which increases to 31.4 nm when the material is heated to 600 ºC. During this stabilisation process, it is also possible to observe the point at which the precursor calcium nitrate in the foams is fully decomposed and the calcium is incorporated into the silica glass network. This process was observed to occur not until a temperature of >400 ºC had been reached.

In-situ time resolved small angle X-ray scattering data showed that pore size decreased as a function of immersion time in SBF, as calcium phosphates grew on the surfaces of the glass. Simultaneous wide angle X-ray diffraction showed that, after 1 hour immersion time in SBF, calcium phosphate growth occurred, and the phases identified are tricalcium phosphate and hydroxycarbonate apatite (HCA). The HCA appeared to be growing with preferred orientation in the (*h,k,0*) direction. The mesoporous network facilitates the rapid growth of relatively high-density HCA, which will therefore eventually replace the initial silicate glass as the material bounding the macropores.

10.2 Future Work

The future of biomaterials could take many different directions, as so much is still to be understood. Future work based on the investigations carried out in this thesis could include an in-depth X-ray fluorescence analysis of the bioactive calcia-silica sol-gel foam sintered to 800 ºC, in order to obtain more accurate compositional data to analyse the *in-situ* high-energy X-ray diffraction data, and to directly compare it to that of the foam sintered to 600 ºC. Also *in-situ* HEXRD studies could be performed on Bioglass® in order to compare the reaction to that of a foamed bioactive calica-silica sol-gel glass.

Since the production of bioactive glasses, many different compositions of glass have been investigated, for example bioactive glasses of both the melt-quenched and sol-gel type examined within this thesis have been doped with silver or copper, which have antibacterial properties [10.1, 10.2]. The techniques utilised in this thesis have proved useful tools in analysing the structure of some bioactive glasses, and enabling the structure to be linked with the bioactive properties of the glass. These techniques will enable the structure of future biomaterials to be analysed, and hence help in the understanding of their bioactive properties.

References

[10.1] Bellantone, M., Williams, H.D., Hench, L.L., *Antimicrob Agents Chemother*.,**46**(6) 1940–1945, 2002.

[10.2] Saravanapavan, P., Gough, J.E., Jones, J.R., Hench, L.L., *Key Engineering Materials*, **254-256**, 1087-1090, 2004.

Appendix 1

1. POLAR

This program performs a correction to account for the polarization of the synchrotron beam:

$$I_{out} = \frac{I_{in}}{\left(P_{\perp} + P_{//}\cos^2(2\theta)\right)}$$

where P is the fraction of beam polarization in the perpendicular and parallel planes to that of the scattering. The program requires $P_{//}$ (fraction of beam polarization in the scattering plane) to be input. For station 9.1 (SRS) $P_{//} = 0.10$ and for ID15B (ESRF) $P_{//} = 0.07$.

2. VOLUME

Performs the following volume variation correction assuming flat plate geometry and θ/2θ scanning:

$$I_{out} = \frac{I_{in}\cos\theta}{t}$$

where *t* in the thickness of the sample in mm (arbitary due to later scaling factor).

3. BACKSUB

Simply subtracts the X-ray scattering from the background (e.g. empty container) from the data. The background scan must be corrected for the same initial processes as the experimental data.

4. ANALYSE

Calculates the corrections that applied to the data to yield the interference function *I*(2θ). Requires an input file in the form (without the table and text):

	Si	O	Ta
Z	14	8	73
n	0.65	2	0.28
a1	5.66269	3.0485	29.2024
a2	3.07164	2.2868	15.2293
a3	2.62446	1.5463	14.5135
a4	1.3932	0.867	4.76492
b1	2.6652	13.2771	1.77333
b2	38.6634	5.7011	9.37046
b3	0.916946	0.3239	0.295977
b4	93.5458	32.9089	63.3644
c	1.24707	0.2508	9.24354
A	0.5085	0.37033	1.0131
B	1.14764	1.22426	0.3488
C	13.2148	25.4902	2.3987

The program also requires the absorption correction μt to be input. This can be calculated as in the example below.

Element	c	Am	mu/rho cm2/g	g (mass fraction)	g* mu/rho
Si	0.65	28.10	0.20	0.18	0.04
O	2.00	16.00	0.16	0.32	0.05
Ta	0.28	180.60	5.94	0.50	2.98
		100.83			3.07

$$\mu t = \sum(\mu g/\rho) * \rho t$$

where ρ is the density in the sample holder and t is the sample thickness in cm.

The program outputs the self-scattering, the Compton scattering, the sharpening function and absorption correction as a function of scattering angle.

To perform the calculations the program calculates the independent scattering factor f_i for each atom:

$$f_i = \sum_i^4 a_i \exp\left(-b_i\, s^2\right) + c$$

where $s = \sin\theta/\lambda$.

The inelastic contribution or Compton scattering from each atom is calculated by one of the following two equations depending on atomic number.

For $Z \leq 20$:

$$I_i^C = \left[Z - \frac{f_i^2}{Z}\right]\left\{1 - A\left(\exp(-Bs) - \exp(-Cs)\right)\right\}$$

For Z > 20:

$$I_i^C = Z\left[1 - \frac{A}{(1 + Bs)^C}\right]$$

The total Compton scattering is given by $I^C = \sum c_i I_i^C$ where c_i is the mole fraction of element *i*.

The Sharpening function, which essentially collapses the scattering for the diffuse electron clouds within the sample to that expected for point-source scatterers, is given by:

$$f_e = \frac{\sum_{UC} f_i}{n_{UC}}$$

where *UC* means summed over unit composition and n_{UC} is the number of atoms in the unit composition.

Finally, the self-scattering, which represents independent scattering from atoms where there is no interference, is given by:

$$I_{self} = \sum_i c_i f_i^2$$

5. CORRECTIONS

This program applies the corrections calculated in **ANALYSE** according to the equation given below:

$$I_{out} = \frac{SI_{in}\exp(\mu t/\cos\theta) - AI^{C} - I_{self}}{f_e^2}$$

where $(\mu t/\cos\theta)$, I^C, I_{self} and f_e are obtained from the output file form **ANALYSE**, and S and A are scaling factors which can be varied in the program (to give $i(2\theta)$ that oscillates about zero).

6. POLY

Fits a polynomial through $i(2\theta)$ to account for any inadequacies of the corrections made in the previous program. User inputs angle from which to start fit and program treats the data as zeros below this angle. User also specifies order of the polynomial.

7. QBIN

Converts $i(2\theta)$ into $i(Q)$ where:

$$Q = \frac{4\pi\sin\theta}{\lambda}$$

8. FT

Performs Fourier transform on *i(Q)* to yield real-space correlation function:

$$d(r) = \int_{Q_{\min}}^{Q_{\max}} M(Q) Q i(Q) \sin(Qr)\, dQ$$

where *M(Q)* is the optional Hanning window function, applied to reduce FT termination ripples:

$$M(Q) = 0.5 + 0.5\cos\left(\frac{\pi Q}{Q_{\max}}\right)$$

Appendix 2

1. purge_det

This program identifies problems with any detectors, i.e. detectors that are dead, unstable, or contain spikes. Any detectors with such problems can then be excluded from the analysis.

2. gudrun_dcs

This program produces a final corrected *S(Q)* differential cross section curve for each detector group. This program sums all the runs of each type, and converts to a *Q*-scale. The data are corrected for absorption and multiple scattering, and they are normalised to vanadium to produce a result that is on an absolute cross-section scale. The program uses information about the instrument, the beam, the vanadium files, the background, the sample and the container. An example of a gudrun input file can be found in the gudrun manual located on the ISIS website.

3. PLATOM

This program is used to calculate the self-scattering term for the sample with a Placzek inelasticity correction.

4. INTERFERE

This program performs the self-scattering, I^{self} subtraction (calculated by PLATOM) for each of the differential cross section curves.

$$s(Q) = S(Q) - I^{self}$$

The result is the distinct scattering *s(Q)*. An *s(Q)* is produced for each of the detector groups, however the result obtained may sometimes not oscillate about zero as it should. This can be corrected by multiplying the diffraction pattern *S(Q)* by a renormalizing factor *a* prior to the subtraction.

5. MERGE

The MERGE program is used to combine together the data from all detector groups to produce a single composite diffraction pattern. The detector groups to include, and the *Q*-range of each detector group to be used, are chosen and input into MERGE. When GEM data are merged they are weighted according to 1/error^2.

6. i2T

The next step is the Fourier Transform of the resultant *S(Q)*.

$$T(r) = T^0(r) + \frac{2}{\pi}\int_0^\infty QS(Q)M(Q)\sin(Qr)dQ$$

where the average density contribution is,

$$T^0(r) = 4\pi r\rho_0(\sum_i c_i b_i)^2$$

ρ_0 is the macroscopic number density, and c_i and b_i are the atomic fraction and coherent scattering length respectively, of element *i*. *M(Q)* is a modification function used to take into account the maximum experimentally attainable value of *Q*.

Appendix 3

1) RANDOM

The RANDOM program will place atoms into a box randomly. The number of atoms and the number density are input.

2) MOVEOUT

This program can impose the closest approach of two atoms. Using the output from RANDOM it moves the atoms apart if they are too close together.

3) MIDPT

This program has the ability to place atoms at the midpoint of bonds between two other atoms. This is useful, for example, when creating a silica network, as an oxygen atom can be placed at the mid-point between two Si atoms.

4) ADDRAND

This program will add atoms randomly to a configuration without any constraints.

5) ADDATOM

This program will add atoms close to other atoms in a configuration defined by the coordination of the target atoms.

6) DELATOM

Atoms can be selected by type, or coordination, and then deleted or renamed as other atom types.

Appendix 4

Tris buffer solution (TBS) is prepared as follows, (courtesy of NovaMin Technology Ltd, USA).

1. Fill a 6000 mL pyrex flask with 2000 mL of deionized (DI) water
2. Put a magnetic stir bar in the flask and place it on a stir/hot plate
3. Turn the stirring on to a medium setting and the heat onto a low setting (make sure that a low heat setting is used so that the solution heats slowly and does not exceed a temperature of 37 °C)
4. Weigh out 30.18 grams of THAM (Tris(hydroxymethyl)aminomethane)
5. Add the THAM to the flask and rinse the weigh boat and neck of the flask with DI water to ensure that all of the THAM is added to the solution
6. Stir until the THAM is completely dissolved
7. Add 884 mL of 0.2N HCl to the flask
    - Prepare the 0.2N HCl by adding 17 mL of concentrated (12.1N) HCl to 983 mL of deionized in a 2000 mL graduated cylinder
    - Set aside the remaining 116 mL of 0.2N HCl (will be used later for pH adjustment
8. Dilute solution in flask to 4000 mL with DI water
9. Place a liquid pH probe and thermometer into the solution
10. Continue stirring and heating the solution until it reaches a temperature of 37 °C
11. Record the pH of the solution
12. Slowly add 0.2N HCl solution until the final pH = 7.25 at 37 °C

13. Record the final pH and temperature of the solution
14. Label the TRIS buffer with the final pH, temperature, date it was made, and expiration date (expires 30 days after it is made)
15. Store the TRIS Buffer in a refrigerator until it is needed

SBF is prepared as follows;

A 1000 ml beaker containing 700 ml deionised water was placed on a magnetic stirring plate. The water was heated up to approximately 37 °C and each chemical reagent given in Table 4A was added into the water, one by one in the order given in the table, after each reagent was completely dissolved.

Order	**Reagent**	**Amount (g/dm^3)**
1	NaCl	7.996
2	$NaHCO_3$	0.350
3	KCl	0.224
4	$K_2HPO_4\cdot 3H_2O$	0.228
5	$MgCl_2\cdot 6H_2O$	0.305
6	1N HCl	40 ml
7	$CaCl_2\cdot 2H_2O$	0.368
8	Na_2SO_4	0.071
9	$(CH_2OH)CNH_2$	6.057

Table 4A: Reagents used in preparation of SBF.

After the last addition, the whole ensemble was placed in a water bath of temperature 36.5 °C. At this point, the solution pH was approximately 7.5 and was buffered at pH 7.25 using 1N hydrochloric acid. After the pH adjustment, the solution from the beaker was transferred into a 1L volumetric flask and was made up to that volume with the addition of deionised water. It was then stored in a refrigerator (at ~4 ºC) in polyethylene bottles for no longer than 1 month.

Appendix 5

Presented below is the second set of data for the *ex-situ* following of the foam through the stabilisation process. The data appear congruent to the data shown in Chapter 8, the data for the foam heated to 100 ºC has been omitted due to poor data quality.

a)

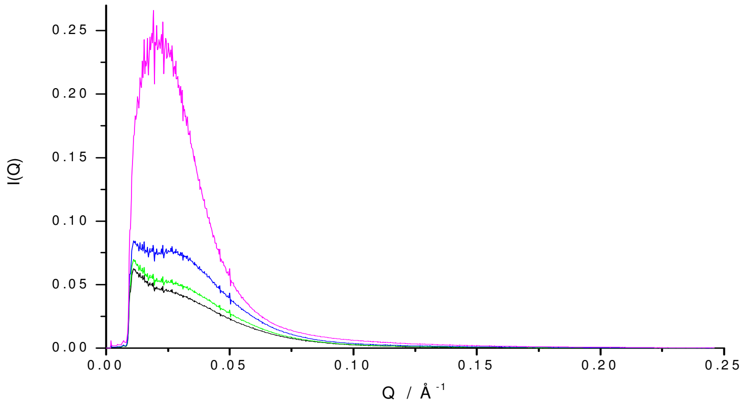

b)

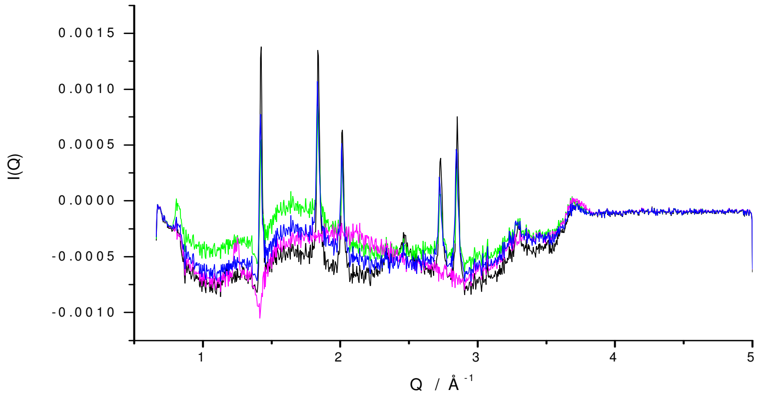

Figure 5A: a) SAXS data for foam two; dried foam (black), foam stabilised at 300 ºC (green), foam stabilised at 400 ºC (blue), foam stabilised at 600 ºC (magenta). **b)** WAXS data for foam one; dried foam (black), foam stabilised at 300 ºC (green), foam stabilised at 400 ºC (blue), foam stabilised at 600 ºC (magenta).

Shown below are *in situ* time-resolved data for two more cuboids of bioactive calcia-silica sol-gel foam reacting with SBF.

Figure 5B shows *in situ* time-resolved SAXS data for a piece of foam over ~9 hours. This reaction was interrupted after ~4 hours reaction time in SBF, and restarted after ~5.5 hours reaction time in SBF. This was due to a beam dump at the synchrotron.

Figure 5C shows the corresponding WAXS data for this reaction.

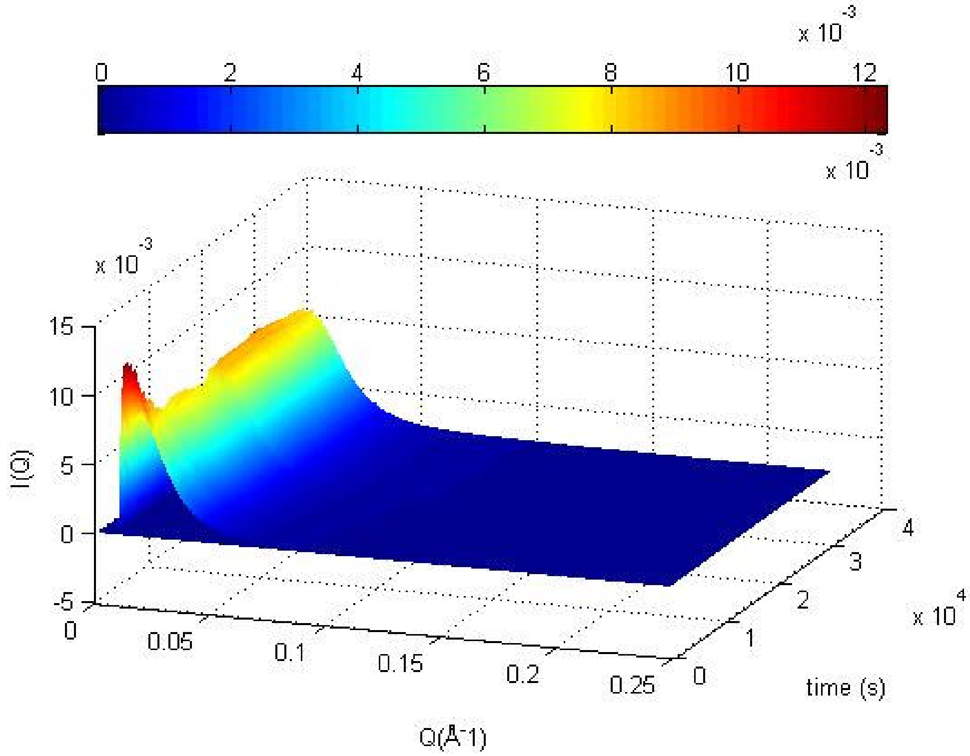

Figure 5B: *In-situ* time-resolved data for a foam reacting in SBF for approximately 9 hours, with a ~1.5 hour gap at ~4 hours.

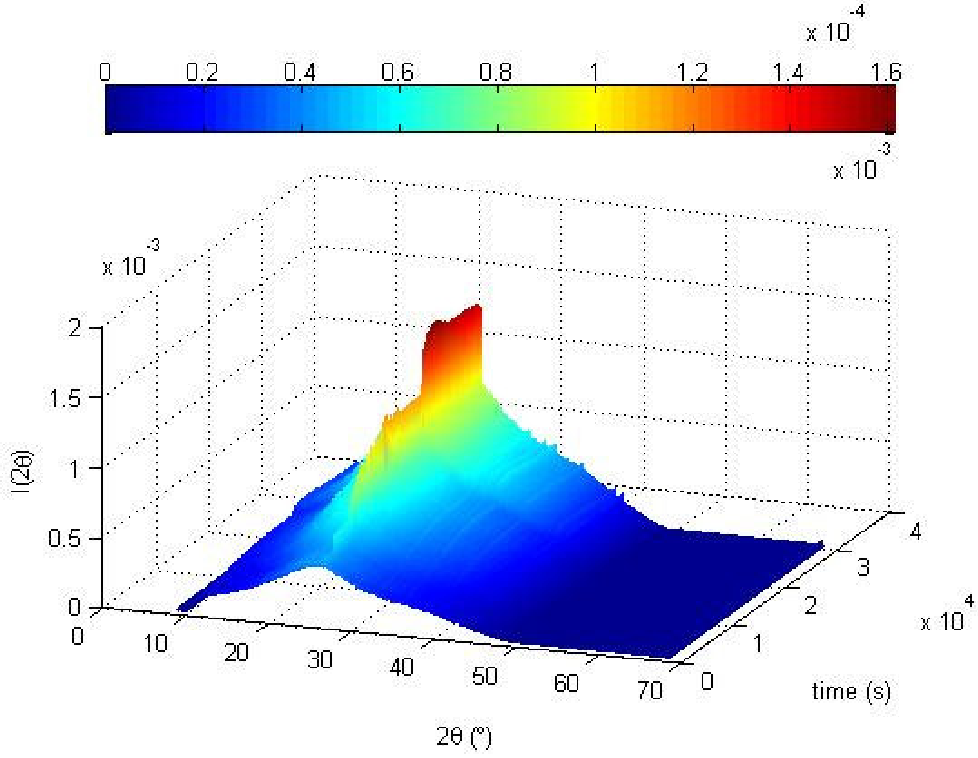

Figure 5C: Corresponding WAXS data

The gap in the measurements can clearly be seen in SAXS and the WAXS data, however, the data is consistent with the reaction used for an in depth analysis shown in Chapter 9.

Figure 5D shows *in-situ* time-resolved SAXS data for a piece of foam over ~12 hours. This reaction was interrupted after ~3.5 hours reaction time in SBF, and restarted after ~9 hours reaction time in SBF. This was due to a problem with the beam at the synchrotron.

Figure 5E shows the corresponding WAXS data for this reaction.

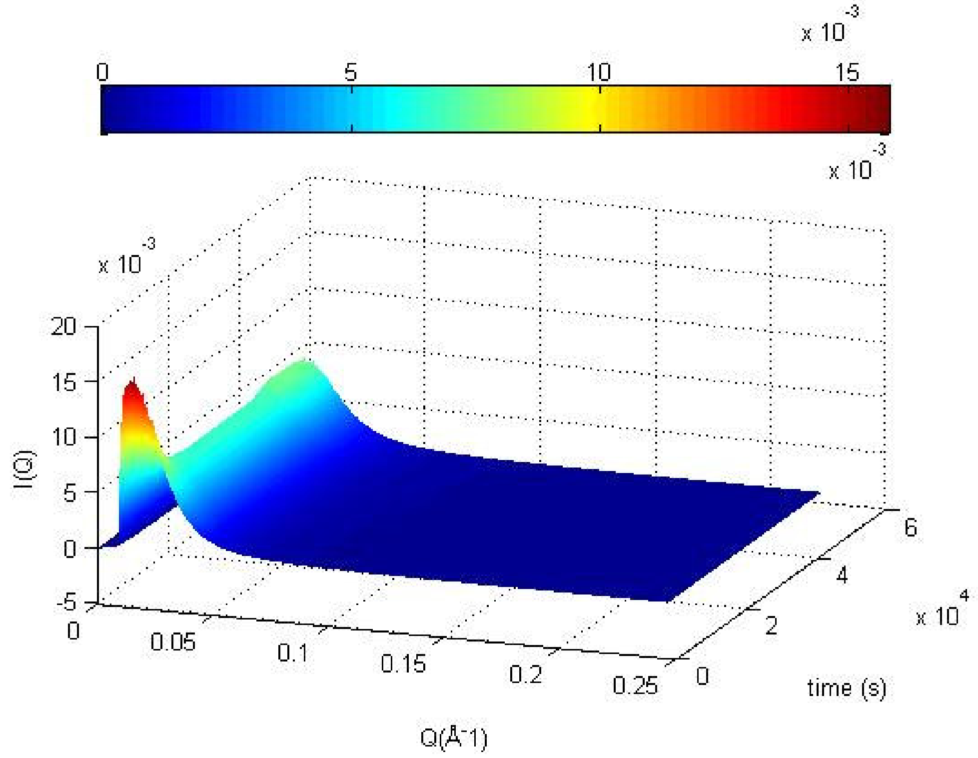

Figure 5D: *In-situ* time-resolved data for a foam reacting in SBF for approximately 12 hours, with a ~5.5 hour gap at ~3.5 hours.

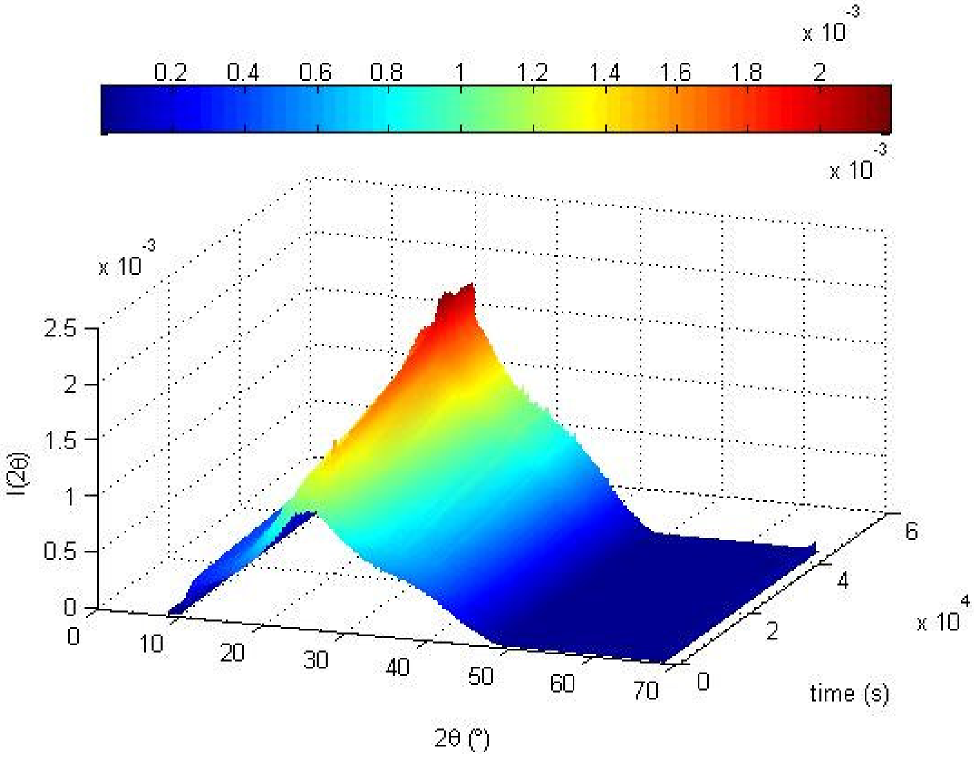

Figure 5E: Corresponding WAXS data

Again the gap in measurements are visible in both data sets, however both appear to be consistent with other data.

The SAXS for all experiments appear to behave in the same way, namely the main feature becomes less intense and broader, and shifts to slightly higher Q as a function of time in SBF. The Bragg peaks occur in the same positions in all WAXS measurements, all becoming visible after a short period of time, ~1hour, in SBF.